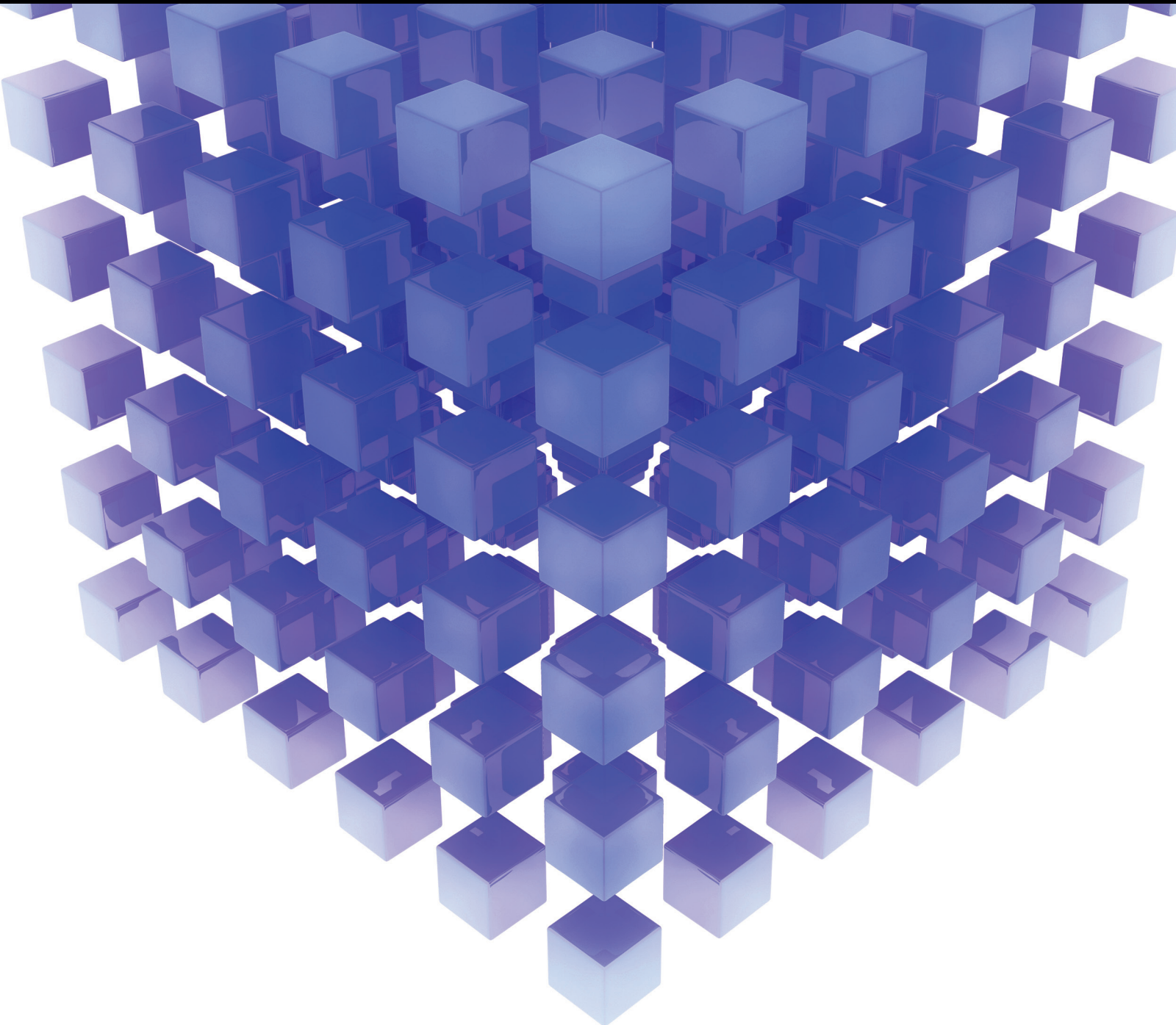


Mathematical Problems in Engineering

Structural Damage Modelling and Assessment 2014

Guest Editors: Anaxagoras Elenas, Yuri Petryna, and Nawawi Chouw





Structural Damage Modelling and Assessment 2014

Mathematical Problems in Engineering

**Structural Damage Modelling and Assessment
2014**

Guest Editors: Anaxagoras Elenas, Yuri Petryna,
and Nawawi Chouw



Copyright © 2015 Hindawi Publishing Corporation. All rights reserved.

This is a special issue published in “Mathematical Problems in Engineering.” All articles are open access articles distributed under the Creative Commons Attribution License, which permits unrestricted use, distribution, and reproduction in any medium, provided the original work is properly cited.

Editorial Board

Mohamed Abd El Aziz, Egypt
Farid Abed-Meraim, France
Silvia Abraho, Spain
Paolo Adesso, Italy
Claudia Adduce, Italy
Ramesh Agarwal, USA
Juan C. Agüero, Australia
Ricardo Aguilar-López, Mexico
Tarek Ahmed-Ali, France
Hamid Akbarzadeh, Canada
Muhammad N. Akram, Norway
Mohammad-Reza Alam, USA
Salvatore Alfonzetti, Italy
Francisco Alhama, Spain
Juan A. Almendral, Spain
Saiied Aminossadati, Australia
Lionel Amodeo, France
Igor Andrianov, Germany
Sebastian Anita, Romania
Renata Archetti, Italy
Felice Arena, Italy
Sabri Arik, Turkey
Fumihiko Ashida, Japan
Hassan Askari, Canada
Mohsen Asle Zaeem, USA
Francesco Aymerich, Italy
Seungik Baek, USA
Khaled Bahlali, France
Laurent Bako, France
Stefan Balint, Romania
Alfonso Banos, Spain
Roberto Baratti, Italy
Martino Bardi, Italy
Azeddine Beghdadi, France
Abdel-Hakim Bendada, Canada
Ivano Benedetti, Italy
Elena Benvenuti, Italy
Jamal Berakdar, Germany
Enrique Berjano, Spain
Jean-Charles Beugnot, France
Simone Bianco, Italy
David Bigaud, France
Jonathan N. Blakely, USA
Paul Bogdan, USA
Daniela Boso, Italy
Abdel-Ouahab Boudraa, France
Francesco Braghin, Italy
Michael J. Brennan, UK
Maurizio Brocchini, Italy
Julien Bruchon, France
Javier Bulduf, Spain
Tito Busani, USA
Pierfrancesco Cacciola, UK
Salvatore Caddemi, Italy
Jose E. Capilla, Spain
Ana Carpio, Spain
Miguel E. Cerrolaza, Spain
Mohammed Chadli, France
Gregory Chagnon, France
Ching-Ter Chang, Taiwan
Michael J. Chappell, UK
Kacem Chehdi, France
Chunlin Chen, China
Xinkai Chen, Japan
Francisco Chicano, Spain
Hung-Yuan Chung, Taiwan
Joaquim Ciurana, Spain
John D. Clayton, USA
Carlo Cosentino, Italy
Paolo Crippa, Italy
Erik Cuevas, Mexico
Peter Dabnichki, Australia
Luca D'Acerno, Italy
Weizhong Dai, USA
Purushothaman Damodaran, USA
Farhang Daneshmand, Canada
Fabio De Angelis, Italy
Stefano de Miranda, Italy
Filippo de Monte, Italy
Xavier Delorme, France
Luca Deseri, USA
Yannis Dimakopoulos, Greece
Zhengtao Ding, UK
Ralph B. Dinwiddie, USA
Mohamed Djemai, France
Alexandre B. Dolgui, France
George S. Dulikravich, USA
Bogdan Dumitrescu, Finland
Horst Ecker, Austria
Ahmed El Hajjaji, France
Fouad Erchiqui, Canada
Anders Eriksson, Sweden
Giovanni Falsone, Italy
Hua Fan, China
Yann Favennec, France
Giuseppe Fedele, Italy
Roberto Fedele, Italy
Jacques Ferland, Canada
Jose R. Fernandez, Spain
Simme Douwe Flapper, The Netherlands
Thierry Floquet, France
Eric Florentin, France
Francesco Franco, Italy
Tomonari Furukawa, USA
Mohamed Gadala, Canada
Matteo Gaeta, Italy
Zoran Gajic, USA
Ciprian G. Gal, USA
Ugo Galvanetto, Italy
Akemi Gálvez, Spain
Rita Gamberini, Italy
Maria Gandarias, Spain
Arman Ganji, Canada
Xin-Lin Gao, USA
Zhong-Ke Gao, China
Giovanni Garcea, Italy
Fernando Garcia, Spain
Laura Gardini, Italy
Alessandro Gasparetto, Italy
Vincenzo Gattulli, Italy
Jrgen Geiser, Germany
Oleg V. Gendelman, Israel
Mergen H. Ghayesh, Australia
Anna M. Gil-Lafuente, Spain
Hector Gómez, Spain
Rama S. R. Gorla, USA
Oded Gottlieb, Israel
Antoine Grall, France
Jason Gu, Canada
Quang Phuc Ha, Australia
Ofer Hadar, Israel
Masoud Hajarian, Iran
Frédéric Hamelin, France
Zhen-Lai Han, China
Thomas Hanne, Switzerland

Takashi Hasuike, Japan
Xiao-Qiao He, China
M.I. Herreros, Spain
Vincent Hilaire, France
Eckhard Hitzer, Japan
Jaromir Horacek, Czech Republic
Muneo Hori, Japan
András Horváth, Italy
Gordon Huang, Canada
Sajid Hussain, Canada
Asier Ibeas, Spain
Giacomo Innocenti, Italy
Emilio Insfran, Spain
Nazrul Islam, USA
Payman Jalali, Finland
Reza Jazar, Australia
Khalide Jbilou, France
Linni Jian, China
Bin Jiang, China
Zhongping Jiang, USA
Ningde Jin, China
Grand R. Joldes, Australia
Joaquim Joao Judice, Portugal
Tadeusz Kaczorek, Poland
Tamas Kalmar-Nagy, Hungary
Tomasz Kapitaniak, Poland
Haranath Kar, India
Konstantinos Karamanos, Belgium
C. M. Khalique, South Africa
Do Wan Kim, Korea
Nam-Il Kim, Korea
Oleg Kirillov, Germany
Manfred Krafczyk, Germany
Frederic Kratz, France
Jurgen Kurths, Germany
Kyandoghere Kyamakya, Austria
Davide La Torre, Italy
Risto Lahdelma, Finland
Hak-Keung Lam, UK
Antonino Laudani, Italy
Aime' Lay-Ekuakille, Italy
Marek Lefik, Poland
Yaguo Lei, China
Thibault Lemaire, France
Stefano Lenci, Italy
Roman Lewandowski, Poland
Qing Q. Liang, Australia
Panos Liatsis, UK
Wanquan Liu, Australia
Yan-Jun Liu, China
Peide Liu, China
Peter Liu, Taiwan
Jean J. Loiseau, France
Paolo Lonetti, Italy
Luis M. López-Ochoa, Spain
Vassilios C. Loukopoulos, Greece
Valentin Lychagin, Norway
Fazal M. Mahomed, South Africa
Yassir T. Makkawi, UK
Noureddine Manamanni, France
Didier Maquin, France
Paolo Maria Mariano, Italy
Benoit Marx, France
Gérard A. Maugin, France
Driss Mehdi, France
Roderick Melnik, Canada
Pasquale Memmolo, Italy
Xiangyu Meng, Canada
Jose Merodio, Spain
Luciano Mescia, Italy
Laurent Mevel, France
Y. V. Mikhlin, Ukraine
Aki Mikkola, Finland
Hiroyuki Mino, Japan
Pablo Mira, Spain
Vito Mocella, Italy
Roberto Montanini, Italy
Gisele Mophou, France
Rafael Morales, Spain
Aziz Moukrim, France
Emiliano Mucchi, Italy
Domenico Mundo, Italy
Jose J. Muñoz, Spain
Giuseppe Muscolino, Italy
Marco Mussetta, Italy
Hakim Naceur, France
Hassane Naji, France
Dong Ngoduy, UK
Tatsushi Nishi, Japan
Ben T. Nohara, Japan
Mohammed Nouari, France
Mustapha Nourelfath, Canada
Sotiris K. Ntouyas, Greece
Roger Ohayon, France
Mitsuhiro Okayasu, Japan
Eva Onaindia, Spain
Javier Ortega-Garcia, Spain
Alejandro Ortega-Moux, Spain
Naohisa Otsuka, Japan
Erika Ottaviano, Italy
Alkiviadis Paipetis, Greece
Alessandro Palmeri, UK
Anna Pandolfi, Italy
Elena Panteley, France
Manuel Pastor, Spain
Pubudu N. Pathirana, Australia
Francesco Pellicano, Italy
Mingshu Peng, China
Haipeng Peng, China
Zhike Peng, China
Marzio Pennisi, Italy
Matjaz Perc, Slovenia
Francesco Pesavento, Italy
Maria do Rosário Pinho, Portugal
Antonina Pirrotta, Italy
Vicent Pla, Spain
Javier Plaza, Spain
Jean-Christophe Ponsart, France
Mauro Pontani, Italy
Stanislav Potapenko, Canada
Sergio Preidikman, USA
Christopher Pretty, New Zealand
Carsten Proppe, Germany
Luca Pugi, Italy
Yuming Qin, China
Dane Quinn, USA
Jose Ragot, France
Kumbakonam Ramamani Rajagopal, USA
Gianluca Ranzi, Australia
Sivaguru Ravindran, USA
Alessandro Reali, Italy
Oscar Reinoso, Spain
Nidhal Rezg, France
Ricardo Riaza, Spain
Gerasimos Rigatos, Greece
José Rodellar, Spain
Rosana Rodriguez-Lopez, Spain
Ignacio Rojas, Spain
Carla Roque, Portugal
Aline Roumy, France
Debasish Roy, India
Rubén Ruiz García, Spain
Antonio Ruiz-Cortes, Spain
Ivan D. Rukhlenko, Australia

Mazen Saad, France
Kishin Sadarangani, Spain
Mehrdad Saif, Canada
Miguel A. Salido, Spain
Roque J. Saltarén, Spain
Francisco J. Salvador, Spain
Alessandro Salvini, Italy
Maura Sandri, Italy
Miguel A. F. Sanjuan, Spain
Juan F. San-Juan, Spain
Roberta Santoro, Italy
Ilmar Ferreira Santos, Denmark
José A. Sanz-Herrera, Spain
Nickolas S. Sapidis, Greece
Evangelos J. Sapountzakis, Greece
Themistoklis P. Sapsis, USA
Andrey V. Savkin, Australia
Valery Sbitnev, Russia
Thomas Schuster, Germany
Mohammed Seaid, UK
Lotfi Senhadji, France
Joan Serra-Sagrasta, Spain
Leonid Shaikhnet, Ukraine
Hassan M. Shanechi, USA
Sanjay K. Sharma, India
Bo Shen, Germany
Babak Shotorban, USA
Zhan Shu, UK
Dan Simon, USA
Luciano Simoni, Italy
Christos H. Skiadas, Greece
Michael Small, Australia
Francesco Soldovieri, Italy

Raffaele Solimene, Italy
Ruben Specogna, Italy
Sri Sridharan, USA
Ivanka Stamova, USA
Yakov Strelniker, Israel
Sergey A. Suslov, Australia
Thomas Svensson, Sweden
Andrzej Swierniak, Poland
Yang Tang, Germany
Sergio Teggi, Italy
Roger Temam, USA
Alexander Timokha, Norway
Rafael Toledo, Spain
Gisella Tomasini, Italy
Francesco Tornabene, Italy
Antonio Tornambe, Italy
Fernando Torres, Spain
Fabio Tramontana, Italy
Sébastien Tremblay, Canada
Irina N. Trendafilova, UK
George Tsiatas, Greece
Antonios Tsourdos, UK
Vladimir Turetsky, Israel
Mustafa Tutar, Spain
Efstratios Tzirtzilakis, Greece
Francesco Ubertini, Italy
Filippo Ubertini, Italy
Hassan Ugail, UK
Giuseppe Vairo, Italy
Kuppalapalle Vajravelu, USA
Robertt A. Valente, Portugal
Raoul van Loon, UK
Pandian Vasant, Malaysia

Miguel E. Vázquez-Méndez, Spain
Josep Vehi, Spain
Kalyana C. Veluvolu, Korea
Fons J. Verbeek, The Netherlands
Franck J. Vernerey, USA
Georgios Veronis, USA
Anna Vila, Spain
R.-J. Villanueva, Spain
Uchechukwu E. Vincent, UK
Mirko Viroli, Italy
Michael Vynnycky, Sweden
Yan-Wu Wang, China
Junwu Wang, China
Shuming Wang, Singapore
Yongqi Wang, Germany
Jeroen A. S. Witteveen, The Netherlands
Yuqiang Wu, China
Dash Desheng Wu, Canada
Guangming Xie, China
Xuejun Xie, China
Gen Qi Xu, China
Hang Xu, China
Xinggong Yan, UK
Luis J. Yebra, Spain
Peng-Yeng Yin, Taiwan
Ibrahim Zeid, USA
Huaguang Zhang, China
Qingling Zhang, China
Jian Guo Zhou, UK
Quanxin Zhu, China
Mustapha Zidi, France
Alessandro Zona, Italy

Contents

Structural Damage Modelling and Assessment 2014, Anaxagoras Elenas, Yuri Petryna, and Nawawi Chouw
Volume 2015, Article ID 968528, 2 pages

Durability Evolution of RC Bridge under Coupling Action of Chloride Corrosion and Carbonization Based on DLA Model, Haoxiang He, Ruifeng Li, and Kui Chen
Volume 2015, Article ID 951846, 11 pages

Damage Identification of Urban Overpass Based on Hybrid Neurogenetic Algorithm Using Static and Dynamic Properties, Hanbing Liu, Xianqiang Wang, Yafeng Gong, and Yubo Jiao
Volume 2015, Article ID 404675, 10 pages

An Analytical Approach for Deformation Shapes of a Cylindrical Shell with Internal Medium Subjected to Lateral Contact Explosive Loading, Xiangyu Li, Zhenduo Li, and Minzu Liang
Volume 2015, Article ID 563097, 10 pages

Damage Analysis and Evaluation of High Strength Concrete Frame Based on Deformation-Energy Damage Model, Huang-bin Lin, Shou-gao Tang, and Cheng Lan
Volume 2015, Article ID 781382, 10 pages

Dynamic Characteristics of Electrostatically Actuated Microbeams with Slant Crack, Han Zhou, Wen-Ming Zhang, Zhi-Ke Peng, and Guang Meng
Volume 2015, Article ID 208065, 13 pages

Editorial

Structural Damage Modelling and Assessment 2014

Anaxagoras Elenas,¹ Yuri Petryna,² and Nawawi Chouw³

¹*Department of Civil Engineering, Democritus University of Thrace, GR-67100 Xanthi, Greece*

²*Department of Civil Engineering, Technical University Berlin, D-13355 Berlin, Germany*

³*Department of Civil and Environmental Engineering, The University of Auckland, Auckland, New Zealand*

Correspondence should be addressed to Anaxagoras Elenas; elenas@civil.duth.gr

Received 9 July 2015; Accepted 9 July 2015

Copyright © 2015 Anaxagoras Elenas et al. This is an open access article distributed under the Creative Commons Attribution License, which permits unrestricted use, distribution, and reproduction in any medium, provided the original work is properly cited.

Damage modelling and assessment is a growing field of fundamental research and a practical problem at the same time. A rapid progress in damage assessment has become possible due to new mathematical approaches developed in the last years. Combined with efficient computer simulations, they are able to predict structural damage at various scales from micromechanics to real large-scale structures. Recent developments enable efficient structural design, health monitoring, and lifetime management. New approaches to damage simulation and assessment traditionally stay also in focus of the present issue.

H. Liu et al. present a hybrid neurogenetic algorithm-based procedure for damage identification of urban overpass. Change rate of frequency and strain ratio is treated as input parameters. The optimized weight and threshold are incorporated as the initial value of ANNs to identify the structural damage condition. The proposed procedure is able to identify the location and the severity of damage (both for single-damage and for multidamage cases). The numerical technique is applied on the Qianjin Bridge. The results reveal that the proposed method can successfully identify the locations and severities of damage.

X. Li et al. present an experimental investigation on the deformation process of a sand-filled cylindrical shell. One side of the shell experienced a contact explosive load. The shapes of the deformation were analysed. An analytical approach has been developed based on the rigid plastic hinge theory. A significant agreement has been achieved between the calculated and the experimental results. Thus, the analytical approach can be considered as a reliable tool in describing the deformation mechanism and predicting the

deformation shapes of the sand-filled cylindrical shell under a lateral contact explosion.

H. He et al. present an evolution model based on Diffusion-Limited Aggregation (DLA) for the durability analysis, considering the coupling action of the chloride ion erosion and the carbonization. The evolutionary process of the chloride ion erosion, the carbonization, and the coupling action are simulated based on the chloride ion diffusion equation and carbonation depth equation. The DLA model presented has been applied on a reinforced concrete bridge structure.

H. Zhou et al. present an improved model of the slant crack on a microbeam, based on the fracture mechanics theory. The nonlinear performance of microbeams with a bending induced slant crack of different geometry parameters is compared and investigated with regard to the dynamic behaviours. The effects of the slant crack and the electric actuation of an electrostatically actuated fixed-fixed microbeam on the dynamic characteristics are examined in detail. It is concluded that the crack position has more significant influence in the pull-in voltage value than the slant angle or the depth ratio. Approaching the slant crack to the fixed end or enlarging the external incentives will amplify the nonlinearity of the microbeam system, while the effects of depth ratio and slant angle are dependent on the crack position.

H. Lin et al. present a new method based on the deformation-energy for characterizing damage to high strength concrete structures. The material model incorporates several nonlinearities like stiffness and strength degradation under a cyclic loading. The proposed model was

embedded into the IDARC program. An example of a high strength RC multistorey frame was used to evaluate the structural damage under various seismic excitations. The degree of structural damage was predicted satisfactorily.

By compiling these papers, the editors hope that the readers will benefit from the latest development in the field of structural damage modelling and assessment of civil engineering structures.

Anaxagoras Elenas
Yuri Petryna
Nawawi Chouw

Research Article

Durability Evolution of RC Bridge under Coupling Action of Chloride Corrosion and Carbonization Based on DLA Model

Haoxiang He,^{1,2} Ruifeng Li,¹ and Kui Chen¹

¹Beijing Key Laboratory of Earthquake Engineering and Structure Retrofit, Beijing University of Technology, Beijing 100124, China

²Beijing Collaborative Innovation Center for Metropolitan Transportation, Beijing 100124, China

Correspondence should be addressed to Haoxiang He; hxx7856@163.com

Received 18 September 2014; Accepted 12 January 2015

Academic Editor: Anaxagoras Elenas

Copyright © 2015 Haoxiang He et al. This is an open access article distributed under the Creative Commons Attribution License, which permits unrestricted use, distribution, and reproduction in any medium, provided the original work is properly cited.

Chloride attack and carbonization are the main factors which affect the durability of concrete structures, and the respective theoretical models are systematically established. However, the quantitative analysis and models about the coupling effect of chloride attack and carbonization are less, so the precision and level of durability analysis of reinforced concrete are restricted. Diffusion-limited aggregation (DLA) model can finely simulate the process of gas diffusion and condensation with randomness and fractal characteristics, which is suitable for revealing the durability evolution process of the chloride attack, carbonization, and the coupling action in concrete. Based on the principle of DLA, considering the factors such as diffusion depth, concrete properties, and exposure conditions which influence the characteristics of chloride diffusion and carbonization, as well as the coupling effect, an integrated DLA model is established. The concentration of carbon dioxide and chloride at any time and any location can be obtained and dynamically displayed based on the DLA model. The performance predict method for concrete and steel bars considering fatigue effect is presented based on DLA, according to the demand for bridge durability analysis. Numerical examples show that the method can dynamically and intensively simulate the durability evolution process of reinforced concrete bridge.

1. Introduction

Reinforced concrete is an excellent construction material: highly durable, economical, under proper conditions, and semipermanent. However, unsuitable use of reinforced concrete in design or construction is likely to result in low performance and deterioration of the concrete long before the end of its intended service life [1]. Early deterioration of structures increases their maintenance costs and requires them to be rehabilitated or dismantled, thus producing building waste and greatly impacting local and global environments.

In recent years, various reinforced concrete structures worldwide have suffered rapid deterioration. Therefore, the durability of concrete structures, especially those exposed to aggressive environment, is of great concern [2]. Many deterioration causes and factors have been investigated. There are many factors that cause deterioration of reinforced

concrete structures: neutralization, chloride damage, freezing and thawing, chemical corrosion, and alkali-aggregate reactions are often indicated as causes for the deterioration of reinforced concrete structures and each involves the corrosion and expansion of a reinforcing bar, which cracks the concrete and deteriorates the capacity and performance of the structure. The durability of reinforced concrete structure is one of the issues of common concern to civil engineering.

At present, the research on the durability of concrete includes three levels, which are microscopic level, mesoscopic level, and macroscopic level. The focus of microlevel research is the deterioration mechanics and damage rules of hardened cement paste and rebar. The scope of mesoscopic level research refers to the influence of material phase composition and structure on the durability. The scope of macroscopic level research involves the integrated performance and the structural durability evaluation and life prediction, and so

forth. According to the achievements from above levels, the theoretical methods on the concrete structure durability are mainly divided into three types. The first one is mathematical model method, which calculates the evolution of the material parameters directly using the chloride ion diffusion equation and carbonation equation [3, 4]. The second method is numerical analysis, which derives the deterioration process of materials in time-space dimension by specified algorithms. For example, cellular automata algorithm has been proposed according to the given local rules [5]. The third method is the finite element method; the 3D model of reinforced concrete structures are usually created by the multiphysics coupling finite element software such as ANSYS and COMSOL, and the materials or the structures are simulated precisely [6]. Though extensive research is conducted on the durability of concrete structures, there are also many respective limitations in each type of method at present.

As a key type of infrastructure in civil engineering, bridge is an important part of the national transportation system, and the reinforced concrete bridge is the most common form in highway bridges. Due to the rigorous environment and the insufficient measurement of construction and maintenance worldwide, the durability of a great many reinforced concrete bridges reduced rapidly, the normal operation and safety are affected [7]. Therefore, the analysis and evaluation of the durability of the reinforced concrete bridge has become an important problem in engineering research.

The durability of the reinforced concrete bridge mainly involves the chloride ion erosion, the carbonation of concrete, and the reinforcement corrosion caused by the above factors and these factors are mainly affected by the diffusion depth, the characteristics of concrete, and the exposure conditions. Until now, the study on the durability degradation due to the single environmental factor such as carbonation and chloride ion penetration of reinforced concrete structure has been thoroughly developed [8]. However, it is worth noting that the actual durability of the concrete structure degradation in practical conditions is the long-term and coupling action of many factors in load, environment, and climate. The combined results are different with the law from a single factor, but the relevant research results and analysis methods, especially those that can be applied in the actual model or equations, are still very limited [9, 10].

In view of the above deficiency in the corresponding research limitations, a numerical analysis model based on diffusion-limited aggregation (DLA) is proposed, in order to reveal the coupling effect about the chloride ion erosion and concrete carbonization on the macroscopic capacity deterioration of the reinforced concrete structures. The change of the concrete and steel rebar in the microlevel, the evolution of the chemical composition and the interaction between the transmission performances in the mesoscopic level, and the durability in the macrolevel are studied. Finally, the chloride ion concentration and the carbonation degree on any location and at any time can be predicted; furthermore, the structural durability can also be calculated and the optimization strategy for maintenance can be provided.

2. Diffusion-Limited Agglomeration

Stochastic models of fractal growth have inspired a number of studies and applications in applied sciences, and the best known model is the diffusion-limited aggregation (DLA). DLA has been extensively employed since its proposition in 1981 by Witten and Sander to model cluster growth controlled by the random process of diffusion [11].

The basic model operates according to the following basic rule. The initial starting point for the growing cluster is fixed, so that the primary cluster consists of a single particle. At every step another particle is attached to the cluster according to some rule so that the cluster remains connected with respect to some neighboring relationship. This is replicated on every new step until the cluster reaches the predetermined size.

The mathematical description of the DLA model is as follows: on the system point group, fixed in a certain location layout particles as the initial state. From that position, different particles are produced once certain threshold value is surpassed, and the particles will move randomly until they are adsorbed by other fixed particles. The adsorption principle is as follows: in four nearest neighbors (up, down, left, and right lattice) that are fixed in particles, the movement of the particles will be adsorbed. And then a particle is produced, and a calculation is done according to the above rules. So it will be a coherent set design. The neighbors in DLA model are not equally likely to be attached to the cluster. Instead, the next particle is chosen among all neighbors with a distribution proportional to the equilibrium electrostatic potential on the boundary of the existing cluster, which is the solution of $\Delta u = 0$ where $\Delta = \nabla^2$ is the Laplace operator. Therefore, DLA captures the essential features of a typical dynamic growth process that is related to the Laplace equation. If the particles on the random walk are beyond the scope of limit state matrix, then the corresponding boundary condition treatment scheme should be considered as (1) the periodic boundary conditions, the particle will not escape, and it will produce a new particle after the old particle is adsorbed; (2) the absorption boundary condition, the particle will be given up when it is beyond the border and a new particle generates.

The advanced features of the DLA model are as follows: (1) with a very simple algorithm, the DLA embody the primary components in a wide range of natural phenomena but the physical mechanism does not need clear forms; (2) the self-similar fractal structure with invariance scale can be generated through a simple kinematics and dynamics process, and the mechanism of fractal growth in practical system is revealed in certain extent; (3) the interface has complex shape and instability, and the growth process is a process far from equilibrium dynamics, but cluster structure is stable and has determined fractal dimension. For more than 20 years, researchers with great interest in the mechanism of DLA model carried out extensive study, and rich theoretical research results are obtained, and the achievement is applied in the fields including fractal physics, environmental science, materials science, and urban planning [12].

The applications of diffusion-limited agglomeration theory in civil engineering are very few; in this paper, the particles are used to simulate the chemical material in microlevel, and the arrangement is controlled by the algorithm of DLA. The concentration of chlorine ion and carbon dioxin in the corresponding depth can be calculated according to the theoretical formula; thus a determined number of particles which randomly move in the horizontal direction are placed in the concrete. Hence, the randomness in the location and the precision in the calculation are simultaneously embodied through DLA model. In addition, the tiny cracks will occur when the reinforced concrete beam is subjected to the bending moment, and the chloride ion erosion and the carbonization will aggravate near the cracks, and the coupling phenomenon can be simulated in detail by the mutual adsorption display function in the DLA model. The durability analysis based on the diffusion-limited aggregation has important research significance and broad application prospects.

3. Chloride Ion Erosion Based on the DLA

If the pore distribution in concrete is assumed to be uniform, the chloride ions do not react with concrete, and the relative concrete exposed surface is a semi-infinite medium body; thus the chlorine ion in the intrusion of saturated concrete meet the second Fick diffusion law [2]. The one-dimensional diffusion equation is as follows:

$$\frac{\partial C}{\partial t} = D \frac{\partial^2 C}{\partial x^2}, \quad (1)$$

where t is the time of chloride ion erosion, x is the distance from the concrete surface to the specified location, c is the chloride ion concentration on the specified location, and D is the chloride ion diffusion coefficient. The initial condition is $C(x, 0) = 0$, and the boundary condition is $C(0, t) = C_s$ and $C(\infty, t) = C_0$. The solution of (1) is

$$C = C_0 + (C_s - C_0) \left[1 - \operatorname{erf} \frac{x}{2\sqrt{Dt}} \right], \quad (2)$$

where C_0 is the initial concentration of chloride ions in concrete, and C_s is the chloride ion concentration on the exposed surface, and $\operatorname{erf}(z)$ is the error function written as follows:

$$\operatorname{erf}(z) = \frac{2}{\sqrt{\pi}} \int_0^z \exp(-u^2) du. \quad (3)$$

For the chloride ion diffusion process in complex condition, especially for the chloride ion diffusion based on the principle of diffusion-limited aggregation [13], the diffusion

model considering multiple factors is advised to be written as follows:

$$C_f = C_0 + (C_s - C_0) \cdot \left[1 - \operatorname{erf} \left(x \cdot \left(2 \sqrt{\frac{KD_0 T t_0^m}{(1+R)(1-m)T_0} e^{q[1/T_0 - 1/T]} t^{1-m}} \right)^{-1} \right) \right], \quad (4)$$

where c_t is the total chlorine ion concentration at t moment in the location which has the distance x from the surface, c_b is the combination of chlorine ion concentration, and c_z is the free chlorine ion concentration. R is the chloride ion combining ability, and $R = c_b/c_z = (c_t - c_z)/c_z$. m is the experimental constant, K is the degradation effect coefficient for the performance of concrete chloride ion diffusion, T is temperature, D_0 is the chloride ion diffusion coefficient on temperature T_0 , and t_0 is the concrete hydration age for q is the activated constant, which associated with water cement ratio [14]; when $m_w/m_c = 0.4$, q is 6000 K, when $m_w/m_c = 0.5$, q is 5450 K, and when $m_w/m_c = 0.6$, q is 3850 K.

The chlorine ion concentration in the location which has the distance x from the surface can be calculated according to (4); thus, the corresponding number of chloride ions which moves at random in the horizontal direction can be arranged in the location of x , by using the theory of diffusion-limited aggregation. When the chloride ions approach others, adsorption will occur and the combination of the chloride ion diffusion equations and the DLA algorithm is realized.

According to the above basic idea, the flow chart of DLA model considering the chloride ion erosion calculation is proposed, as shown in Figure 1.

Assuming the concrete surface chloride ion concentration is known as 2.0 Kg/m^3 , the original concentration of chloride ion in concrete was 0.01 Kg/m^3 and the concrete hydration age is 28 days. The protective layer thickness is 35 mm, the diameter of the steel bar is 25 mm, the water cement ratio is 0.4, and the temperature is 20 degrees Celsius; the diffusion coefficient can be obtained through the experiment, and $2.5 \times 10^{-11} \text{ m}^2/\text{s}$ is determined in this study. When the chloride ion erosion time is 10 years, the chloride ion erosion model based on DLA simulation results is shown in Figure 2. It is obvious that the DLA model can intensively reveal the randomness and uncertainty in the process of chloride ion erosion in concrete, and it can simultaneously reflect the concentration variation and performance evolution in the process of chloride ion propagation accurately.

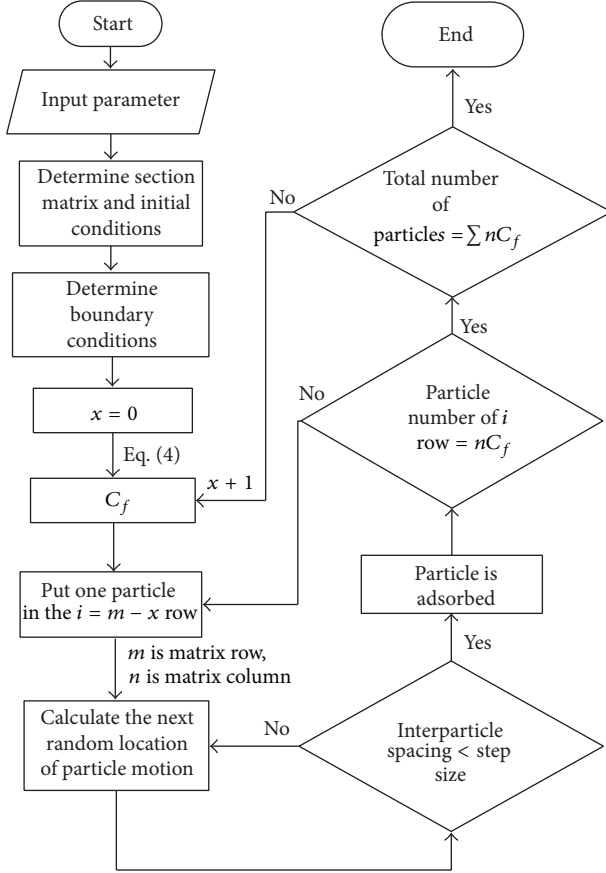


FIGURE 1: Flow chart of chloride attack in the DLA model.

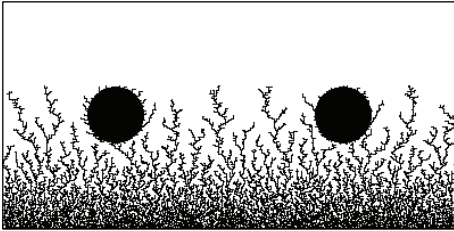


FIGURE 2: Chloride attack in 10 years based on DLA.

4. Reinforcement Corrosion under Chloride Ion Erosion

The chloride ion erosion accumulates in the concrete under severe conditions, and the corrosion will occur in the reinforcement bar when the chloride ion concentration reaches a critical value. There are two criteria to predicate the critical concentration, one is the chloride ion concentration, and the other is the ratio of chloride ion to hydroxide ion, that is, $[Cl^-/OH^-]$. A new criteria was proposed to apply in engineering structures; for a new structure, 0.6 Kg/m^3 is defined, and 0.6 Kg/m^3 – 0.9 Kg/m^3 can be chosen for important existing structures, and 1.0 Kg/m^3 is for normal structures [15]. In this paper, 0.6 Kg/m^3 is defined as the critical concentration. The exposure condition of the case is

in offshore atmospheric environment which is about 0.1 km far from the sea, and the average chloride concentration on concrete surface is 3.0 Kg/m^3 based on empirical data. Assuming that the chloride ion concentration on the concrete surface is 3.0 Kg/m^3 , other parameters are the same as the previous section. The initial corrosion time is 9 years according to (4), and the destruction process of concrete structure is shown in Figure 3 as the DLA algorithm is used.

The quantity formula of the reinforcement corrosion in the corrosion time t is as follows:

$$\Delta g = \frac{NS \int i_{\text{corr}} dt}{F}, \quad (5)$$

where N is the molar mass of the reinforcement, and $N = g/n$; F is Faraday constants, and $1F = 96500 \text{ C/mol} = 26.8 \text{ A-h/mol}$. S is the surface area of the reinforcement in the concrete and the unit is cm^2 ; i_{corr} is the corrosion current density and the unit is A/cm^2 .

After considering the comprehensive function of factors such as chloride ion concentration, layer resistance, and temperature, the corrosion current density model is obtained by the regression analysis of the test results as follows:

$$\ln 1.08i = 8.37 + 0.618 \ln 169Cl - \frac{3034}{T} - 0.000105R_c + 2.32t^{-0.215}, \quad (6)$$

where i is the corrosion current density and the unit is $\mu\text{A/cm}^2$. Cl is the chlorine ion around the reinforcement and the unit is Kg/m^3 ; T is degree Fahrenheit; R_c is the resistance of concrete cover and the unit is Ω ; t is the time after rust begin and the unit is year.

The average corrosion rate based on the corrosion amount of the reinforcement is given by

$$\eta = \frac{\Delta g}{g_0} = \frac{NS \int i_{\text{corr}} dt}{Fg_0}, \quad (7)$$

where g_0 is the original quality of the rebar.

After studying the bending test of the reinforced concrete members under the coastal environment, the following model of steel corrosion current density is presented as [16]

$$i_{\text{corr}}(t) = 0.3683 \ln(t) + 1.1305. \quad (8)$$

Substituting (6) into (7) gives

$$\eta = \frac{\Delta g}{g_0} = \frac{NS \int (0.3683 \ln(t) + 1.1305) dt}{Fg_0}. \quad (9)$$

5. Corrosive Cracks Analysis under Chloride Ion Erosion

The reinforcement corrosion can cause the rust expansion and the cracking and spalling in the concrete cover, furthermore, inducing the deterioration of the structural bearing capacity and durability. The study on the cover-cracking

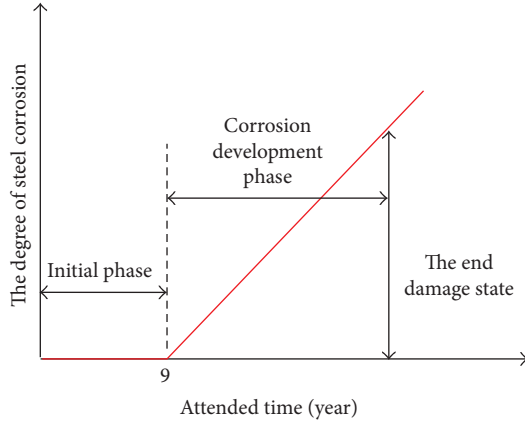


FIGURE 3: Corrosion process under chloride attack.

induced by steel corrosion mainly focuses on the early stage, and less research is carried out for the damage mechanism after the corrosion cracking. Because the corrosion state should be determined in the case of nondestructive operation in the actual engineering, the relationship between the corrosion rate and the corrosive crack width is necessary to the durability evaluation. At present, the corresponding function can be obtained by the methods, including normal test, elastic mechanics method, and finite element method (FEM), and mostly through the experienced formula of the accelerated corrosion experiments.

François and Arliguie [17] and Vidal et al. [18] focused on the effects on cracks to the reinforcement corrosion in reinforced concrete structure and established the life prediction models based on crack width and steel cross-sectional loss. Arya and Wood [19] studied the effect of crack spacing and different forms of cracks to the corrosion, and the cracks are divided into the lateral cracks, vertical cracks, live cracks, and dormant cracks; furthermore, the impact of different types of steel corrosion cracks was studied.

Assuming the reinforced depth rusty and crack width have a linearly proportional relationship and they are independent of the bar diameter, the cover thickness, the concrete strength, and other parameters; the equation on the steel corrosion rate and the corrosive crack width of concrete can be expressed in the form based on the impressed current accelerated corrosion of corrosive test according to [20] as

$$\eta_s = 4 \left[\frac{1}{d} (0.222w - 0.011) - \frac{1}{d^2} (0.222w - 0.011)^2 \right], \quad (10)$$

where η_s is the rebar corrosion rate, d is the rebar diameter, and w is the corrosive crack width of concrete.

Assuming the material parameters are as stated above, the concrete chloride ion erosion model considering the corrosive cracks is established based on DLA algorithm and the formula above, as shown in Figure 4. It is obvious that the chloride ion erosion model based on DLA can dynamically reveal the diffusion state of chloride ions at different time points and the shape of the apparent derivative corrosion

crack. Compared with the existing simulation methods, the DLA model has the advantages in the fineness, the accuracy, the computational efficiency, and the dynamic display.

6. Carbonation Analysis Based on DLA

As same as the chloride ion erosion, the concrete carbonation is also an important factor for the durability deterioration of the material and reinforced structure. Carbonation is the result of the carbon dioxide diffuse from the environment of the concrete inside, usually changing the chemical composition and organization of concrete structure and the mechanical properties of concrete vary significantly.

Peter et al. [21] theoretically analyzed the carbonation reaction and provide a general theory for carbonation assessment. Papadakis et al. [22] deduced the classic experiment carbonation coefficients according to the content of minerals and cement hydration products. Baroghel-Bouny [23] established a model based on high concentrations of carbonation of concrete porosity and water saturation rate, thus providing a theoretical basis for on-site testing for carbonation. Saetta and Vitaliani [24] and Isgor and Razaqpur [25] established the uncracked concrete carbonation established theoretical model according to the mathematical theory and finite element method. In addition, Song et al. [26], Alahmad et al. [27], and Niu [28] systematically analyzed the effect of the cracks on the carbon dioxide transport and studied the cracking concrete carbonation process and carbonation models.

The theory on the concrete carbonation can be studied based on diffusion theory, and the assumptions are as follows: (1) the carbon dioxide concentration in the concrete is linear distribution; (2) the carbon dioxide concentration on the concrete surface is equal to the concentration of the external environmental condition and the concentration of noncarbonation area is 0; (3) the quantity of unit volume to absorb carbon dioxide is a constant value.

Under these assumptions, the concrete carbonation process follows Fick's first law of diffusion, and the formula for calculating the concrete carbonation depth can be derived as follows:

$$X = \sqrt{\frac{2D_{CO_2}C_{CO_2}}{M_{CO_2}}} \sqrt{t}, \quad (11)$$

where X is the carbonation depth, D_{CO_2} is the effective diffusion coefficient of the carbon dioxide in concrete, and C_{CO_2} is the concrete surface carbon dioxide concentrations. M_{CO_2} is the absorption amount of the carbon dioxide in unit volume concrete and t is the carbonization time.

On the grounds of the theoretical model of concrete carbonation, a modified carbonation depth model is presented, and two major acting factors including the environmental conditions and the concrete quality are considered in the model. Besides, other factors such as the carbonation location, the casting surface, and the working stress are also

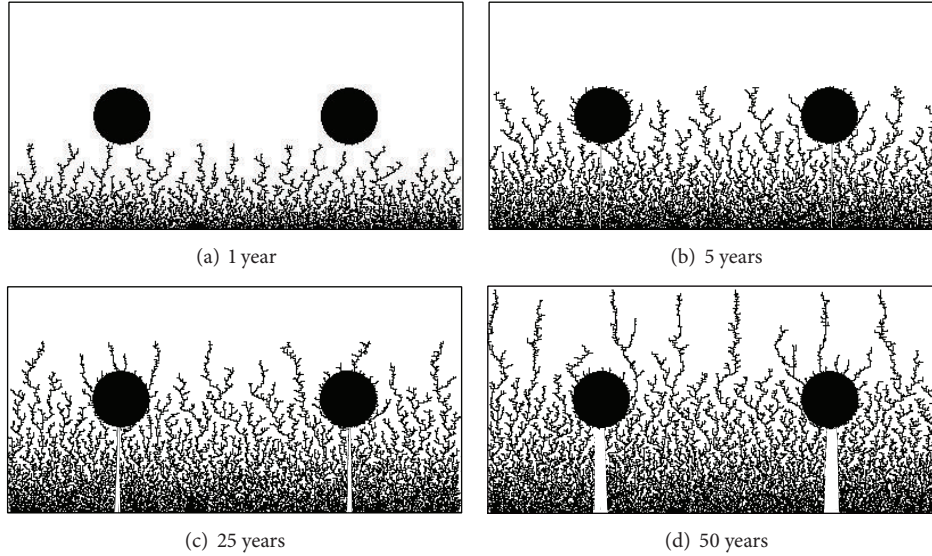


FIGURE 4: DLA evolution model for chloride attack.

involved [26–28]. The stochastic forecasting model is given by

$$X_c = K_{mc} \cdot k_j \cdot k_{co_2} \cdot k_p \cdot k_s \cdot K_e \cdot K_f \sqrt{t}, \quad (12)$$

where K_{mc} is the random variable which represents the difference between the carbonation model calculation and the actual test; at the same time, some other minor random factors are also included. k_j is the correction coefficient on concrete corner, taken as 1.4 for corner and 1.0 for normal location. k_{co_2} is the efficient for carbon dioxide concentration; k_p is the correction coefficient for casting surface, taken as 1.2 for the casting surface and 1.0 for normal surface. k_s is the influence coefficient for working stress, taken as 1.1 for the concrete in tension, and 1.0 for the compressed concrete. K_e is the environment influence coefficient and K_f is the influence coefficient for concrete quality.

For the carbonation model using diffusion-limited aggregation algorithm, the modified carbonation depth can be calculated by (12), and the carbon dioxide concentration in the location which is x far from the surface can be deduced, supposing the carbon dioxide concentration in concrete is linear distribution. In the DLA model, the corresponding amount of carbon dioxide is arranged to be in random motion and these carbon dioxide particles will adsorb together once their mutual distance is less than the given value.

Assuming the carbonization time is 1 year, 10 years, 25 years, and 50 years, respectively, the concrete strength is 20 Mpa, the temperature is 21 degrees Celsius, and the relative humidity is 0.8. The efficient for carbon dioxide concentration is 1.5, the protective layer thickness is 35 mm, and the diameter of rebar is 25 mm. The carbonation model based on DLA is shown in Figure 5. It is apparent that the concrete carbonation based on DLA model can simulate the all evolutionary process and display the carbonizing state at different time points, perfectly having both accuracy and randomness.

7. DLA Model for Coupling Action of Chloride Ion Erosion and Carbonization

In actual environment, the decrease of structural performance due to the deterioration of the durability is usually the integrated consequence of multiple factors such as variable loads, climate, and service conditions. The deterioration process is not the simple superposition of each single factor but the interaction and accumulation of all the factors; this phenomenon causes the concrete deterioration which is more complicated and the related conclusions and experience formula based on the single factor effect have certain limitations. Thus, study on the durability under multiple factors is more intricate.

The study on the carbonization reaction can destruct the original filtering mechanism in the basal body of concrete [29] and promote the Friedel salt decomposition, and the chloride ion content increases. The carbonization can slightly reduce the chloride ion diffusion coefficient, and the chloride ion concentration has a maximum in the carbide cutting edge [30]. The experiments on the coupling effect of carbonation and chloride ion erosion are generally carried out considering limited factors and the specific conditions. The common qualitative conclusion is that the chloride ion concentration has less effect on the depth of carbonation but the carbonization can evoke the decline of the alkalinity in the pore solution, and the corrosion of the rebar placed on the carbonated concrete under the erosion of chloride ion will be more serious. Hence, the effect of carbonization on the chloride ion erosion is more obvious, which has more related factors.

The theoretical model and achievement of the coupling effect of carbonation and chloride ion erosion are little. Beaudoin [31] proposed the modified coefficient of the chloride ion diffusion under carbonation; the total chlorine ion content will increase under the carbonation; that is, the constrained chloride ion content on the surface is proportional

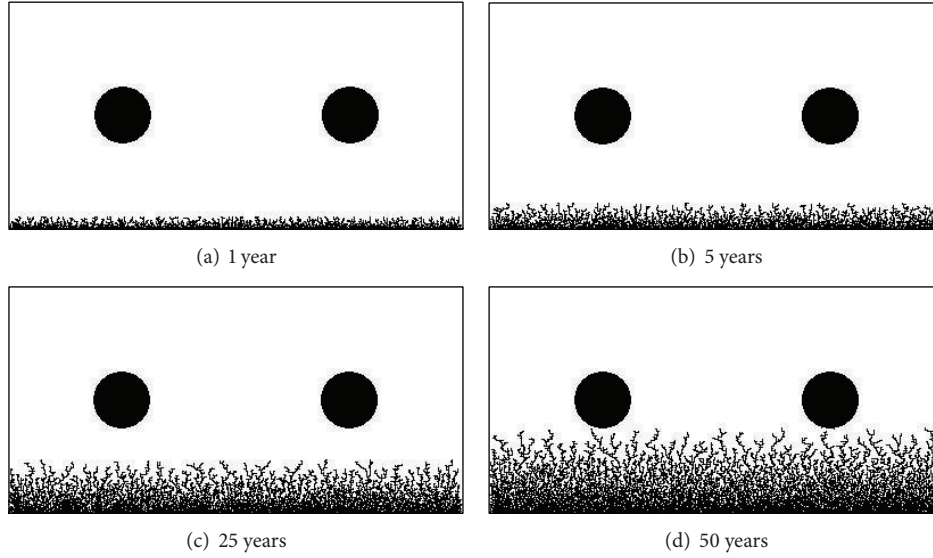


FIGURE 5: DLA evolution model for carbonation.

to the relative increased free chloride ion content, and the modified carbonation coefficient is given by

$$\alpha = \frac{Cl_{lib}^-}{Cl_{lib}^- + Cl_{free}^-} = \frac{C'_s - C_s}{C'_s}, \quad (13)$$

where α is the carbonation modified coefficient, Cl_{lib}^- is the free chlorine ion content under the action of carbonation, Cl_{free}^- is the original free chlorine ion content, C_s is the original chloride ion concentration on the concrete surface, and C'_s is the chloride ion concentration on the concrete surface under carbonation.

The concentration of the internal free chloride ion is assumed to be higher than the concentration of the outside free chloride ion under carbonation action, and the internal free chloride ions will spread to the external environment; thus a modified factor β is introduced as follows:

$$C'_s = \frac{\beta C_s}{1 - \alpha}. \quad (14)$$

In this assumption, the chloride ion erosion depth is constant due to the fact that the carbonation depth is irrelevant to the carbon concentration on the concrete surface. However, the chloride ion erosion depth can actually increase and the initial corrosion time will be reduced; thus, the formula on the modified erosion depth is adopted as follows:

$$I_{cl,ca} = \frac{\left(1 - \sqrt{c_{crit}/c'_s}\right)^2}{\left(1 - \sqrt{c_{crit}/c_s}\right)^2}, \quad (15)$$

where c_{crit} is the chloride ion concentration of the location whose distance from the surface is x .

According to the above discussion, the DLA model on the chloride ion erosion and the DLA model on the concrete carbonation can be combined and calculate the comprehensive

damage and deterioration. The flow chart of DLA considering coupling action is shown in Figure 6. By determining the modified coefficient of carbonation, the surface chloride ion concentration under the carbonation action and chloride ion erosion depth can be calculated simultaneously. Thus, the coupling DLA model on both chloride ion erosion and carbonation can be established.

Assuming the example parameters are still as stated earlier, the influence coefficient of the carbon dioxide concentration is 1.5, and the evolution results obtained from the coupling model are shown in Figure 7. Compared with the results in Figure 4, it can be seen that the severity of the carbonation and the chloride ion erosion aggravates after considering the coupling effect, and the corrosive crack width which is induced by the chloride ion erosion in the concrete will obviously enlarge.

These results indicate that the durability degradation phenomenon can be precisely simulated considering the coupling action of both the chloride ion erosion and the carbonization, and DLA method has better ability than traditional methods. In addition, the chloride ion concentration increases with the chloride ion erosion depth and the chloride ion erosion is the primary factor and the influence of the carbonation is less, especially for the environment where the chlorine ion concentration is higher, such as the coastal region. Hence, only the effect of the carbonization on the chloride ion erosion is usually discussed and studied.

8. Durability Analysis for Bridge under Coupling Effect and Fatigue Condition

The reinforced bridges in service are subjected to coupling effect of the chloride ion erosion and the carbonization, so it is suitable to carry out the durability analysis by using the

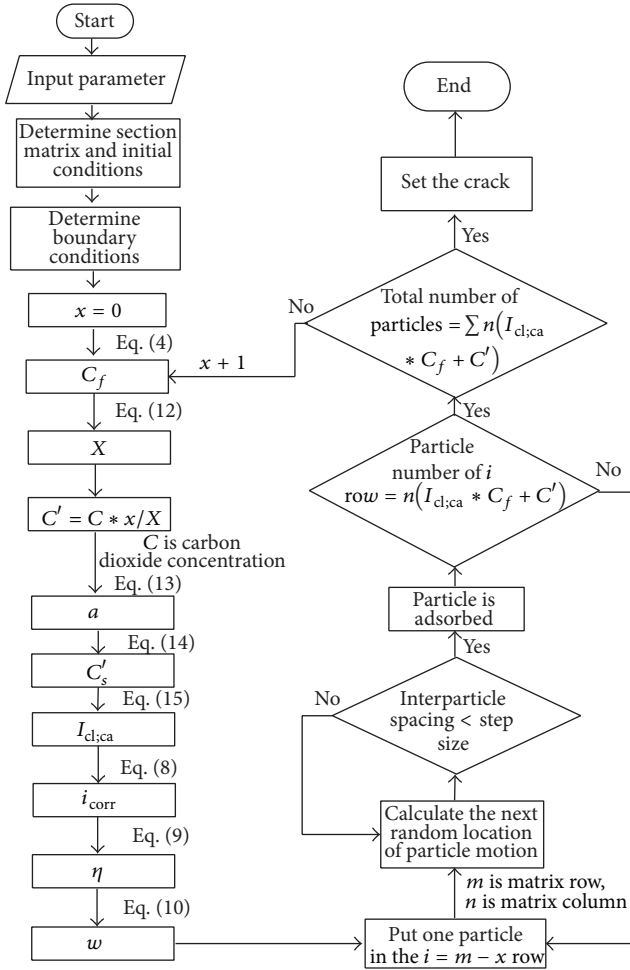


FIGURE 6: DLA flow chart of coupling action.

coupling DLA model proposed in this study. In addition, due to the reinforced concrete bridges bear also bear the effect of traffic load, the fatigue failure will occur under the action of cyclic loading although the actual stress is less than the yield strength. The rebar corrosion induced by the coupling effect of the chloride ion erosion and carbonization can not only reduces the effective cross section but also increases the fatigue stress amplitude; at the same time the steel fatigue strength decreases; thus, the service life of the structure will seriously shorten.

Therefore, for the reinforced concrete bridges under the condition of traffic load and complicated environment, the study on the time-varying fatigue durability considering the coupled action of chloride ion erosion and carbonization is significant.

In the effect of the chloride ion erosion, the corrosion rate will increase and the stress concentration will arise from the partial dents on the rebar. Under fatigue load, the chloride ion diffusion rate increases, the corrosion aggravates, and the fatigue resistance degrades. According to the data from the reinforcement degradation test with different corrosion

states, the time-varying model for the corrosion depth and fatigue strength [32] is concluded as

$$\varphi(t) = \begin{cases} 1.066 & \Delta\delta < 1.23 \text{ mm} \\ 1.066 - 0.002e^{2.859\Delta\delta(t)} & \Delta\delta \geq 1.23 \text{ mm,} \end{cases} \quad (16)$$

where $\varphi(t)$ is the steel fatigue strength coefficient; $\Delta\delta$ is the reinforcement corrosion depth, which can be obtained from the rebar corrosion rate. According to (10)–(16) and simulated results from the coupling DLA model, the reinforced time-varying fatigue strength and the integral durability index can be calculated.

In order to verify the accuracy of the method in this paper, a simply supported reinforced concrete highway bridge with T section is chosen as an example, and the cross section diagram is shown in Figure 8. The span is 16 m, the axial compression strength of the concrete is 20.7 N/mm^2 , and protective layer thickness is 30 mm. The yield strength of the rebar is 235 N/mm^2 , 12 rebars are set in the beam bottom, the diameter of the six main rebar is 32 mm, and the diameter of other rebar is 16 mm. The surface chloride ion concentration of the concrete is 3.0 Kg/m^3 , and the original chloride ions concentration in the concrete is 0.01 Kg/m^3 , the concrete hydration age is 28 days, the water cement ratio is 0.4, the environmental temperature is 20 degrees Celsius, and the humidity is 0.8. The diffusion coefficient can be obtained through the experiment, and $2.5 \times 10^{-11} \text{ m}^2/\text{s}$ is assumed in this study. The carbon dioxide concentration influence coefficient is 1.5.

The action time for the environmental factors and fatigue load is from 1 year to 50 years, and the evolutionary process of the material performance of the main sections is calculated based on the coupling DLA model, considering the effect of both the chloride ion erosion and carbonization. The concrete carbonation, chloride ion erosion, and the corrosive crack propagation state of the midspan cross section after 25 years are shown in Figure 9. It can be seen that the cracks in the midspan cross section grown rapidly after the bridge served 25 years and the maximum width has been larger than the limit value 0.3 mm; thus major repair should adopt for the upper structure. Furthermore, it is verified that the DLA model can integrate the theoretical equations and simulation algorithm, and the coupling evolution process of the chloride ion erosion and carbonization can be dynamically and continuously displayed. Hence, the DLA model is appropriate for the engineering application.

The evolutionary process of the chloride ion concentration on the surface of the rebar located at the bottom of the cross section is shown in Figure 10. The evolution process about the concrete carbonation depth distribution is shown in Figure 11. The development trend about the rebar corrosion rate and the fatigue strength reduction coefficient of the rebar located at the bottom of the cross section under different service time is shown in Figures 12 and 13, respectively.

According to the results and comprehensive analysis, it can be seen that the increment speed of both the chloride ion concentration on the surface of the rebar and the concrete carbonation depth will diminish with the service time, and the fatigue strength of the rebar will reduce in the corrosion

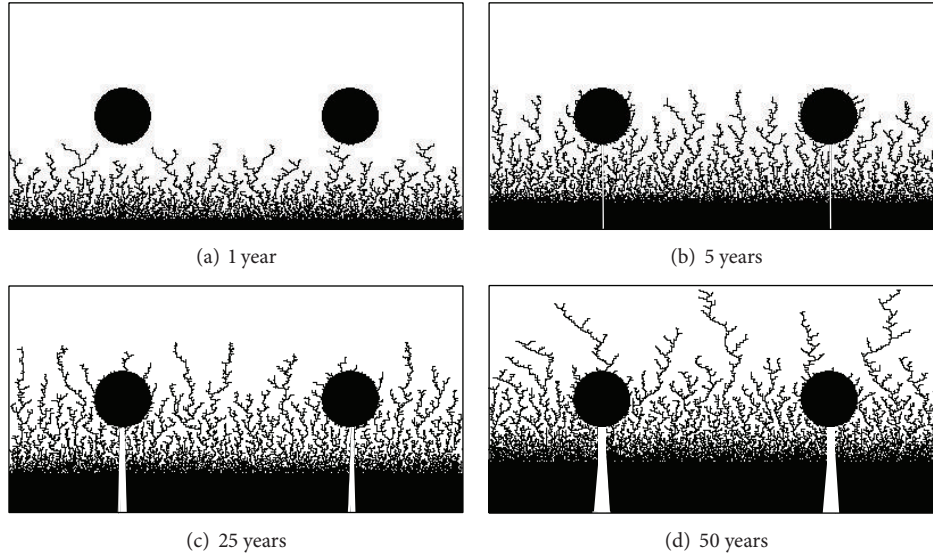


FIGURE 7: DLA evolution model for coupling action.

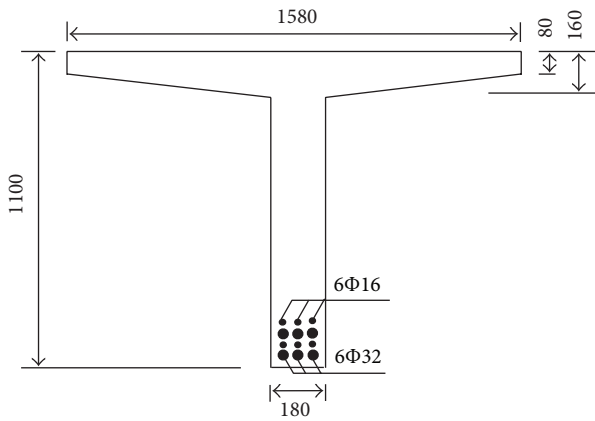


FIGURE 8: Section of T type RC beam.

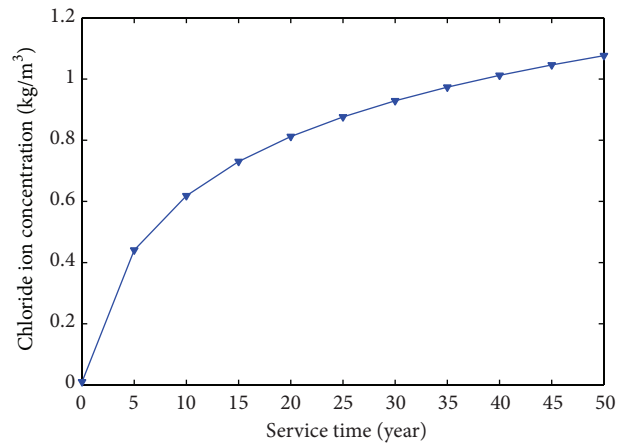


FIGURE 10: Evolutionary process of chloride concentration.

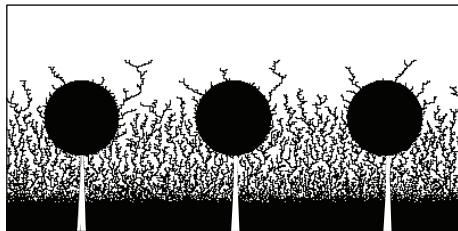


FIGURE 9: Evolutionary results for coupling action in 25 years.

environment induced by the chloride ion erosion. The rebar in the T type beam began to rust in the 9th service year, and the corrosive cracks gradually expand under fatigue loads and environmental factors. The general durability of the bridge significantly decline until the 20th service year and necessary maintenance and repair strategy should be adopted.

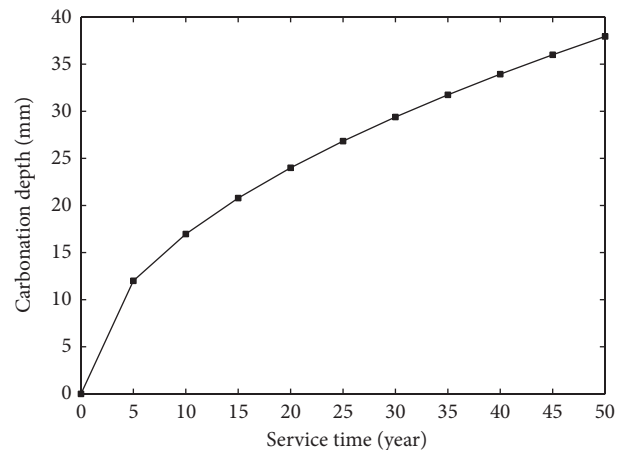


FIGURE 11: Evolutionary process of carbonation depth.

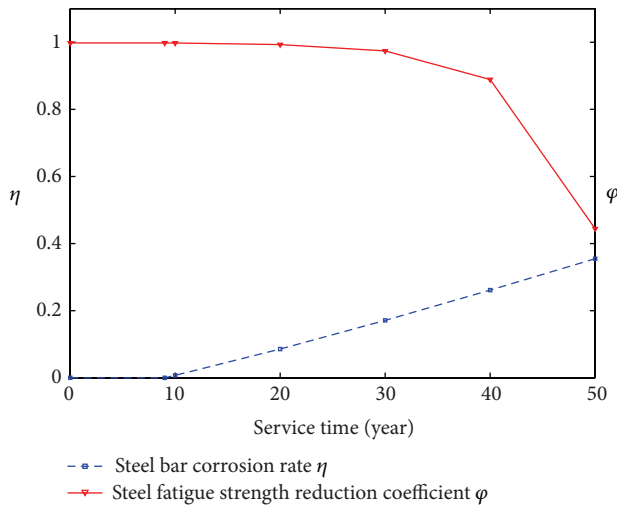


FIGURE 12: Rebar corrosion rate and fatigue strength reduction coefficient evolutionary process.

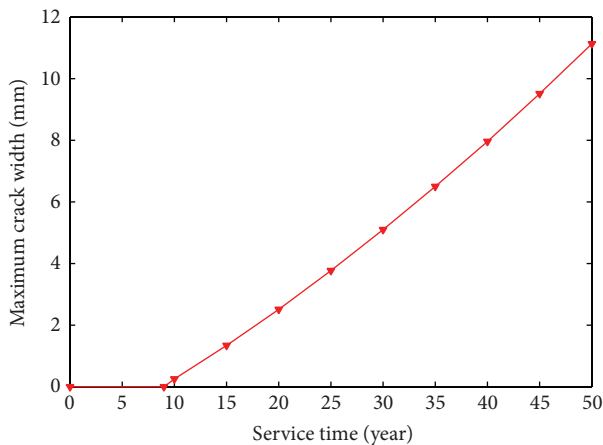


FIGURE 13: Evolutionary process of maximum width of cracks.

9. Conclusions

In this paper, an evolution model based on diffusion-limited aggregation is presented for the durability analysis of the reinforced concrete bridge, and the coupling action of the chloride ion erosion and the carbonization is considered. The evolutionary process of the chloride ion erosion, the carbonization, and the coupling action is simulated based on the chloride ion diffusion equation and carbonation depth equation.

The DLA model can meet the actual conditions of the diffusion of the chloride ion and carbon. Meanwhile, it also embodies the randomness by using the diffusion-limited aggregation principle. In addition, the DLA model can simulate the evolutionary process of microcracks, especially for the reinforced concrete structure subjected to bending moment, chloride ion erosion, and carbonation.

The DLA model can be used to simulate the concrete cracks of steel bar under the corrosive action according to

the formula about the rebar corrosion rate and corrosive action, and the results are detailed and precise.

Through the relationship between the corrosion depth and the fatigue strength reduction, the fatigue strength under the coupling of the chloride ion erosion and the carbonization can be calculated, and the phenomena are also revealed by the DLA model. In general, the DLA model can be utilized to analyze the durability of the reinforced concrete bridge in all the service period.

It should be pointed out that there are many aspects need to be further studied in performance simulation by the DLA model, such as the application of the multidimensional diffusion equations, and the differences in different cross sections and lateral sections, and the effect on bond-slip effect between rebar and concrete in the final service time.

Conflict of Interests

The authors declare that there is no conflict of interests regarding the publication of this paper.

Acknowledgments

This work is partially supported by Natural Science Foundation of China under Grants nos. 51478024 and 51108009 and Foundation of Beijing Key Lab of Earthquake Engineering and Structural Retrofit under Grant no. USDE201403.

References

- [1] H. Bohni, *Corrosion in Reinforced Concrete Structures*, Woodhead Publishing Limited, Abington, UK, 1st edition, 2005.
- [2] V. S. Ramachandran and J. J. Beaudoin, *Handbook of Analytical Techniques in Concrete Science and Technology: Principles, Techniques, and Applications*, Noyes Publications, 1st edition, 2001.
- [3] K. Takewaka, T. Yamaguchi, and S. Maeda, "Simulation model for deterioration of concrete structures due to chloride attack," *Journal of Advanced Concrete Technology*, vol. 1, no. 2, pp. 139–146, 2003.
- [4] T. Ishida and C.-H. Li, "Modeling of carbonation based on thermo-hygro physics with strong coupling of mass transport and equilibrium in micro-pore structure of concrete," *Journal of Advanced Concrete Technology*, vol. 6, no. 2, pp. 303–316, 2008.
- [5] J. S. Zhu and L. K. He, "Cellular automata-based chloride ion diffusion simulation of concrete bridges under multi-factor coupling actions," *Journal Wuhan University of Technology, Materials Science Edition*, vol. 27, no. 1, pp. 160–165, 2012.
- [6] O. B. Isgor and A. G. Razaqpur, "Finite element modeling of coupled heat transfer, moisture transport and carbonation processes in concrete structures," *Cement and Concrete Composites*, vol. 26, no. 1, pp. 57–73, 2004.
- [7] N. M. Okasha and D. M. Frangopol, "Advanced modeling for efficient computation of life-cycle performance prediction and service-life estimation of bridges," *Journal of Computing in Civil Engineering*, vol. 24, no. 6, pp. 548–556, 2010.
- [8] M. S. Darmawan and M. G. Stewart, "Spatial time-dependent reliability analysis of corroding pretensioned prestressed concrete bridge girders," *Structural Safety*, vol. 29, no. 1, pp. 16–31, 2007.

- [9] W. Puatatsananon and V. E. Saouma, "Nonlinear coupling of carbonation and chloride diffusion in concrete," *Journal of Materials in Civil Engineering*, vol. 17, no. 3, pp. 264–275, 2005.
- [10] P. Chindaprasirt, S. Rukzon, and V. Sirivivatnanon, "Effect of carbon dioxide on chloride penetration and chloride ion diffusion coefficient of blended Portland cement mortar," *Construction and Building Materials*, vol. 22, no. 8, pp. 1701–1707, 2008.
- [11] T. A. Witten and L. M. Sander, "Diffusion-limited aggregation, a kinetic critical phenomenon," *Physical Review Letters*, vol. 47, no. 19, pp. 1400–1403, 1981.
- [12] S. Q. Chishty, F. Mazhar, B. B. Rajshaikh, and K. Mohd, "Fractal deposits on limestones due to diffusion limited aggregation," *Journal of Chemical, Biological and Physical Sciences*, vol. 4, no. 3, pp. 2549–2554, 2014.
- [13] H.-F. Yu, W. Sun, H.-Y. Ma, and L.-H. Yan, "Diffusion equations of chloride ion in concrete under the combined action of durability factors," *Journal of Building Materials*, vol. 5, no. 3, pp. 240–247, 2002.
- [14] L. A. Stephen, A. J. Dwayne, and A. M. Matthew, "Predicting the service life of concrete marine structures: an environmental methodology," *Structural Journal*, vol. 95, no. 1, pp. 27–36, 1998.
- [15] Y. P. Liu and R. E. Weyers, "Modeling the time-to-corrosion cracking in chloride contaminated reinforced concrete structures," *ACI Materials Journal*, vol. 95, no. 6, pp. 675–682, 1998.
- [16] C. Q. Li, "Reliability based service life prediction of corrosion affected concrete structures," *Journal of Structural Engineering*, vol. 130, no. 10, pp. 1570–1577, 2004.
- [17] R. François and G. Arliguie, "Effect of microcracking and cracking on the development of corrosion in reinforced concrete members," *Magazine of Concrete Research*, vol. 51, no. 2, pp. 143–150, 1999.
- [18] T. Vidal, A. Castel, and R. François, "Analyzing crack width to predict corrosion in reinforced concrete," *Cement and Concrete Research*, vol. 34, no. 1, pp. 165–174, 2004.
- [19] C. Arya and L. A. Wood, "The relevance of cracking in concrete to corrosion in reinforcement," Technical Report no. 44, The Concrete Society, Berkshire, UK, 1995.
- [20] C. Alonso, C. Andrade, J. Rodriguez, and J. M. Diez, "Factors controlling cracking of concrete affected by reinforcement corrosion," *Materials and Structures*, vol. 31, no. 211, pp. 435–441, 1998.
- [21] M. A. Peter, A. Muntean, S. A. Meier, and M. Böhm, "Competition of several carbonation reactions in concrete: a parametric study," *Cement and Concrete Research*, vol. 38, no. 12, pp. 1385–1393, 2008.
- [22] V. G. Papadakis, C. G. Vayenas, and M. N. Fardis, "Fundamental modeling and experimental investigation of concrete carbonation," *ACI Materials Journal*, vol. 88, no. 4, pp. 363–373, 1991.
- [23] V. Baroghel-Bouny, *Concrete Design for a Given Structure Service Life: Durability Management with Regard to Reinforcement Corrosion and Alkali-silica Reaction*, AFGC, Paris, France, 2007.
- [24] A. V. Saetta and R. V. Vitaliani, "Experimental investigation and numerical modeling of carbonation process in reinforced concrete structures. Part I. Theoretical formulation," *Cement and Concrete Research*, vol. 34, no. 4, pp. 571–579, 2004.
- [25] O. B. Isgor and A. G. Razaqpur, "Finite element modeling of coupled heat transfer, moisture transport and carbonation processes in concrete structures," *Cement and Concrete Composites*, vol. 26, no. 1, pp. 57–73, 2004.
- [26] H.-W. Song, S.-J. Kwon, K.-J. Byun, and C.-K. Park, "Predicting carbonation in early-aged cracked concrete," *Cement and Concrete Research*, vol. 36, no. 5, pp. 979–989, 2006.
- [27] S. Alahmad, A. Toumi, J. Verdier, and R. François, "Effect of crack opening on carbon dioxide penetration in cracked mortar samples," *Materials and Structures*, vol. 42, no. 5, pp. 559–566, 2009.
- [28] D. T. Niu, *Durability and Life Forecast of Reinforced Concrete Structure*, Science Press, Beijing, China, 1st edition, 2003.
- [29] F. H. Wittmann, P. Zhang, and T. G. Zhao, "Influence of combined environmental loads on durability of reinforced concrete structures," *Restoration of Buildings and Monuments*, vol. 12, no. 4, pp. 349–361, 2006.
- [30] C. Xu, C.-K. Wang, and W.-L. Jin, "Interaction effect of chloride attack and carbonization in concrete," *Journal of Building Materials*, vol. 14, no. 3, pp. 376–380, 2011.
- [31] E. Beaudoin, "Carbonation and chloride penetration in concrete-with special objective of service life modelling by the factor approach," Tech. Rep. VTT-R-04771-09, VTT Technical Research Centre of Finland, 2008.
- [32] X. N. Peng, *Study on Several Fatigue Durability Problems of Reinforced Concrete with Bars Corroded*, Guangxi University, Nanning, China, 2004.

Research Article

Damage Identification of Urban Overpass Based on Hybrid Neurogenetic Algorithm Using Static and Dynamic Properties

Hanbing Liu, Xianqiang Wang, Yafeng Gong, and Yubo Jiao

College of Transportation, Jilin University, Changchun 130025, China

Correspondence should be addressed to Yubo Jiao; jiaoyb@jlu.edu.cn

Received 10 March 2015; Revised 12 May 2015; Accepted 18 May 2015

Academic Editor: Anaxagoras Elenas

Copyright © 2015 Hanbing Liu et al. This is an open access article distributed under the Creative Commons Attribution License, which permits unrestricted use, distribution, and reproduction in any medium, provided the original work is properly cited.

Urban overpass is an important component of transportation system. Health condition of overpass is essential to guarantee the safe operation of urban traffic. Therefore, damage identification of urban overpass possesses important practical significance. In this paper, finite element model of left auxiliary bridge of Qianjin Overpass is constructed and vulnerable sections of structure are chosen as objects for damage recognition. Considering the asymmetry of Qianjin bridge, change rate of modal frequency and strain ratio are selected as input parameters for hybrid neurogenetic algorithm, respectively. Identification effects of damage location and severity are investigated and discussed. The results reveal that the proposed method can successfully identify locations and severities with single and multiple damage locations; its interpolation ability is better than extrapolation ability. Comparative analysis with BP neural network is conducted and reveals that the damage identification accuracy of hybrid neurogenetic algorithm is superior to BP. The effectiveness between dynamic and static properties as input variable is also analyzed. It indicates that the identification effect of strain ratios is more satisfactory than frequency ratio.

1. Introduction

Bridge structures are exposed to various external environments including vehicle, wind, and temperature. The security and durability of many bridges decline and damage appears, which will lead to unexpected collapse. Therefore, damage identification for these bridges has important practical significance [1–3].

Traditional nondestructive evaluation- (NDE-) based methods such as ultrasonic and X-ray techniques have been widely applied for damage detection. However, the NDE-based damage detection approaches face the criticism that users have to know the damage vicinity in advance and damage prone areas have to be readily accessible in bridge monitoring [4]. To overcome the shortcomings of these local damage detection methods, overall identification method based on modal properties was put forward. Its theoretical background is that damage will modify the stiffness and mass of structure and then alter the modal data. Conversely, modal parameters can be regarded as damage indicators of structure. Most widely used modal parameters for damage

identification include modal frequency, modal flexibility, modal strain energy, and modal curvature [5–8].

Frequency is the most easily obtained modal parameter [9–12]. With improvement of signal processing and analyzing, the identification precision of frequency becomes more favorable. Cawley and Adams proposed a nondestructive method to assess the integrity of structures using measurements of structural natural frequencies. The results have shown that it could detect, locate, and quantify damage [13]. Guo and Yi built the functional relationship between structural damage and change rate of frequency based on modal perturbation theory and successfully realized the damage identification of location and level [14]. Patil and Maiti put forward a multicrack damage identification method based on modal frequency for slender Bernoulli-Euler beams [15]. Kim and Stubbs presented a method to locate and estimate size of crack by using natural frequency changes; numerical simulation verified its feasibility [16].

In recent years, Artificial Neural Networks- (ANNs-) based damage identification methods have been widely utilized because of their excellent pattern recognition capacity

[17–19]. Kao and Hung [20] presented a novel neural network-based approach for detecting structural damage by using two-step method. Fang et al. [21] proposed a back-propagation (BP) neural network-based damage identification method using frequency response functions as input data. Numerical simulation demonstrated that neural network can assess damage conditions with favorable accuracy. Mehrjoo et al. [22] presented a method for estimating the damage intensities of joints for truss bridge structures using a BP neural network. Bakhary et al. [23] developed a statistical approach to take into account the effect of uncertainties in developing ANNs model. However, ANNs have several drawbacks. Their convergence rate is very low and the chances of getting stuck in local minima are relatively high [17]. Complementarily, genetic algorithm (GA) is able to find global optimal solution on a complicated optimization problem. Therefore, hybrid neurogenetic algorithm is promising choice for damage identification of bridge.

This paper is aimed at damage assessment of urban overpass, whose structural characteristics and mechanical properties are more complicated than traditional bridges. Taking advantages of calculation features of ANNs and GA, the initial weights and thresholds of BP neural networks are optimized by GA. The change rate of frequency and nodal strain before and after damage are chosen as input parameters, respectively. Comparative analysis is conducted to verify the superiority between BP and neurogenetic algorithm and also between dynamic property and static property.

2. Theoretical Background

2.1. Basic Theory of ANNs. ANNs are information processing systems which mimic the network structure of actual human brain [24]. It can process complex logic operations and achieve nonlinear mapping adaptively through learning. The process contains the forward propagation and back propagation. BP neural network is a widely used back-propagation network and consists of an input layer, hidden layers, and an output layer. The typical three-layer neural network is shown in Figure 1, in which successive layers are connected by adaptive interconnected weights. Training process of neural network is to minimize the objective function through adjusting the interconnected weights. The objective function is generally taken as the sum-squared error function [17], as shown in

$$E = \sum_{k=1}^P \sum_{m=1}^n (O_{km} - T_{km})^2, \quad (1)$$

where O_{km} and T_{km} are the actual and target output of m th neuron in output layer for k th training pattern, respectively. n is the number of outputs and p is the number of patterns. The calculation process of actual output in neural network with three layers is shown in Figure 2.

The design of suitable network is based on the selection of the number of hidden layers, number of neurons in the hidden layers, and the training algorithm. This paper adopts the BP neural network with one hidden layer, shown in Figure 1, as basic network architecture. The suitable number

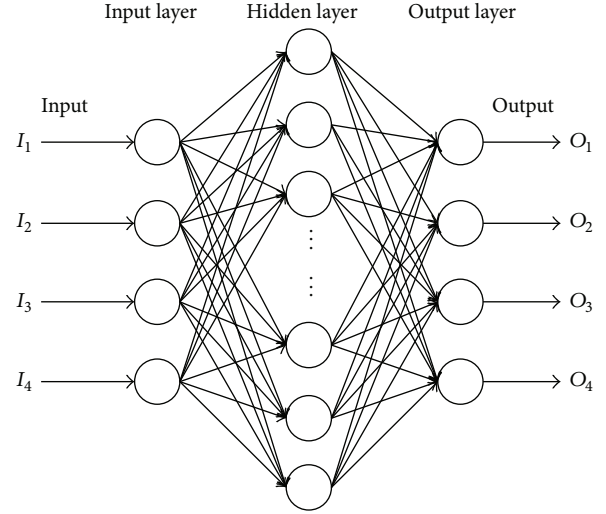


FIGURE 1: Architecture of three-layer BP neural network.

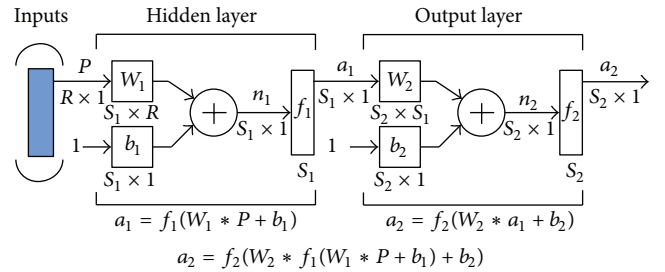


FIGURE 2: Calculation process of neural network.

of neurons in hidden layer is determined by multiple trial and errors in the standard neural network procedure. Considering the performance in minimizing mean square error (MSE) and accelerating convergence, neural networks with 10-13-4 topology (10 input layer neurons, 13 hidden layer neurons, and 4 output layer neurons) and 20-25-4 topology (20 input layer neurons, 25 hidden layer neurons, and 4 output layer neurons) are utilized to identify damage based on frequency and strain, respectively. In addition, the activation functions on hidden and output layers are sigmoid and linear function, respectively, while training algorithm adopts the Levenberg-Marquardt (L-M) algorithm.

2.2. Basic Theory of GA. Genetic algorithm is adaptive probabilistic search algorithm for global optimization [25]. It is derived from the biological natural selection and genetic mechanisms. It is especially suitable for dealing with the complex and nonlinear problems which traditional search methods cannot resolve. Comparing with conventional optimization methods, the most highlighted advantage of GA is being not easy to trap in local optima due to many individuals (population) exploring in their search space [26].

In the optimization process of GA, the basic purpose is to maximize the fitness function by employing the three genetic operators called selection, crossover, and mutation. Firstly,

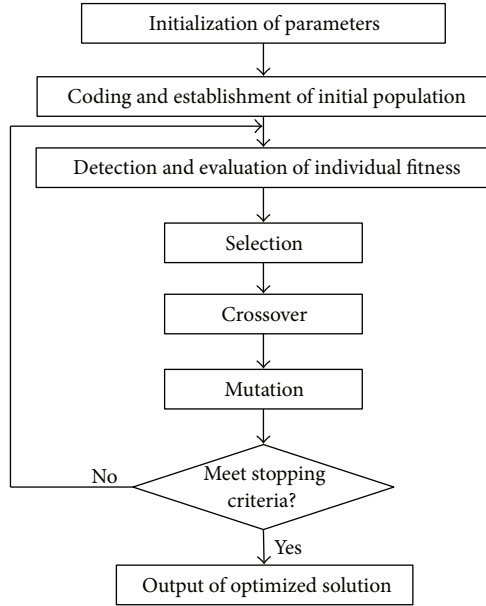


FIGURE 3: Processing flow of GA.

a population of individuals is initially generated at random and their fitness values are evaluated. Then, the selection operator selects a better set of individuals with higher fitness values in order to generate the next generation by the next two operators: crossover and mutation. In the crossover operator, two parents are selected randomly to breed two new offspring by exchanging different segments of the parents with each other. The mutation operator selects a random genome of a particular solution and alters its value to create new individual. Finally, with the evaluation of fitness for the new generation, the selection operator is utilized to select better parents for next generation. The above procedures are repeated for few generations until a given terminal criterion is satisfied. The basic calculation flow is shown in Figure 3.

The performance of GA is closely associated with coding, initial population, fitness function, genetic operation, and terminal condition. They are introduced in detail in the following.

(1) *Coding*. In GA, the individual in population is coded as a string of chromosome of given length l , and each string of chromosome represents a feasible solution to the optimization problem [27]. Because of the easy implementation to crossover and mutation operation, the binary code is usually used in GA. However, binary code makes the string of chromosome too long and fails to obtain high learning precision. It is incapable of coding parameter composed of the weights and thresholds of BP neural network. The real code is adopted in this paper to code the string of chromosome representing the weights and thresholds. Each position in chromosome denotes a weight or threshold of BP neural network.

(2) *Initial Population*. The production of GA begins with the initial population. Suppose that the population size is N .

The individuals in initial population are assigned values to their chromosomes randomly. The fitness of population is evaluated to guide the genetic operation. Each generation possesses the same size with initial population. The low number of the chromosomes will lead to searching a small part of the search space. According to the researches, a suitable population with 20–100 chromosomes can get best answers [28].

(3) *Fitness Function*. Each individual corresponds to different initial weights and thresholds of BP neural network. The fitness values of individuals represent the difference between actual outputs and expected outputs of BP neural network. The individual with bigger fitness is considered to have a better chance of survival. Fitness function is defined as follows:

$$F = \frac{1}{1 + E}, \quad (2)$$

where E is the sum-squared error of BP neural network.

(4) *Genetic Operation*

(a) *Selection*. Roulette wheel selection is a selection operator based on the fitness of individuals. The selection probability of each individual as next generation is in proportion to its fitness. This probability of the i th individual in population is calculated as follows:

$$P_i = \frac{F_i}{\sum_{j=1}^N F_j}, \quad (3)$$

where F_i is the fitness of i th individual in population and N is the population size. According to the Darwinian theory of survival of the fittest, it is more possible for the individual with better fitness in the current population to be selected and duplicated into the next generation.

(b) *Crossover*. Crossover operation creates offspring through the intersection of two parent chromosomes. The arithmetic crossover operator is adopted to perform crossover between two parent chromosomes coded as real variables. Suppose that two parent chromosome vectors are $N_1 = (x_1^{(1)}, x_2^{(1)}, \dots, x_m^{(1)})$ and $N_2 = (x_1^{(2)}, x_2^{(2)}, \dots, x_m^{(2)})$ and two offspring are $N_a = (x_1^{(a)}, x_2^{(a)}, \dots, x_m^{(a)})$ and $N_b = (x_1^{(b)}, x_2^{(b)}, \dots, x_m^{(b)})$, respectively. $(\alpha_1, \alpha_2, \dots, \alpha_m)$ are the random numerical values between 0 and 1. The calculation process of nonuniform arithmetic crossover is defined as follows:

$$\begin{aligned} x_i^{(a)} &= \alpha_i x_i^{(1)} + (1 - \alpha_i) x_i^{(2)} = x_i^{(2)} + \alpha_i (x_i^{(1)} - x_i^{(2)}), \\ x_i^{(b)} &= \alpha_i x_i^{(2)} + (1 - \alpha_i) x_i^{(1)} = x_i^{(1)} + \alpha_i (x_i^{(2)} - x_i^{(1)}), \end{aligned} \quad (4)$$

where $i = 1, 2, \dots, m$ and m is the number of real variables in individual chromosome.

(c) *Mutation*. The nonuniform mutation operator is used to perform mutation in chromosomes. Suppose that parent chromosome $A = (x_1, x_2, \dots, x_k, \dots, x_m)$ produces mutation randomly at k th variable and the variation range

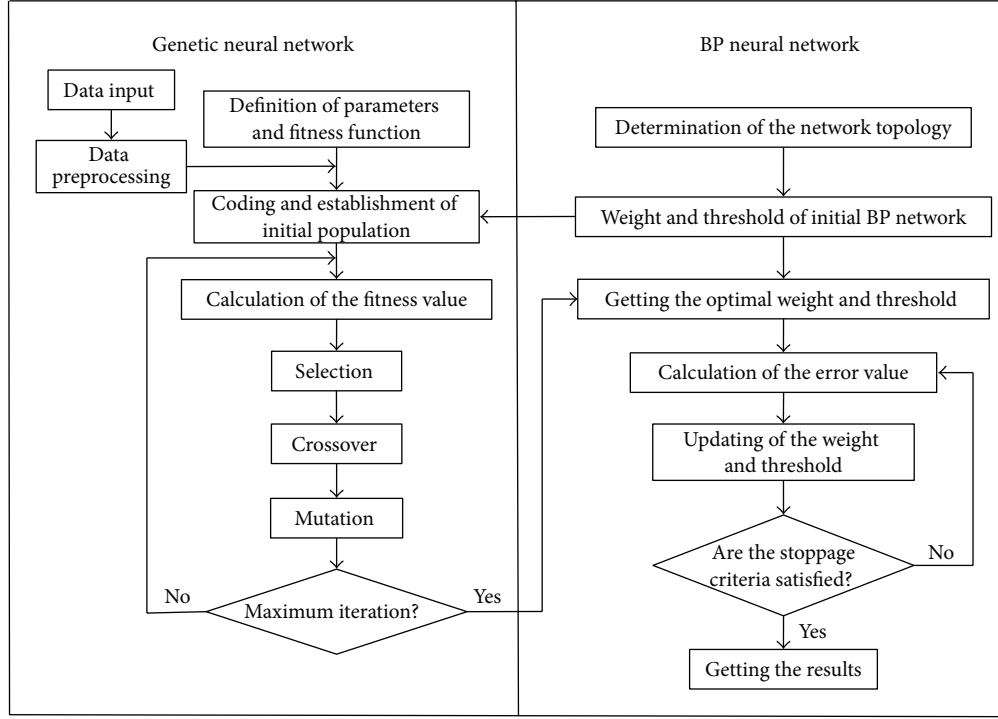


FIGURE 4: Calculation process of hybrid neurogenetic algorithm.

is (a_k, b_k) . The new offspring after mutation is $A' = (x_1, x_2, \dots, x'_k, \dots, x_m)$. x'_k is calculated according to

$$x'_k = \begin{cases} x_k + \Delta(t, b_k - x_k), & \text{rnd} \leq 0.5, \\ x_k - \Delta(t, x_k - a_k), & \text{rnd} > 0.5. \end{cases} \quad (5)$$

Δ is defined as

$$\Delta(t, y) = y \cdot r \cdot \left(1 - \frac{t}{T}\right)^\lambda, \quad (6)$$

where rnd and r are the random numbers between 0 and 1; t and T are the current iteration time and the maximum number of iterations, respectively; λ is a constant between 2 and 5, which controls the dependency of algorithm on iteration times.

(5) *Terminal Condition.* The optimization process of GA stops when the fitness of optimal individual satisfies the given critical value or the evolution reaches the maximum iteration. Generally, the maximum number of iterations is set between 100 and 500. In this paper, the maximum number of iterations is adopted as stoppage criteria.

2.3. Basic Theory of Hybrid Neurogenetic Algorithm. The prediction performance of BP neural network highly depends on the initial weights and thresholds of BP model. In this paper, the initial weights and thresholds are optimized by genetic algorithm. The combination of neural network and genetic algorithm can effectively overcome the shortcomings of neural network in order to realize the identification of

damage location and severity for urban overpasses. The method of hybrid neurogenetic algorithm includes three steps: the determination of network structure, the optimization of genetic algorithm, and output prediction of BP neural network. Its basic process is shown in Figure 4.

The architectures of BP neural networks used to identify damage based on frequency and strain are determined as 10-13-4 and 20-25-4, respectively. In order to avoid overfitting in neural network, the hidden layer neurons are defined based on the available data and multiple trials. Initial weights and thresholds are selected and coded as real variables in chromosomes. The optimization of GA is carried out with a population of 50 and the maximum number of iterations of 100. After the optimization for the initial weights and thresholds, BP neural network is trained with the setting parameters. The maximum number of iterations is 2000, tolerance error is $1.0e-13$, and learning coefficients are set as 0.3. In addition, a good preprocessing plays an important role in robustness and reliability of the networks. Therefore, the normalization for the input data is carried out before using any databases. Hybrid neurogenetic algorithm makes the BP neural network more practical and accurate to identify damage in structure.

3. Numerical Simulation

3.1. Model Overview. Left auxiliary bridge of Qianjin Overpass in Changchun is a four-span continuous prestressed concrete box girder bridge. Each span has the length of 23 m, and the height of girder is 1.3 m. Schematic diagram for structure plan is shown in Figure 5.

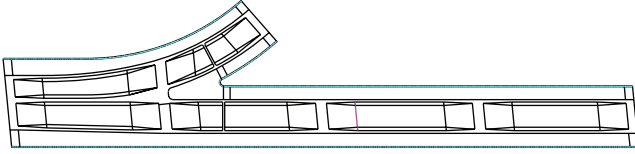


FIGURE 5: Structural plan.

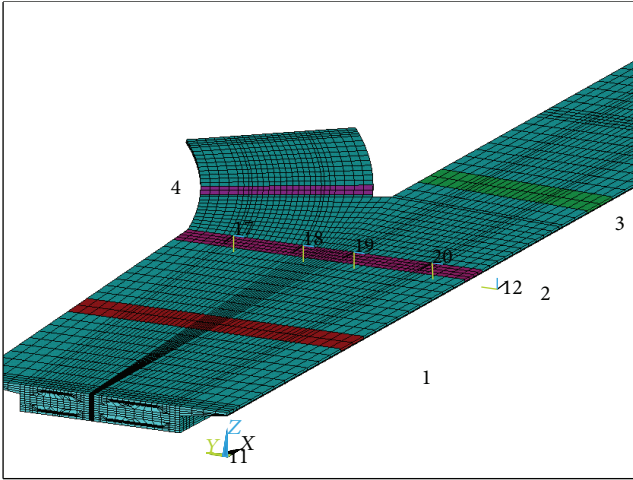


FIGURE 6: Determination of damaged sections.

3.2. Determination of Damage Sections. In consideration of the complexity of calculation model, it is unpractical to identify all elements of the structure, so vulnerable areas are chosen as objects for study in order to improve the computing efficiency. Bifurcation portion of bridge bears complicated bending-torsion coupling effect and becomes the emphasis area to identify damage. Therefore, research objects of this model include the middle section of the first span (section 1), the fulcrum section of the first span (section 2), and the middle section of the second span (section 3 and section 4). They are shown in Figure 6. The element damage is simulated through the reduction of elastic modulus and the percentage of reduction represents the damage extent.

3.3. Determination of Parameters for Damage Identification

(1) Input Parameters. Change rates of frequencies and nodal strains at characteristic sections are chosen as input parameters for hybrid neurogenetic algorithm. The dynamic input parameter can be calculated by

$$FCR_i = \frac{f_{ui} - f_{di}}{f_{ui}}, \quad (7)$$

where FCR_i is the i th-order frequency ratio and f_{ui} and f_{di} represent i th-order frequency of the model before and after damage, respectively.

The static input parameter can be expressed by

$$SCR_j = \left| \frac{S_{uj} - S_{dj}}{S_{uj}} \right|, \quad (8)$$

where SCR_j is the strain ratio at node j and S_{uj} and S_{dj} represent measured data of strains at node j before and after damage, respectively.

Totally 20 nodes are selected as characteristic nodes, and strain ratios at these nodes are treated as input variables of hybrid neurogenetic algorithm. The characteristic nodes locate at the first mid-span, second mid-span, third mid-span, and fourth mid-span and also related fulcrum sections.

(2) Output Parameter. Damage levels of elements are simulated by the decline of element rigidity, defined as follows:

$$\alpha_i = 1 - \frac{k_{i,d}}{k_{i,u}}, \quad (9)$$

where i is the number of element, α_i is the damage level, $k_{i,d}$ is the element rigidity with damage, and $k_{i,u}$ is the element rigidity without damage.

The output parameter of hybrid neurogenetic algorithm is defined as follows:

$$\text{output} = \{o_1, o_2, \dots, o_n\}^T. \quad (10)$$

For identification of damage location, $o_i = 1$ represents that section i has damage and $o_i = 0$ represents that section i is undamaged.

For identification of damage severity, o_i represents damage level of section i (α_i).

3.4. Damage Identification Based on Change Rate of Frequency and Hybrid Neurogenetic Algorithm

(1) Damage Identification with Single Damage Location. Taking damage identification of sections 1, 2, 3, and 4, for example, the levels of damage are considered in the range between 10% and 50%, or six damage levels of 10%, 20%, 30%, 35%, 40%, and 50%. 16 training samples are chosen with damage levels of 10%, 20%, 30%, and 40%, while 8 test samples with damage levels of 35% and 50% are used to check the damage identification performance. Testing cases are listed in Table 1.

Results of damage location identification are shown in Table 2. It indicates that hybrid neurogenetic algorithm can successfully identify the location of damage, and it has favorable generalization ability.

As for damage severity identification, the damage identification results are shown in Table 3, and the corresponding error curve and fitness curve are shown in Figures 7 and 8.

As can be seen from Table 3, the maximum error for testing samples with damage level 35% is 3.1%, while it is 4.66% for damage level 50%. It indicates that hybrid neurogenetic algorithm has better interpolation ability and relatively weaker extrapolation ability.

(2) Damage Identification with Multiple Damage Locations. Damage cases with multiple damage locations are listed in Table 4. For example, the case with damage levels of 20%-20% in damage sections 1 and 3 represents that the damage severity

TABLE 1: Testing cases for damage identification with single damage location.

| Testing case | Damage section (corresponding expected output) | Damage severity (corresponding expected output) |
|--------------|--|---|
| S1 | 1 (1-0-0-0) | 35% (0.35-0-0-0) |
| S2 | 1 (1-0-0-0) | 50% (0.5-0-0-0) |
| S3 | 2 (0-1-0-0) | 35% (0-0.35-0-0) |
| S4 | 2 (0-1-0-0) | 50% (0-0.5-0-0) |
| S5 | 3 (0-0-1-0) | 35% (0-0-0.35-0) |
| S6 | 3 (0-0-1-0) | 50% (0-0-0.5-0) |
| S7 | 4 (0-0-0-1) | 35% (0-0-0-0.35) |
| S8 | 4 (0-0-0-1) | 50% (0-0-0-0.5) |

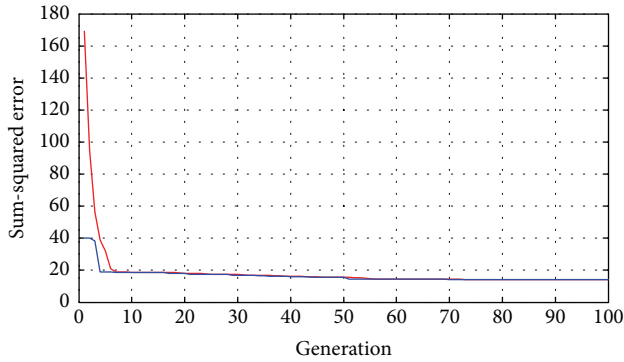


FIGURE 7: Error curve of damage severity identification with single damage location.

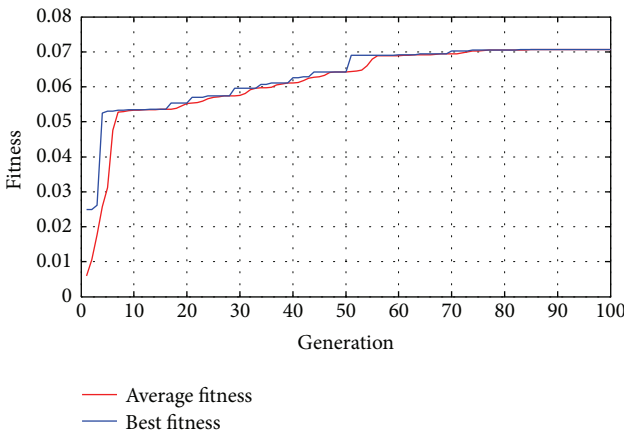


FIGURE 8: Fitness curve of damage severity identification with single damage location.

of section 1 is 20% and that of section 3 is also 20%. Eight samples with damage levels of 20%-30%, 30%-35%, 35%-35%, and 40%-20% of sections 1 and 3 and 20%-30%, 30%-35%, 35%-35%, and 40%-20% of sections 2 and 4 are selected as testing cases, as shown in Table 5, while the others are training samples.

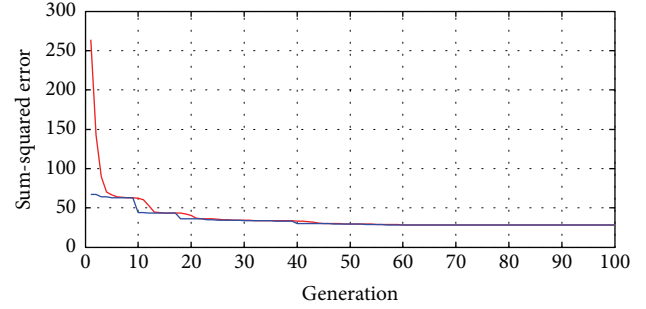


FIGURE 9: Error curve of damage severity identification with multiple damage locations.

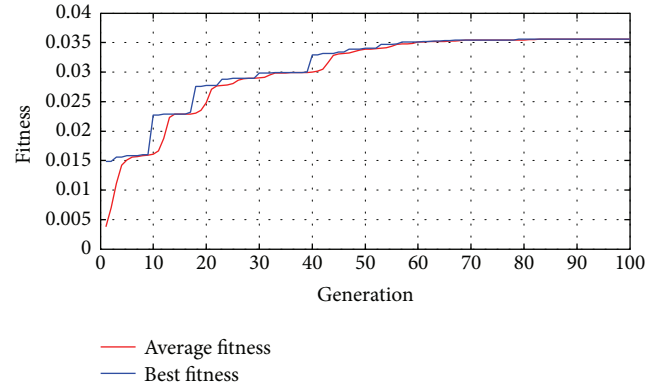


FIGURE 10: Fitness curve of damage severity identification with multiple damage locations.

Results of damage locations identification are listed in Table 6. The results reveal that damage localization of hybrid neurogenetic algorithm with multi-damage locations is favorable.

The damage severity identification results with multiple locations are shown in Table 7, and the corresponding error curve and fitness curve are shown in Figures 9 and 10.

As can be seen from Table 7, hybrid neurogenetic algorithm can successfully identify the damage levels for multiple damage locations with favorable accuracy. The maximum relative error is 5%.

3.5. Damage Identification Based on Strain Ratio and Hybrid Neurogenetic Algorithm

(1) *Damage Identification with Single Damage Location.* Training and test samples are the same with damage identification using frequency ratio. Results of damage location identification are listed in Table 8. The results reveal that damage localization results are favorable.

The damage severity identification results are shown in Table 9. As can be seen from Table 9, the maximum error for samples with damage level 35% is 2.29%, while it is 2.5% for damage level 50%. It also indicates that hybrid neurogenetic algorithm has better interpolation ability and relatively weaker extrapolation ability.

TABLE 2: Damage localization with single damage using frequency ratio.

| Output results | Testing cases | | | | | | | |
|------------------|---------------|--------|--------|--------|--------|--------|--------|--------|
| | S1 | S2 | S3 | S4 | S5 | S6 | S7 | S8 |
| Expected outputs | 1 | 1 | 0 | 0 | 0 | 0 | 0 | 0 |
| | 0 | 0 | 1 | 1 | 0 | 0 | 0 | 0 |
| | 0 | 0 | 0 | 0 | 1 | 1 | 0 | 0 |
| | 0 | 0 | 0 | 0 | 0 | 0 | 1 | 1 |
| Actual outputs | 1.004 | 1.003 | 0.000 | -0.004 | 0.000 | -0.003 | -0.001 | -0.001 |
| | -0.004 | -0.003 | 1.000 | 1.005 | 0.000 | 0.003 | 0.001 | 0.001 |
| | -0.001 | 0.001 | -0.001 | -0.003 | 1.001 | 1.001 | -0.001 | 0.002 |
| | 0.001 | 0.000 | 0.000 | 0.002 | -0.001 | -0.001 | 1.000 | 0.998 |

TABLE 3: Damage severity identification with single damage location using frequency ratio.

| Output results | Testing cases | | | | | | | |
|---------------------|---------------|--------|---------|---------|---------|--------|---------|---------|
| | S1 | S2 | S3 | S4 | S5 | S6 | S7 | S8 |
| Expected outputs | 0.35 | 0.5 | 0 | 0 | 0 | 0 | 0 | 0 |
| | 0 | 0 | 0.35 | 0.5 | 0 | 0 | 0 | 0 |
| | 0 | 0 | 0 | 0 | 0.35 | 0.5 | 0 | 0 |
| | 0 | 0 | 0 | 0 | 0 | 0 | 0.35 | 0.5 |
| Actual outputs | 0.3453 | 0.5268 | 0.0002 | 0.0078 | 0.0014 | 0.0047 | -0.0016 | 0.0078 |
| | 0.0034 | 0.0085 | 0.3503 | 0.5034 | -0.0024 | 0.0020 | -0.0002 | -0.0096 |
| | -0.0047 | 0.0038 | -0.0015 | -0.0016 | 0.3391 | 0.5190 | -0.0007 | -0.0036 |
| | -0.0050 | 0.0039 | 0.0048 | -0.0092 | 0.0024 | 0.0013 | 0.3541 | 0.5218 |
| Relative errors (%) | 1.34 | 4.66 | 0.08 | 0.68 | 3.1 | 3.8 | 1.17 | 4.36 |

TABLE 4: Cases for damage identification with multiple locations.

| Damage section | Damage severity |
|------------------|--|
| Sections 1 and 3 | 20%-20%; 20%-30%; 20%-35%; 20%-40%; 30%-20%; 30%-30%; 30%-35%; 30%-40%; 35%-20%; 35%-30%; 35%-35%; 35%-40%; 40%-20%; 40%-30%; 40%-35%; 40%-40%; |
| Sections 2 and 4 | 20%-20%; 20%-30%; 20%-35%; 20%-40%; 30%-20%; 30%-30%; 30%-35%; 30%-40%; 35%-20%; 35%-30%; 35%-35%; 35%-40%; 40%-20%; 40%-30%; 40%-35%; 40%-40%; |

Note: case with damage levels of A%-B% in damage sections C1 and C2 represents that the damage severity of section C1 is A% and that of section C2 is B%.

TABLE 5: Testing cases for damage identification with multiple damage location.

| Testing case | Damage section (corresponding expected output) | Damage severity (corresponding expected output) |
|--------------|--|---|
| M1 | 1 and 3 (1-0-1-0) | 20%-30% (0.2-0-0.3-0) |
| M2 | 1 and 3 (1-0-1-0) | 30%-35% (0.3-0-0.35-0) |
| M3 | 1 and 3 (1-0-1-0) | 35%-35% (0.35-0-0.35-0) |
| M4 | 1 and 3 (1-0-1-0) | 40%-20% (0.4-0-0.2-0) |
| M5 | 2 and 4 (0-1-0-1) | 20%-30% (0-0.2-0-0.3) |
| M6 | 2 and 4 (0-1-0-1) | 30%-35% (0-0.3-0-0.35) |
| M7 | 2 and 4 (0-1-0-1) | 35%-35% (0-0.35-0-0.35) |
| M8 | 2 and 4 (0-1-0-1) | 40%-20% (0-0.4-0-0.2) |

TABLE 6: Damage localization of multi-damage locations using frequency ratio.

| Output results | Testing cases | | | | | | | |
|------------------|---------------|-------|------|-------|------|------|------|------|
| | M1 | M2 | M3 | M4 | M5 | M6 | M7 | M8 |
| Expected outputs | 1 | 1 | 1 | 1 | 0 | 0 | 0 | 0 |
| | 0 | 0 | 0 | 0 | 1 | 1 | 1 | 1 |
| | 1 | 1 | 1 | 1 | 0 | 0 | 0 | 0 |
| | 0 | 0 | 0 | 0 | 1 | 1 | 1 | 1 |
| Actual outputs | 1.01 | 1.01 | 0.99 | 1.01 | 0.01 | 0.00 | 0.00 | 0.00 |
| | -0.02 | -0.01 | 0.01 | -0.01 | 0.99 | 1.00 | 1.00 | 1.00 |
| | 1.01 | 1.01 | 1.00 | 1.01 | 0.01 | 0.00 | 0.00 | 0.00 |
| | -0.01 | -0.01 | 0.00 | -0.01 | 0.99 | 1.00 | 1.00 | 1.00 |

TABLE 7: Damage severity identification with multiple damage locations using frequency ratio.

| Output results | Testing cases | | | | | | | |
|---------------------|---------------|-------|------|-------|------|------|------|------|
| | M1 | M2 | M3 | M4 | M5 | M6 | M7 | M8 |
| Expected outputs | 0.2 | 0.3 | 0.35 | 0.4 | 0 | 0 | 0 | 0 |
| | 0 | 0 | 0 | 0 | 0.2 | 0.3 | 0.35 | 0.4 |
| | 0.3 | 0.35 | 0.35 | 0.2 | 0 | 0 | 0 | 0 |
| | 0 | 0 | 0 | 0 | 0.3 | 0.35 | 0.35 | 0.2 |
| Actual outputs | 0.21 | 0.31 | 0.34 | 0.41 | 0.00 | 0.00 | 0.00 | 0.00 |
| | 0.00 | -0.01 | 0.01 | -0.02 | 0.20 | 0.30 | 0.35 | 0.40 |
| | 0.30 | 0.35 | 0.34 | 0.21 | 0.00 | 0.00 | 0.00 | 0.00 |
| | 0.02 | 0.01 | 0.00 | 0.00 | 0.31 | 0.35 | 0.35 | 0.20 |
| Relative errors (%) | 5.00 | 3.33 | 2.85 | 2.50 | 0 | 0 | 0 | 0 |
| | 0 | 0 | 2.85 | 5.00 | 3.33 | 0 | 0 | 0 |

TABLE 8: Damage location identification with single damage using strain ratio.

| Output results | Testing cases | | | | | | | |
|------------------|---------------|--------|---------|---------|--------|---------|---------|---------|
| | S1 | S2 | S3 | S4 | S5 | S6 | S7 | S8 |
| | 1 | 1 | 0 | 0 | 0 | 0 | 0 | 0 |
| Expected outputs | 0 | 0 | 1 | 1 | 0 | 0 | 0 | 0 |
| | 0 | 0 | 0 | 0 | 1 | 1 | 0 | 0 |
| | 0 | 0 | 0 | 0 | 0 | 0 | 1 | 1 |
| | 0 | 0 | 0 | 0 | 0 | 0 | 0 | 0 |
| Actual outputs | 1.0000 | 0.9999 | 0.0001 | -0.0002 | 0.0002 | 0.0009 | 0.0000 | 0.0000 |
| | 0.0000 | 0.0000 | 1.0000 | 0.9999 | 0.0002 | -0.0005 | -0.0001 | -0.0001 |
| | 0.0000 | 0.0000 | 0.0000 | -0.0001 | 1.0001 | 0.9997 | 0.0000 | 0.0000 |
| | 0.0000 | 0.0000 | -0.0001 | 0.0001 | 0.0000 | -0.0003 | 1.0000 | 0.9998 |

TABLE 9: Damage severity identification with single damage location using strain ratio.

| Output results | Testing cases | | | | | | | |
|---------------------|---------------|---------|---------|---------|---------|---------|---------|---------|
| | S1 | S2 | S3 | S4 | S5 | S6 | S7 | S8 |
| | 0.35 | 0.5 | 0 | 0 | 0 | 0 | 0 | 0 |
| Expected outputs | 0 | 0 | 0.35 | 0.5 | 0 | 0 | 0 | 0 |
| | 0 | 0 | 0 | 0 | 0.35 | 0.5 | 0 | 0 |
| | 0 | 0 | 0 | 0 | 0 | 0 | 0.35 | 0.5 |
| | 0 | 0 | 0 | 0 | 0 | 0 | 0 | 0 |
| Actual outputs | 0.342 | 0.5125 | -0.0006 | 0.0036 | -0.0004 | 0.0083 | 0.0032 | 0.0028 |
| | 0.0005 | 0.0007 | 0.3526 | 0.5011 | 0.0001 | 0 | -0.0008 | -0.0012 |
| | 0.0000 | -0.0001 | -0.0001 | -0.0002 | 0.3512 | 0.5023 | 0.0001 | 0.0002 |
| | 0.0022 | 0.0036 | 0.0007 | -0.0034 | 0 | -0.0019 | 0.3468 | 0.5081 |
| Relative errors (%) | 2.29 | 2.5 | | | | | | |
| | | | 0.74 | 0.22 | | 0.33 | 0.47 | |
| | | | | | | | 0.9 | 1.6 |

(2) *Damage Identification with Multiple Damage Locations.* Results of damage locations identification are listed in Table 10. The results reveal that damage localization of hybrid neurogenetic algorithm with multi-damage locations is favorable.

The damage severity identification results with multiple locations are shown in Table 11.

As can be seen from Table 11, hybrid neurogenetic algorithm can successfully identify the damage levels of multi-damage cases with favorable accuracy. The maximum relative error is 2.42%.

4. Comparative Analysis

In order to verify the effectiveness of the proposed method in this paper, comparative analysis between hybrid neurogenetic algorithm and BP network is conducted.

Taking the damage identification of sections 1 and 3 using frequency ratio as input variable, for example, damage cases are shown in Table 12. Two samples with damage degrees of 20%-35% and 30%-40% are selected as testing cases, while the others are training samples. Corresponding damage identification results are listed in Table 13.

As can be seen from Table 13, the maximal relative error of hybrid neurogenetic algorithm and BP is 5% and 8.57%,

respectively. It reveals that the damage identification accuracy of hybrid neurogenetic algorithm is superior to BP.

As for the effect using static and dynamic properties as input variables, comparison between Tables 7 and 11 presents that the identification effect of strain ratios is more satisfactory than frequency ratio.

5. Conclusions

A hybrid neurogenetic algorithm-based method is proposed for damage identification of urban overpass. Change rate of frequency and strain ratio are treated as input parameters, respectively. The optimized weight and threshold are treated as the initial value of ANNs to identify the damage of bridge structure. Damage identification with single and multiple locations is used to verify the feasibility of the proposed method.

For both input parameters, numerical simulation results reveal that hybrid neurogenetic algorithm possesses favorable ability to identify the location of damage both for single damage case and multi-damage cases. For damage severity identification, the interpolation ability is better than extrapolation ability.

Comparative analysis with BP neural network indicates that maximal error of hybrid neurogenetic algorithm and BP

TABLE 10: Damage location identification of multi-damage locations using strain ratio.

| Output results | Testing cases | | | | | | | |
|------------------|---------------|---------|---------|--------|--------|--------|--------|---------|
| | M1 | M2 | M3 | M4 | M5 | M6 | M7 | M8 |
| Expected outputs | 1 | 1 | 1 | 1 | 0 | 0 | 0 | 0 |
| | 0 | 0 | 0 | 0 | 1 | 1 | 1 | 1 |
| | 1 | 1 | 1 | 1 | 0 | 0 | 0 | 0 |
| | 0 | 0 | 0 | 0 | 1 | 1 | 1 | 1 |
| Actual outputs | 1.0003 | 1.0003 | 0.9998 | 1.0001 | 0.0000 | 0.0000 | 0.0000 | 0.0005 |
| | -0.0001 | -0.0001 | 0.0001 | 0.0030 | 1.0001 | 1.0001 | 0.9999 | 1.0002 |
| | 0.9999 | 0.9999 | 1.0002 | 1.0025 | 0.0001 | 0.0001 | 0.0000 | -0.0004 |
| | -0.0002 | -0.0001 | -0.0001 | 0.0014 | 1.0000 | 1.0001 | 1.0000 | 0.9999 |

TABLE 11: Damage severity identification result of multidamage using strain ratio as parameter.

| Output results | Testing cases | | | | | | | |
|---------------------|---------------|-------|-------|--------|--------|-------|-------|--------|
| | M1 | M2 | M3 | M4 | M5 | M6 | M7 | M8 |
| Expected outputs | 0.2 | 0.3 | 0.35 | 0.4 | 0 | 0 | 0 | 0 |
| | 0 | 0 | 0 | 0 | 0.2 | 0.3 | 0.35 | 0.4 |
| | 0.3 | 0.35 | 0.35 | 0.2 | 0 | 0 | 0 | 0 |
| | 0 | 0 | 0 | 0 | 0.3 | 0.35 | 0.35 | 0.2 |
| Actual outputs | 0.205 | 0.302 | 0.349 | 0.397 | -0.001 | 0.000 | 0.000 | 0.000 |
| | 0.000 | 0.000 | 0.000 | -0.001 | 0.203 | 0.301 | 0.349 | 0.410 |
| | 0.307 | 0.350 | 0.348 | 0.200 | 0.000 | 0.000 | 0.000 | -0.003 |
| | 0.000 | 0.000 | 0.000 | 0.003 | 0.307 | 0.348 | 0.348 | 0.203 |
| Relative errors (%) | 2.39 | 0.64 | 0.42 | 0.64 | | | | |
| | | | | | 1.69 | 0.21 | 0.37 | 2.41 |
| | 2.17 | 0.02 | 0.62 | 0.17 | | | | |
| | | | | | 2.42 | 0.43 | 0.55 | 1.71 |

TABLE 12: Damage cases for comparative analysis.

| Damage section | Damage severity |
|------------------|--|
| Sections 1 and 3 | 20%-20%; 20%-30%; 20%-35%; 20%-40%; 30%-20%; 30%-30%; 30%-35%; 30%-40%; 35%-20%; 35%-30%; 35%-35%; 35%-40%; 40%-20%; 40%-30%; 40%-35%; 40%-40%; |

TABLE 13: Identification results of hybrid neurogenetic algorithm and BP.

| Output results | Methods | | | |
|------------------|-------------------------------|------|-------------|-------|
| | Hybrid neurogenetic algorithm | | BP networks | |
| Expected outputs | 0.2 | 0.3 | 0.2 | 0.3 |
| | 0 | 0 | 0 | 0 |
| | 0.35 | 0.4 | 0.35 | 0.4 |
| | 0 | 0 | 0 | 0 |
| Actual outputs | 0.21 | 0.29 | 0.2 | 0.31 |
| | 0.00 | 0.02 | -0.02 | 0.01 |
| | 0.34 | 0.40 | 0.38 | 0.42 |
| | -0.01 | 0.00 | 0.01 | -0.02 |
| Errors (%) | 5 | 3.33 | 0 | 3.33 |
| | 2.86 | 0 | 8.57 | 5 |

is 5% and 8.57%, respectively. Hybrid neurogenetic algorithm possesses more favorable results for damage identification.

As for using static and dynamic properties as input variables, the damage identification effect using strain ratio as input variable is more favorable. However, the frequency ratio is more convenient to obtain in practical application.

Conflict of Interests

The authors declare that there is no conflict of interests regarding the publication of this paper.

Acknowledgments

The authors express their appreciation for the financial support of National Natural Science Foundation of China under Grant nos. 51408258, 51378236, and 51278222, China Post-doctoral Science Foundation funded project (2014M560237), Fundamental Research Funds for the Central Universities and Science (JCKY-QKJC06), and Technology Development Program of Jilin Province (20140203002SF). The authors are very grateful for the reviewers and TMEE 2011.

References

[1] N. Kulprapha and P. Warnitchai, "Structural health monitoring of continuous prestressed concrete bridges using ambient thermal responses," *Engineering Structures*, vol. 40, pp. 20-38, 2012.

- [2] A. Rytter, *Vibration based inspection of civil engineering structures [Ph.D. thesis]*, Department of Building Technology and Structural Engineering, Aalborg University, Aalborg, Denmark, 1993.
- [3] J. V. A. dos Santos, C. M. M. Soares, C. A. M. Soares, and N. M. M. Maia, "Structural damage identification: influence of model incompleteness and errors," *Composite Structures*, vol. 62, no. 3-4, pp. 303-313, 2003.
- [4] P. Lu, *A statistical based damage detection approach for highway bridge structural health monitoring [Ph.D. thesis]*, Iowa State University, Ames, Iowa, USA, 2008.
- [5] M. Chandrashekhar and R. Ganguli, "Damage assessment of structures with uncertainty by using mode-shape curvatures and fuzzy logic," *Journal of Sound and Vibration*, vol. 326, no. 3-5, pp. 939-957, 2009.
- [6] A. K. Pandey, M. Biswas, and M. M. Samman, "Damage detection from changes in curvature mode shapes," *Journal of Sound and Vibration*, vol. 145, no. 2, pp. 321-332, 1991.
- [7] Y. Xia, H. Hao, J. M. W. Brownjohn, and P.-Q. Xia, "Damage identification of structures with uncertain frequency and mode shape data," *Earthquake Engineering and Structural Dynamics*, vol. 31, no. 5, pp. 1053-1066, 2002.
- [8] D. Ribeiro, R. Calçada, R. Delgado, M. Brehm, and V. Zabel, "Finite element model updating of a bowstring-arch railway bridge based on experimental modal parameters," *Engineering Structures*, vol. 40, pp. 413-435, 2012.
- [9] O. S. Salawu, "Detection of structural damage through changes in frequency: a review," *Engineering Structures*, vol. 19, no. 9, pp. 718-723, 1997.
- [10] M. A.-B. Abdo and M. Hori, "A numerical study of structural damage detection using changes in the rotation of mode shapes," *Journal of Sound and Vibration*, vol. 251, no. 2, pp. 227-239, 2002.
- [11] P. Z. Qiao, K. Lu, W. Lestari, and J. L. Wang, "Curvature mode shape-based damage detection in composite laminated plates," *Composite Structures*, vol. 80, no. 3, pp. 409-428, 2007.
- [12] Q. Lu, G. Ren, and Y. Zhao, "Multiple damage location with flexibility curvature and relative frequency change for beam structures," *Journal of Sound and Vibration*, vol. 253, no. 5, pp. 1101-1114, 2003.
- [13] P. Cawley and R. D. Adams, "The location of defects in structures from measurements of natural frequencies," *Journal of Strain Analysis for Engineering Design*, vol. 14, no. 2, pp. 49-57, 1979.
- [14] G. H. Guo and W. J. Yi, "A numerical study on the damage assessment of a simply-supported beam on natural frequencies," *Journal of Chongqing Jianshu University*, vol. 23, pp. 17-21, 2001.
- [15] D. P. Patil and S. K. Maiti, "Detection of multiple cracks using frequency measurements," *Engineering Fracture Mechanics*, vol. 70, no. 12, pp. 1553-1572, 2003.
- [16] J.-T. Kim and N. Stubbs, "Crack detection in beam-type structures using frequency data," *Journal of Sound and Vibration*, vol. 259, no. 1, pp. 145-160, 2003.
- [17] B. Sahoo and D. Maity, "Damage assessment of structures using hybrid neuro-genetic algorithm," *Applied Soft Computing Journal*, vol. 7, no. 1, pp. 89-104, 2007.
- [18] C. Na, S.-P. Kim, and H.-G. Kwak, "Structural damage evaluation using genetic algorithm," *Journal of Sound and Vibration*, vol. 330, no. 12, pp. 2772-2783, 2011.
- [19] J. J. Lee, J. W. Lee, J. H. Yi, C. B. Yun, and H. Y. Jung, "Neural networks-based damage detection for bridges considering errors in baseline finite element models," *Journal of Sound and Vibration*, vol. 280, no. 3-5, pp. 555-578, 2005.
- [20] C. Y. Kao and S.-L. Hung, "Detection of structural damage via free vibration responses generated by approximating artificial neural networks," *Computers and Structures*, vol. 81, no. 28-29, pp. 2631-2644, 2003.
- [21] X. Fang, H. Luo, and J. Tang, "Structural damage detection using neural network with learning rate improvement," *Computers and Structures*, vol. 83, no. 25-26, pp. 2150-2161, 2005.
- [22] M. Mehrjoo, N. Khaji, H. Moharrami, and A. Bahreininejad, "Damage detection of truss bridge joints using Artificial Neural Networks," *Expert Systems with Applications*, vol. 35, no. 3, pp. 1122-1131, 2008.
- [23] N. Bakhary, H. Hao, and A. J. Deeks, "Damage detection using artificial neural network with consideration of uncertainties," *Engineering Structures*, vol. 29, no. 11, pp. 2806-2815, 2007.
- [24] M. T. Hagan, H. B. Demuth, and M. H. Beale, *Neural Network Design*, University of Colorado Bookstore, 2002.
- [25] H.-B. Liu and Y.-B. Jiao, "Application of genetic algorithm-support vector machine (GA-SVM) for damage identification of bridge," *International Journal of Computational Intelligence and Applications*, vol. 10, no. 4, pp. 383-397, 2011.
- [26] A. Rabiee, H. Sayyad, M. Riazi, and A. Hashemi, "Determination of dew point pressure in gas condensate reservoirs based on a hybrid neural genetic algorithm," *Fluid Phase Equilibria*, vol. 387, pp. 38-49, 2015.
- [27] A. Azadeh, S. F. Ghaderi, S. Tarverdian, and M. Saberi, "Integration of artificial neural networks and genetic algorithm to predict electrical energy consumption," *Applied Mathematics and Computation*, vol. 186, no. 2, pp. 1731-1741, 2007.
- [28] D. E. Goldberg, *Genetic Algorithm in Search, Optimization and Machine Learning*, Addison-Wesley, Harlow, UK, 1989.

Research Article

An Analytical Approach for Deformation Shapes of a Cylindrical Shell with Internal Medium Subjected to Lateral Contact Explosive Loading

Xiangyu Li, Zhenduo Li, and Minzu Liang

College of Science, National University of Defense Technology, Changsha 410073, China

Correspondence should be addressed to Xiangyu Li; xiangyulee@nudt.edu.cn

Received 27 February 2015; Revised 18 June 2015; Accepted 24 June 2015

Academic Editor: Yuri Petryna

Copyright © 2015 Xiangyu Li et al. This is an open access article distributed under the Creative Commons Attribution License, which permits unrestricted use, distribution, and reproduction in any medium, provided the original work is properly cited.

An experimental investigation on deformation shape of a cylindrical shell with internal medium subjected to lateral contact explosion was carried out briefly. Deformation shapes at different covered width of lateral explosive were recovered experimentally. Based on the experimental results, a corresponding analytical approach has been undertaken with rigid plastic hinge theory. In the analytical model, the cylindrical shell is divided into end-to-end rigid square bars. Deformation process of the cylindrical shell is described by using the translations and rotations of all rigid square bars. Expressions of the spring force, buckling moment, and deflection angle between adjacent rigid square bars are conducted theoretically. Given the structure parameters of the cylinder and the type of the lateral explosive charge, deformation processes and shapes are reported and discussed using the analytical approach. A good agreement has been obtained between calculated and experimental results, and thus the analytical approach can be considered as a valuable tool in understanding the deformation mechanism and predicting the deformation shapes of the cylindrical shell with internal medium subjected to lateral contact explosion. Finally, parametric studies are carried out to analyze the effects of deformation shape, including the covered width of the lateral explosive, explosive charge material, and distribution of initial velocity.

1. Introduction

Cylindrical shells are used in a wide variety of engineering applications, from the containment pressure vessels of nuclear reactors to the bracing elements of aerospace structures. Such structures may be subjected to a wide variety of short duration transient loads throughout the course of their working life, such as air blasts, underwater explosions, and high velocity impact. Accurate prediction of the dynamic plastic deformation and rupture of the cylindrical shell subjected to high intensity transient loading is of great importance in many industrial applications.

Early researches on the dynamic buckling and failure of cylinders were restricted to axisymmetric external radial pulse loading [1] and axial impact loading. However, the corresponding analysis, though presented in an elegant analytical form, is of limited applicability because axisymmetric dynamic loading seldom occurs in practice. In real world

situations loading is usually applied to one side of the cylinder and is characterized by various degrees of locality. It may consist of a projectile, missile or mass impact, standoff explosion described by a pressure pulse, or contact explosion often approximated as an ideal impulsive loading.

Depending on the load intensity and the special distribution of contact pressures, various forms of damage may result ranging from large amplitude lateral deflections to punch-through penetration, fracture initiation at the base plate, progression of tearing fracture, and finally massive structural damage. Yakupov [2, 3] studied the dynamic response of the cylindrical shell subjected to a planar plastic shock wave with rigid plastic hinge theory and presented the residual deformation of the cylindrical shell as a function of a planar wave pressure. Gefken et al. [4] extended the earlier analysis by Lindberg and Florence to one-side inward radial pressure that varied as the cosine of the angular position around the shell and was uniform along length, to identify the structural

response modes of thin cylindrical shell, with and without internal pressure, subjected to external radial impulsive loads. For unpressurized shells the response modes consisted of dynamic pulse buckling followed by large inward deflections of the loaded surface. In shell with high internal pressure, these response modes were followed by an outward motion driven by the internal pressure. Fatt and Wierzbicki [5] and Wierzbicki and Fatt [6] investigated the large amplitude transient response of plastic cylindrical shells using a string-on-foundation model, and the model incorporated two main load-resistance mechanisms in the shell: stretching in the longitudinal direction and bending in the circumferential direction. Jiang and Olson [7] presented a numerical model for large deflection, elastic-plastic analysis of the cylindrical shell structures under air blast loading condition based on a transversely curved finite strip formulation. Li and Jones [8] studied the dynamic response of a “short” cylindrical shell, which is made from a rigid, perfectly plastic material, and the plastic behavior of the material is controlled by the transverse shear force as well as the circumferential membrane and the longitudinal bending moment.

In recent years, increasing attention of both engineering communities and government agencies has turned to the dynamic response of the cylindrical shell subjected to underwater explosion. Pédrón and Combescure [9] presented a modal method of analysis to determine the response of an infinitely long stiffened cylindrical shell of revolution lateral pressure produced by an underwater explosion and propagating in an acoustic fluid. Rajendran and Lee [10] studied comparative damage of air-backed and water-backed plates subjected to noncontact underwater explosion. Hung et al. [11] investigated the linear and nonlinear dynamic responses of three cylindrical shell structures subjected to underwater small charge explosion under different standoff distances. The three cylindrical shell structures were unstiffened, internally stiffened, and externally stiffened, respectively. Li and Rong [12] studied the dynamic response of the cylindrical shell structures subjected to underwater explosion by using experimental and numerical methods. Li et al. [13] investigated two kinds of the cylindrical shell models with the same geometry characteristics: unfilled and main hull sand-filled. The main hull sand-filled cylindrical shell is more difficult to be damaged by the shock wave loading than the unfilled model. Hu et al. [14] studied the effects of elastic modulus, shell radius, and thickness on the transient response characteristics of the cylindrical shell. Yao et al. [15] presented a new shock factor based on energy acting on the structure to describe the loading of underwater explosion. Jama et al. [16] reported an experimental and analytical investigation of steel square hollow sections subjected to transverse blast load, and the energy dissipated in the local deformation is discussed. In recent decades, the research on the performance of the cylindrical shell is still very limited. A series of analytical models have been developed, to predict the dynamic response of a cylindrical shell subjected to a lateral shock loading, or localized loading, or underwater explosion. Because of complexities introduced by unsymmetric loading, large displacements, and rotations of the shell amplified by material nonlinearities, the problem does not lend itself

easily to an analytical treatment. However, very few studies have been reported on cylindrical shell filled with medium subjected to contact explosion loading.

To investigate the behavior of the cylindrical shell with internal medium loaded by lateral contact explosion, several experiments have been conducted, and the experimental results are presented and discussed in detail in this paper. Based on the experiments, a corresponding analytical approach was conducted with rigid plastic hinge theory. Deformation processes of cylindrical shells are described using the translations and rotations of all rigid square bars. In this study, an infinitely long cylindrical shell filled with medium subject to lateral contact explosion is performed. Because the cylindrical shell has the unique deformation shape in the symmetric axis direction, we take a ring representing the cylinder. Due to solving the inertia moment of the ring, a unit height ring represents deformation of the infinite cylinder. Because the ring has the same value of thickness and height in the radial and axial direction, the cross section of the ring in the circumferential direction is square, so we call it “square bar.”

Given the structural parameters of the ring and the type of the explosive charge, deformation processes and shapes are reported using the analytical approach. A good agreement has been obtained between calculated and experimental results. Finally, parametric studies are carried out to analyze the effects of deformation shapes, depending on the covered width of the lateral explosive, explosive charge material, and distribution of initial velocity.

2. Experimental Procedure and Results

2.1. Experimental Procedure. In order to investigate the dynamic response of the cylindrical shell with internal medium subjected to lateral contact explosion loading, some experiments were carried out with respect to the different covered widths of the lateral explosive charge. The photography and assembly schematics of experimental setups are shown in Figures 1 and 2, respectively.

The experimental setup consists of a cylindrical shell with internal medium (sand), a lateral explosive charge, a connecting rod, and two endplates. The thickness t , the outer radius r_1 , and the axial length H of the cylindrical shell, made from 1020 Steel, are 2 mm, 100 mm, and 220 mm, respectively. The radius of the cylindrical shell is more than 10 times the thickness. The internal medium with a center hole reserved is local sand, having a density of 1.75 g/cm^3 . Two endplates, made from LY12 Aluminium, having a thickness of 10 mm, are fixed by the connecting rod so that fully closed condition will be simulated. Material properties of 1020 Steel, LY12 Aluminum, and sand are listed in Table 1.

The lateral charge is an emulsion explosive (DL103-80), which is made from 75% PETN, 20% emulsion, and 5% Pb_3O_4 , and the density is 0.95 g/cm^3 . The emulsion explosive DL103-80 is a sort of mild and flexible material that can be easily shaped. The inner radius, the thickness, and the covered width of the lateral explosive charge are 100 mm, 5 mm, and φ , respectively. The explosion of each test is initiated by an electric detonator on the top of the lateral explosive charge.

TABLE 1: Material properties of 1020 Steel, LY12 Aluminium, and sand.

| Material | Density (g/cm ³) | Yield stress (MPa) | Young's modulus (GPa) | Poisson's ratio |
|----------------|------------------------------|--------------------|-----------------------|-----------------|
| 1020 Steel | 7.85 | 275 | 210 | 0.29 |
| LY12 Aluminium | 2.78 | 230 | 70 | 0.29 |
| Sand | 1.75 | 4.23 | 0.01 | 0.26 |

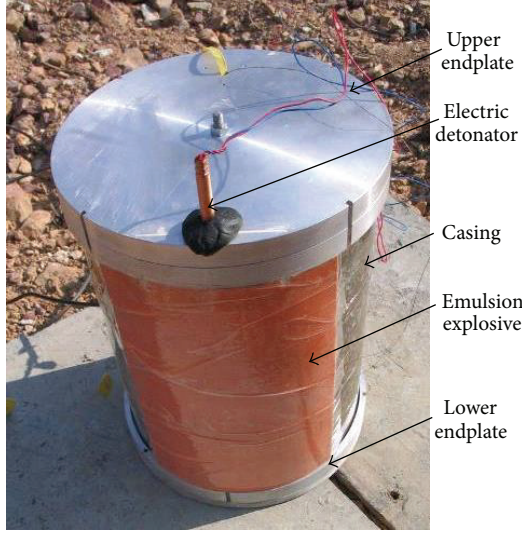


FIGURE 1: Photography of the experimental setups.

2.2. Experimental Results. Deformation shapes of the cylindrical shell with internal medium at three different covered widths of the lateral explosive charge were recovered. Deformation shapes after tests are shown in Figure 3. From the deformation shapes recovered, the angle of the lateral charge has a significant effect on the deformation shape, and the deformation shapes are concave, linear, and convex when the covered widths of lateral charges are 45°, 90°, and 135°, respectively.

3. Analytical Model

3.1. Basic Assumptions. Deformation processes of the cylindrical shell with internal medium subjected to lateral contact explosion are a high nonlinear problem. Due to complexities introduced by unsymmetric loading, large displacements, and rotations of the cylinder amplified by material nonlinearities, the problem does not lend itself easily to an analytical treatment. However, by introducing a suitable set of assumptions, a simple and realistic model can be established to describe the deformation processes of the cylindrical shell with internal medium.

Basic assumptions are as follows: (1) the cylindrical shell is infinitely long, and the axial thickness selected is equal to the thickness of cylinder; (2) the cylinder is divided into end-to-end rigid square bars along the circumferential direction; (3) the square bars close to the lateral explosive charges have an instantaneous velocity pointing to the centre of the cylinder.

During deformation processes of the cylindrical shell, some parameters of square bars may vary at different moments, such as translational displacements, translational velocities, rotational displacements, rotational angles, and area surrounded by square bars, which affect the value of the spring force, the bending moment, and the deflection angle intensively.

3.2. Analytical Approach. Based on the above-mentioned assumptions, the analytical model is established, shown in Figure 4, where the origins for x and y are given, and the range x is from 0 to $2r_i$, and the range y is from $-r_i$ to r_i . The cylindrical shell is divided into end-to-end rigid square bars along the circumferential direction. The arc length l of each square bar is $2\pi r_1/N$ (N is the total number of square bars). The relationships between two adjacent square bars are established by using a spring force, a bending moment, and a deflection angle.

The spring force between adjacent square bars assumed as the perfect elastic-plastic is described by a changeable spring force (Figure 5). The spring force between adjacent square bars is expressed by the equation

$$F = \begin{cases} E \cdot s \cdot t^2 & s \leq s_0 \\ \sigma_y \cdot t^2 & s > s_0, \end{cases} \quad (1)$$

where E , σ_y , and s_0 are Young's modulus, the yield stress, and the elastic limit displacement of bar, respectively. F is the spring force between adjacent square bars, and s is the relative displacement between the end of the current bar and the head of the next bar.

The relative displacements between the end of the current bar and the head of the next bar are obtained by using the end displacement of the current square bar subtracting the head displacement of the next square bar. The relative displacements of adjacent square bars are described by the equation

$$\begin{aligned} s_x(i) &= \left[dt \cdot v_x(i) - \frac{l \cdot \theta(i)}{2} \sin \alpha(i) \right] \\ &\quad - \left[dt \cdot v_x(i+1) - \frac{l \cdot \theta(i+1)}{2} \sin \alpha(i+1) \right], \\ s_y(i) &= \left[dt \cdot v_y(i) + \frac{l \cdot \theta(i)}{2} \cos \alpha(i) \right] \\ &\quad - \left[dt \cdot v_y(i+1) + \frac{l \cdot \theta(i+1)}{2} \cos \alpha(i+1) \right], \end{aligned} \quad (2)$$

where $s_x(i)$ and $s_y(i)$ are relative displacements between two adjacent square bars in the x -axis and y -axis directions,

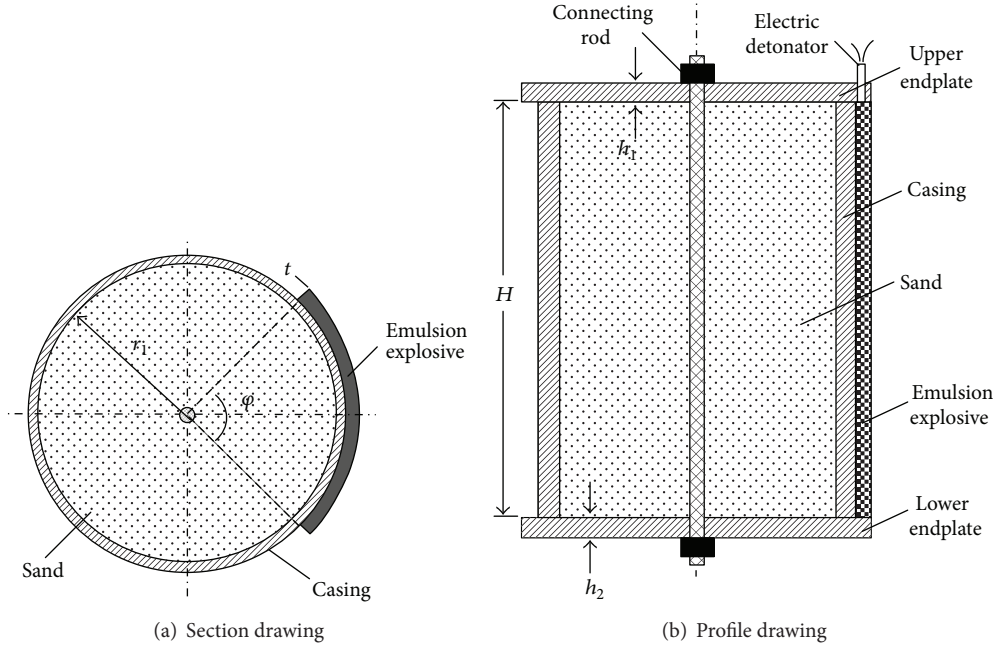


FIGURE 2: Assembly schematics of experimental setups: (a) section drawing and (b) profile drawing.

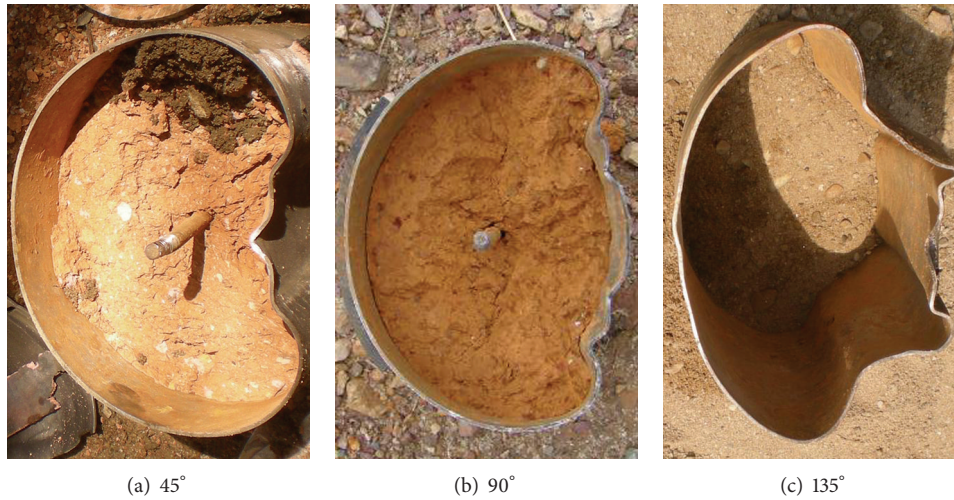


FIGURE 3: Experimental result of deformation shapes after tests at three different covered widths of the lateral explosive charge.

respectively. dt is a time step. $v_x(i)$ and $v_y(i)$ are translational velocities of the current square at the x -axis and y -axis directions, respectively. $v_x(i+1)$ and $v_y(i+1)$ are translational velocities of the next square at the x -axis and y -axis directions, respectively. $\theta(i)$ is the relative deflection angle between two adjacent square bars. The spring force between two adjacent square bars is calculated by the following equation when $s_x(i)$ and $s_y(i)$ are less than s_0 :

$$\begin{aligned} F_x(i) &= E \cdot t^2 \cdot s_x(i), \\ F_y(i) &= E \cdot t^2 \cdot s_y(i), \end{aligned} \quad (3)$$

where $F_x(i)$ and $F_y(i)$ are spring forces between two adjacent square bars in the x -axis and y -axis directions, respectively.

Bending moment and corresponding deflection angle between two adjacent square bars are shown in Figure 6. Based on the rigid plastic hinge theory, the plastic hinges are achieved when the bending moment of the square bar reaches the plastic ultimate bending moment. During the deformation processes of the cylindrical shell, the relationships between the bending moment M and the deflection angle θ are assumed to be linear when the bending moment is less than the plastic ultimate bending moment M_p . Meanwhile, the deflection θ is set to the plastic limit deflection angle θ_p when the bending moment is greater than or equal to the plastic ultimate bending moment.

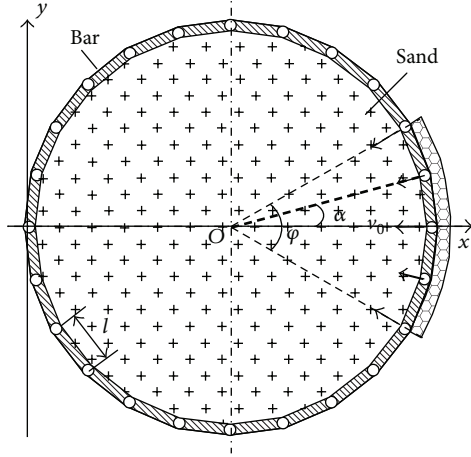


FIGURE 4: Analytical model.

The relationship between the bending moment and the deflection angle is expressed by the equation

$$\theta = \begin{cases} \frac{Ml}{EI} & M < M_p \\ \theta_p & M \geq M_p \end{cases} \quad (4)$$

where M is the bending moment; I is the moment of inertia, which is equal to $t^4/12$; θ is the deflection angle; M_p is the plastic ultimate bending moment, which is equal to $t^3\sigma_y/4$.

Moment of each square bar consists of two aspects: the moment generated by the spring force and the moment resulting from the bar bending. Moments of square bars are described by the equation

$$\begin{aligned} M_h(i) &= \left(\frac{l}{2}\right) \cdot F_x(i-1) \sin \alpha(i) - \left(\frac{l}{2}\right) \\ &\quad \cdot F_y(i-1) \cos \alpha(i) + M(i), \\ M_e(i) &= \left(\frac{l}{2}\right) \cdot F_x(i) \sin \alpha(i) - \left(\frac{l}{2}\right) \\ &\quad \cdot F_y(i) \cos \alpha(i) - M(i), \end{aligned} \quad (5)$$

where $M_h(i)$ and $M_e(i)$ are the moment generated by the spring force at the head and end of the current square bar, respectively. $M(i)$ is the moment generated by the relative bending between two adjacent square bars.

The internal medium is compressed because of the translation and rotation of square bars. During movement processes of all bars, interactions between square bars and internal medium are shown in Figure 7, where velocities of previous bar, current bar, and next bar are $v(i-1)$, $v(i)$, and $v(i+1)$, respectively. The resistance forces suffered by the internal medium are $f(i-1)$, $f(i)$, and $f(i+1)$, respectively.

It is assumed that the processes of the internal medium compressed undergo two stages. The first stage is that voids of internal medium are compacted, and the resistance force of each square bar is equal to $\rho_e t^2 (\vec{v} \cdot \vec{n}l) \vec{v}$, where ρ_e is the internal medium density. The second stage is that medium

compacted suffers a shock compression, and the relationship between shock pressure and volume is assumed to be linear:

$$p = \frac{\eta(dV - j_0 \cdot V_0)}{(1 - j_0) \cdot V_0}, \quad (6)$$

where p is the shock pressure; η is a scale factor; V_0 and dV are the initial volume and the compression volume of internal medium, respectively; j_0 is the compression ratio of medium.

The resistance forces of bar generated by internal medium during the two stages are expressed by the equation

$$\vec{f} = \begin{cases} \rho_e t^2 (\vec{v} \cdot \vec{n}l) \vec{v} & j < j_0 \\ pt \cdot \vec{n}l & j \geq j_0 \end{cases} \quad (7)$$

By calculating the spring forces between adjacent square bars and the resistance forces generated by the internal medium, translational accelerations of all square bars are obtained at corresponding time. By calculating the bending moments of all square bars, the rotational accelerations are obtained at corresponding time. The translational and rotational accelerations of square bars are described by

$$\begin{aligned} \vec{a}(i) &= \frac{\vec{f}(i) + \vec{F}(i-1) + \vec{F}(i)}{m}, \\ \beta(i) &= \frac{M_h(i) + M_e(i)}{I}, \end{aligned} \quad (8)$$

where $\alpha(i)$ and $\beta(i)$ are the translational and rotational accelerations of the current square bar, respectively.

Utilizing (8), the translational and rotational accelerations are calculated, which are the initial conditions at the next time step.

3.3. Initial Conditions. Initial translational acceleration, rotational acceleration, and velocities of all square bars are set to 0, and the distributions of initial velocities are as follows:

$$\vec{v} = \begin{cases} [v_0 \cos \alpha, v_0 \sin \alpha] & -\frac{\varphi}{2} \leq \alpha \leq \frac{\varphi}{2} \\ 0 & \alpha < -\frac{\varphi}{2}, \alpha > \frac{\varphi}{2} \end{cases} \quad (9)$$

where φ is the half angle covered by the lateral explosive charge, α is the angle between the current square bar and x -axis, and v_0 is the initial velocity of cylindrical shell close to the lateral explosive charge.

According to the Gurney equations on contact explosion, the ring velocity can be obtained by using the equation [17]

$$v_0 = \sqrt{2E} \sqrt{\frac{3}{1 + 5M_f/C_e + 4(M_f/C_e)^2}}, \quad (10)$$

where v_0 is the ring velocity (m/s); $\sqrt{2E}$ is the Gurney energy unit mass (m/s); C_e is the mass of lateral explosive charge (kg); M_f is the mass of the cylindrical shell close to the lateral charge (kg). The Gurney equation is a classical method to solve the metal velocity in recent decades, the error between the experimental and calculated results is about 5%, and its accuracy is acceptable for our work.

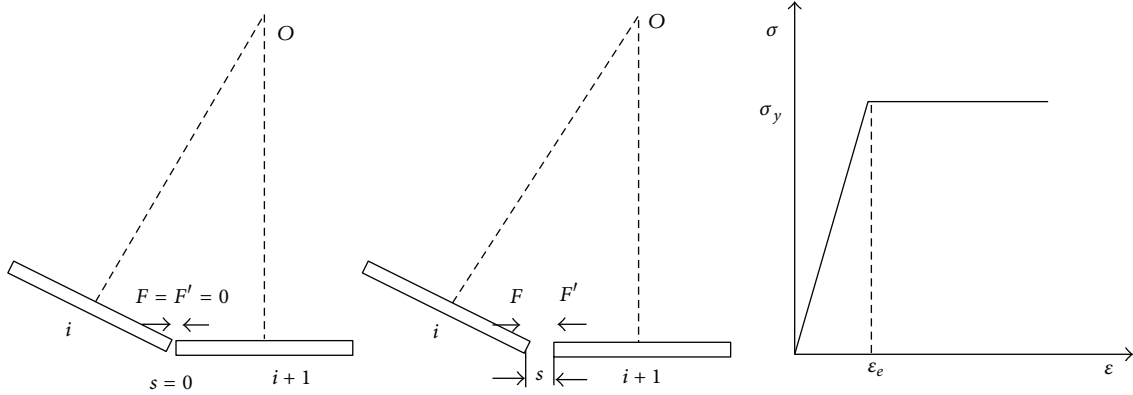


FIGURE 5: Spring force between two adjacent square bars.

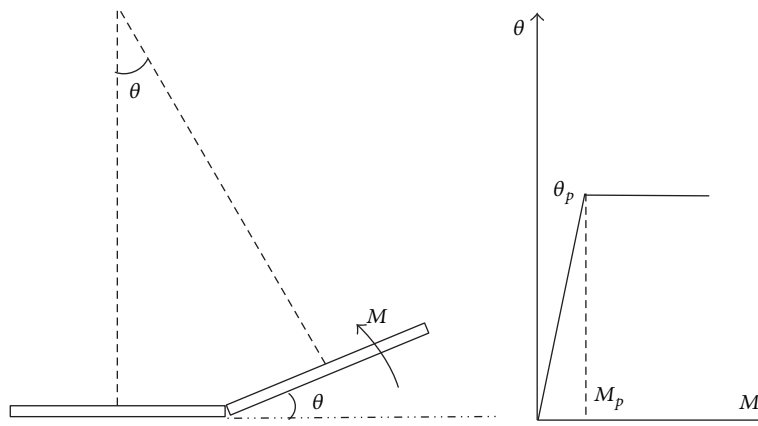


FIGURE 6: Bending moment and deflection angle between bars.

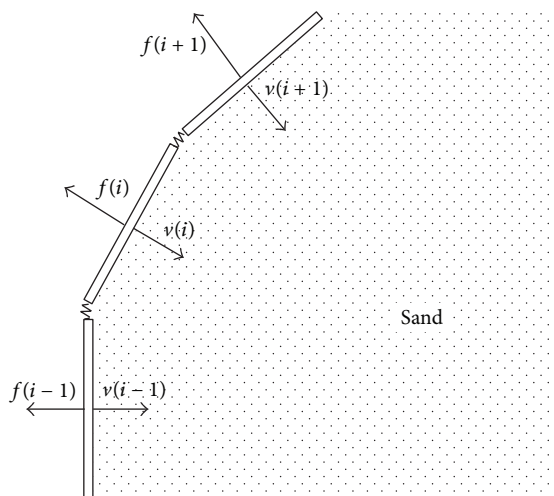


FIGURE 7: Interactions between square bars and internal medium.

4. Calculated Results

According to specific structure parameters and the type of the explosive charge, the velocity of the ring can be obtained with (8). It is assumed that the ring, made of 1020 Steel,

has a thickness of 2 mm, and the explosive, made of DL103-80, has the thickness of 5 mm. Based on detonation parameters of DL103-80, substituting these parameters into the Gurney equation, the velocity is approximately 200 m/s. If the explosive DL103-80 is replaced with RDX or HMX, the velocity is greater, and the different initial velocity distribution can be obtained by varying the explosive charge material and the explosive mass.

Based on the analytical approach, calculated results are reported and discussed. Deformation processes of the cylindrical shell consist of two stages: stage I, velocities of the cylindrical shell obtained by the lateral contact explosion loading, and stage II, interactions between the cylindrical shell and internal medium. Figure 8 illustrates distribution of positions and velocities of the cylindrical shell at five different moments under the covered width 45° and the initial velocity of the cylindrical shell 200 m/s, respectively. Figures 9 and 10 show distributions of positions and velocities of the cylindrical shell at five classical times under the covered widths 90° and 135°, respectively. The ultimate translational velocities of the cylindrical shell are 6.1 m/s, 7.3 m/s, and 10.9 m/s with the covered widths 45°, 90°, and 135°, respectively.

From the results of deformation shapes, a good agreement has been obtained between calculated and experimental results, and thus the analytical approach can be considered as

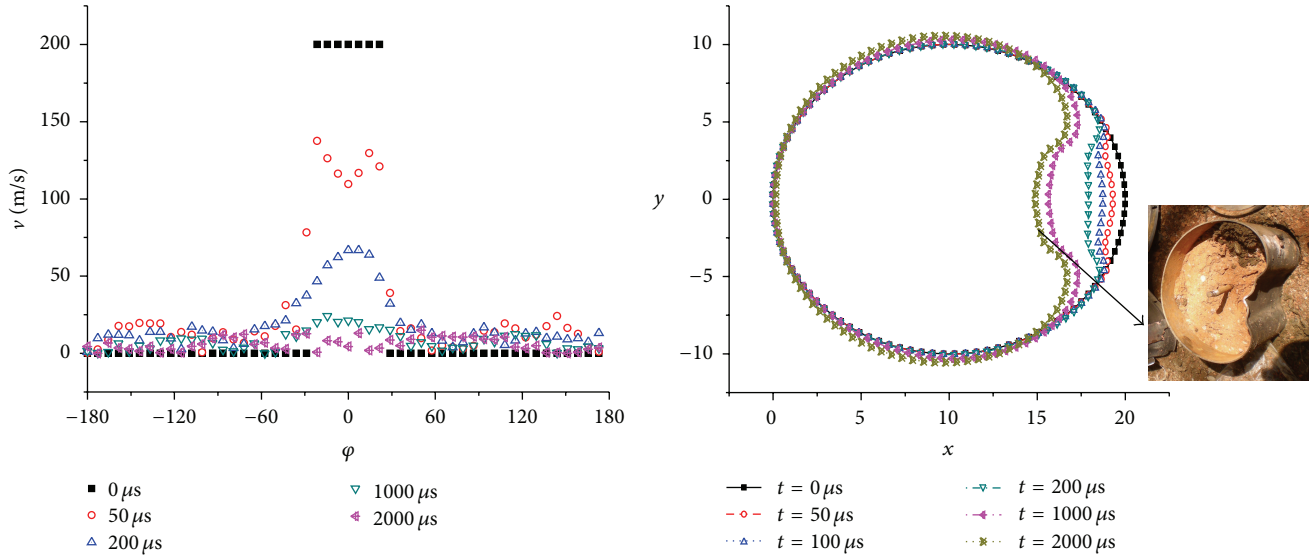


FIGURE 8: Distributions of positions and velocities of the cylindrical shell at different moments ($\varphi = 45^\circ$).

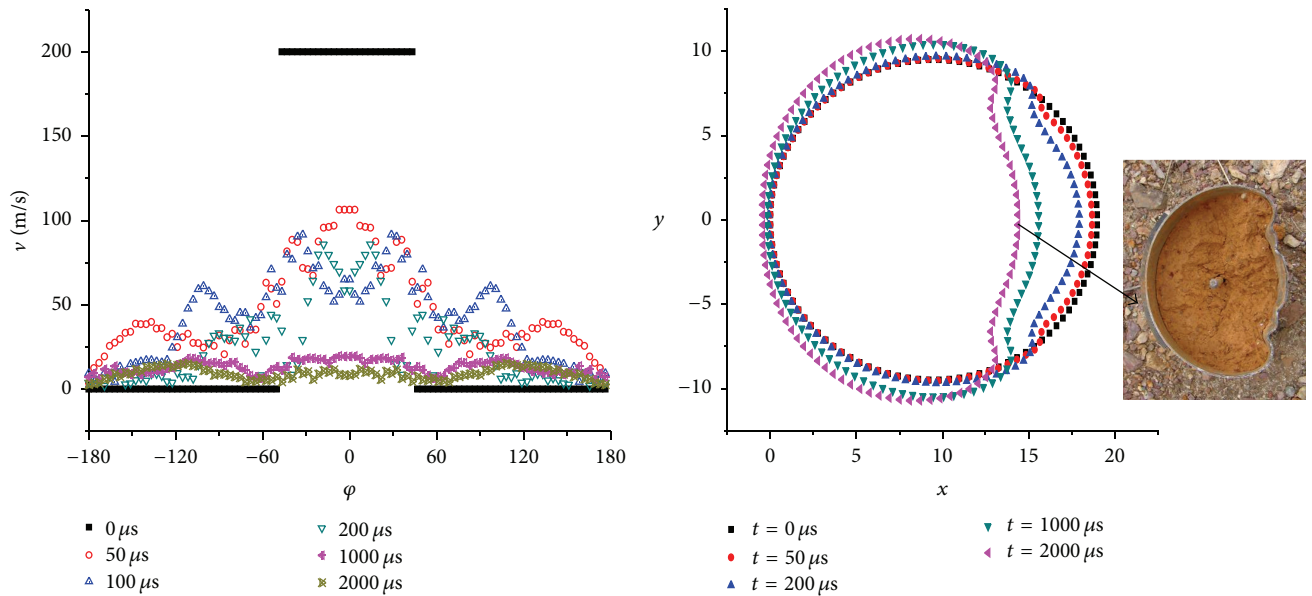


FIGURE 9: Distributions of positions and velocities of the cylindrical shell at different moments ($\varphi = 90^\circ$).

a valuable tool in understanding the deformation mechanism and predicting the deformation shape of the cylindrical shell under lateral contact explosion loading.

5. Parametric Studies

Deformation shapes of the ring have a significant relationship with the covered width of lateral explosive, explosive materials, and initial velocities distribution. In order to better understand the deformation mechanism, parametric studies are carried out for the deformation shapes and corresponding results were discussed.

5.1. *Effect of Covered Width of Lateral Explosive.* From the calculated and experimental results, it is obvious that the covered width of the lateral explosive charge is a key factor to the deformation shapes. Deformation shapes of various covered widths of the lateral charge are shown in Figure 11, where initial velocity of the ring equals 200 m/s. Various deformation shapes can be achieved by changing the width of lateral charge.

5.2. *Effect of Lateral Explosive Materials.* In order to investigate the effect of lateral charge, a series of calculated results are obtained by adjusting various initial velocities

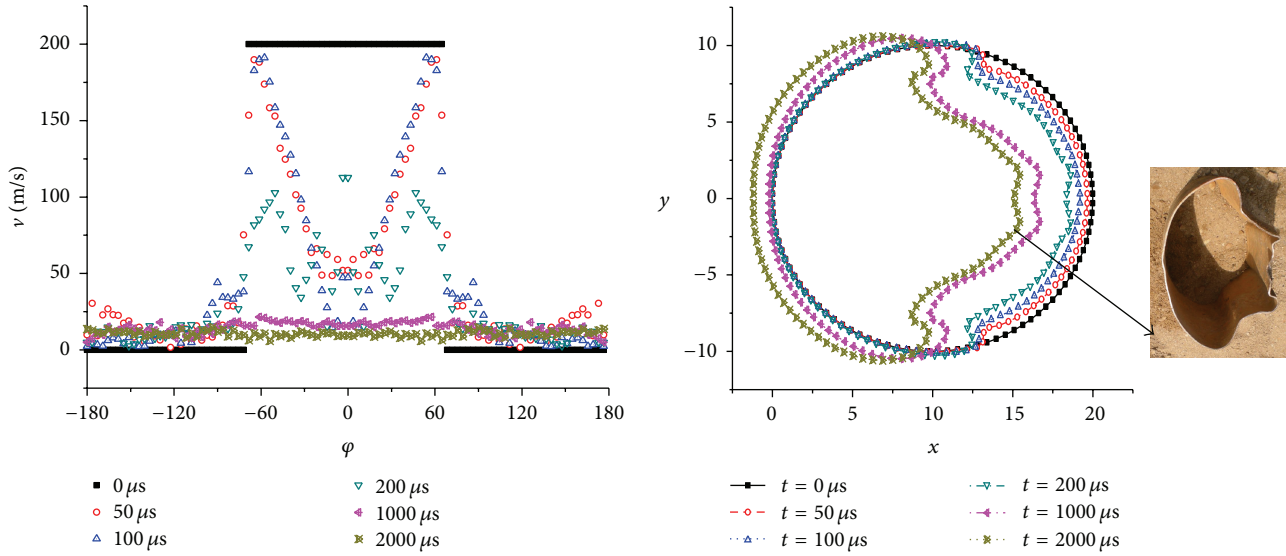


FIGURE 10: Distributions of positions and velocities of the cylindrical shell at different moments ($\varphi = 135^\circ$).

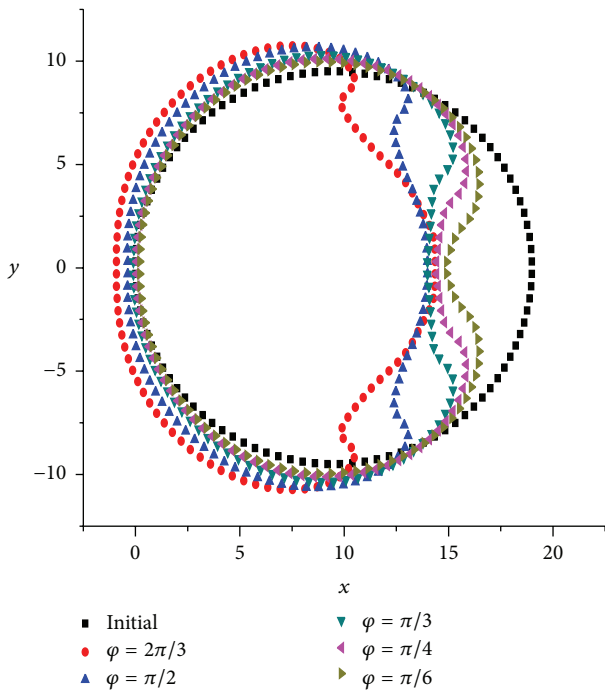


FIGURE 11: Deformation shapes of the cylindrical shell at various widths of lateral explosive charge ($v_0 = 200$ m/s).

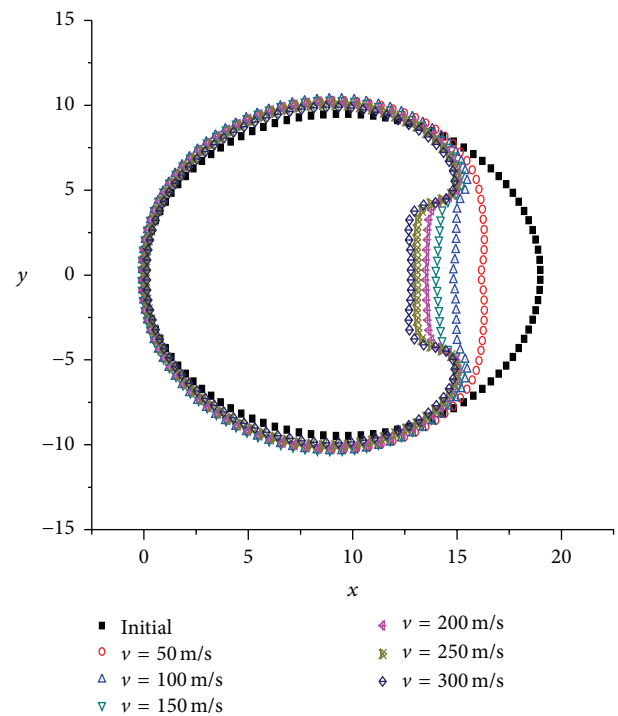


FIGURE 12: Deformation shapes of the cylindrical shell at various initial velocities ($\varphi = 60^\circ$).

of the cylindrical shell, because higher initial velocities of cylindrical shell represent greater power of charge.

Figure 12 shows the deformation shapes of the cylindrical shell at various initial velocities with the covered width 60° , in which velocities are 50 m/s, 100 m/s, 150 m/s, 200 m/s, 250 m/s, and 300 m/s, respectively. The compression capacity of the sand medium increases with initial velocities; while initial velocities reach a certain extent, there is little change in deformation shapes.

5.3. *Effect of Initial Velocities Distribution.* In general, the lateral explosive charge has a uniform thickness in the circumferential direction within the central angle, and the ring close to the lateral explosive has the same velocity value. The velocity values varies with thickness of the circumferential explosive. The simplest assumption is that the thickness of the lateral explosive is a linear distribution from one side to

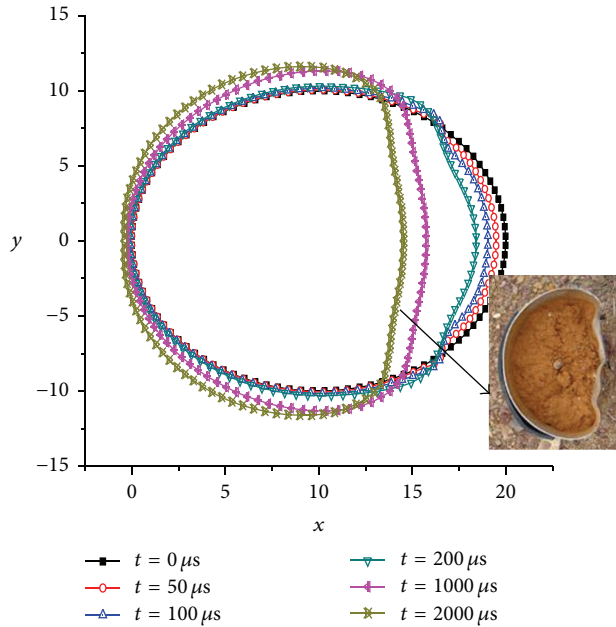


FIGURE 13: Distributions of positions and velocities of the cylindrical shell at different moments ($v(\alpha) = v_0 \cos \alpha$).

middle position, and the thickness of one side is a half of middle position.

Due to the explosive mass reduction, the initial velocities close to the lateral charge are assumed to have a cosine distribution. Figure 13 illustrates distribution of positions and velocities of the cylindrical shell at five classical times under the covered width 90° and the initial velocities having a cosine distribution.

The plotted data in Figures 8–13 are from mathematical modeling, including deformation process, different covered width, and initial velocity, where there are several results compared with the experimental results. For example, in Figure 8, the deformation shape remains stationary at 2000 microsecond moment, which is in good agreement with the experimental results. From the calculated results of the velocity distributions of the ring, the velocity of each discrete bar is zero almost at 2000 microsecond moment, so it can represent the experimental result.

6. Conclusions

This paper presents brief results of an experimental investigation on the deformation process of the cylindrical shell with internal medium under lateral contact explosion, and the deformation shapes were obtained. Based on the experiments, a corresponding analytical approach has been undertaken using the rigid plastic hinge theory.

Given the structural parameters and explosive charge, deformation processes and shapes are reported using the analytical approach. A good agreement has been obtained between calculated and experimental results, and thus the analytical approach can be considered as a valuable tool in understanding the deformation mechanism and predicting

the deformation shapes of the cylindrical shell with internal medium subjected to lateral contact explosion. Finally, a parametric study is carried out to analyze the effects of deformation shapes, depending on the covered width of the lateral explosive, explosive materials, and distribution of initial velocities. Therefore, an optimal deformation shape can be achieved by adjusting the covered width of lateral and initial velocities distribution.

Conflict of Interests

The authors declare that there is no conflict of interests regarding the publication of this paper.

Acknowledgment

The authors wish to acknowledge, with thanks, the financial support from the China National Natural Science Funding under Grants nos. 11202237 and 11132012.

References

- [1] V. Hadavi, J. Z. Ashani, and A. Mozaffari, "Theoretical calculation of the maximum radial deformation of a cylindrical shell under explosive forming by a new energy approach," *Proceedings of the Institution of Mechanical Engineers Part C: Journal of Mechanical Engineering Science*, vol. 226, no. 3, pp. 576–584, 2012.
- [2] R. G. Yakupov, "Plastic strains in a cylindrical shell under the effect of a spherical blast wave," *Strength of Materials*, vol. 14, no. 1, pp. 52–56, 1982.
- [3] R. G. Yakupov, "Plastic deformations of a cylindrical shell under the action of a planar explosion wave," *Journal of Applied Mechanics and Technical Physics*, vol. 23, no. 4, pp. 579–584, 1982.
- [4] P. R. Gefken, S. W. Kirkpatrick, and B. S. Holmes, "Response of impulsively loaded cylindrical shells," *International Journal of Impact Engineering*, vol. 7, no. 2, pp. 213–227, 1988.
- [5] M. S. T. Fatt and T. Wierzbicki, "Damage of plastic cylinders under localized pressure loading," *International Journal of Mechanical Sciences*, vol. 33, no. 12, pp. 999–1016, 1991.
- [6] T. Wierzbicki and M. S. H. Fatt, "Damage assessment of cylinders due to impact and explosive loading," *International Journal of Impact Engineering*, vol. 13, no. 2, pp. 215–241, 1993.
- [7] J. Jiang and M. D. Olson, "Nonlinear dynamic analysis of blast loaded cylindrical shell structures," *Computers & Structures*, vol. 41, no. 1, pp. 41–52, 1991.
- [8] Q. M. Li and N. Jones, "Blast loading of a 'short' cylindrical shell with transverse shear effects," *International Journal of Impact Engineering*, vol. 16, no. 2, pp. 331–353, 1995.
- [9] C. Pédrón and A. Combesure, "Dynamic buckling of stiffened cylindrical shells of revolution under a transient lateral pressure shock wave," *Thin-Walled Structures*, vol. 23, no. 1–4, pp. 85–105, 1995.
- [10] R. Rajendran and J. M. Lee, "A comparative damage study of air- and water-backed plates subjected to non-contact underwater explosion," *International Journal of Modern Physics B*, vol. 22, no. 9–11, pp. 1311–1318, 2008.

- [11] C. F. Hung, B. J. Lin, J. J. Hwang-Fuu, and P. Y. Hsu, "Dynamic response of cylindrical shell structures subjected to underwater explosion," *Ocean Engineering*, vol. 36, no. 8, pp. 564–577, 2009.
- [12] J. Li and J.-L. Rong, "Experimental and numerical investigation of the dynamic response of structures subjected to underwater explosion," *European Journal of Mechanics B/Fluids*, vol. 32, no. 1, pp. 59–69, 2012.
- [13] L.-J. Li, W.-K. Jiang, and Y.-H. Ai, "Experimental study on deformation and shock damage of cylindrical shell structures subjected to underwater explosion," *Proceedings of the Institution of Mechanical Engineers Part C: Journal of Mechanical Engineering Science*, vol. 224, no. 11, pp. 2505–2514, 2010.
- [14] G. Y. Hu, G. Xia, and J. Li, "The transient responses of two-layered cylindrical shells attacked by underwater explosive shock waves," *Composite Structures*, vol. 92, no. 7, pp. 1551–1560, 2010.
- [15] X.-L. Yao, J. Guo, L.-H. Feng, and A.-M. Zhang, "Comparability research on impulsive response of double stiffened cylindrical shells subjected to underwater explosion," *International Journal of Impact Engineering*, vol. 36, no. 5, pp. 754–762, 2009.
- [16] H. H. Jama, G. N. Nurick, M. R. Bambach, R. H. Grzebieta, and X. L. Zhao, "Steel square hollow sections subjected to transverse blast loads," *Thin-Walled Structures*, vol. 53, pp. 109–122, 2012.
- [17] M. A. Meyer, *Dynamic Behavior of Materials*, John Wiley & Son, New York, NY, USA, 1994.

Research Article

Damage Analysis and Evaluation of High Strength Concrete Frame Based on Deformation-Energy Damage Model

Huang-bin Lin,¹ Shou-gao Tang,¹ and Cheng Lan²

¹*School of Aerospace Engineering and Applied Mechanics, Tongji University, Shanghai 200092, China*

²*Bolina Ingegneria S.R.L., Mestre, 30173 Venice, Italy*

Correspondence should be addressed to Huang-bin Lin; 1110448@tongji.edu.cn

Received 18 August 2014; Accepted 24 November 2014

Academic Editor: Yuri Petryna

Copyright © 2015 Huang-bin Lin et al. This is an open access article distributed under the Creative Commons Attribution License, which permits unrestricted use, distribution, and reproduction in any medium, provided the original work is properly cited.

A new method of characterizing the damage of high strength concrete structures is presented, which is based on the deformation energy double parameters damage model and incorporates both of the main forms of damage by earthquakes: first time damage beyond destruction and energy consumption. Firstly, test data of high strength reinforced concrete (RC) columns were evaluated. Then, the relationship between stiffness degradation, strength degradation, and ductility performance was obtained. And an expression for damage in terms of model parameters was determined, as well as the critical input data for the restoring force model to be used in analytical damage evaluation. Experimentally, the unloading stiffness was found to be related to the cycle number. Then, a correction for this changing was applied to better describe the unloading phenomenon and compensate for the shortcomings of structure elastic-plastic time history analysis. The above algorithm was embedded into an IDARC program. Finally, a case study of high strength RC multistory frames was presented. Under various seismic wave inputs, the structural damages were predicted. The damage model and correction algorithm of stiffness unloading were proved to be suitable and applicable in engineering design and damage evaluation of a high strength concrete structure.

1. Introduction

Structural concrete is a material with quite outstanding cumulative damage characteristics; however, damage development and damage accumulation under different conditions are fundamental for understanding structural failure. Seismic damage greatly influences the bearing capacity of a building or structure during the follow-up service period and remaining life. Structural damage and its accumulation occur under dynamic loading, and a reasonable damage model must be constructed so that the damage can be described.

The structure damage caused by earthquakes is closely related to the maximum structural deformation and the low cycle fatigue effect caused by the accumulation of damage. In this paper, we have adopted a model based on two major forms of seismic damage [1]: (1) damage which occurs the first time the structure is taken beyond initial cracking and (2) damage due to subsequent energy dissipation. These forms

of damage are incorporated into a double parameter damage model based on deformation and energy dissipation.

In this paper, we use the stiffness degradation trilinear model (DT3 model, Figure 1). The DT3 model uses three lines to describe the loading and restoring force skeleton curve and considers the stiffness degradation properties of the reinforced concrete structure or structural component. The model can describe in more detail the real restoring force curve of a reinforced concrete structure. Depending on whether a particular structure or structural member is expected to harden after yielding, the curve is divided into two parts—one part using the maximum top hardening degradation from the trilinear model, while the other part without this consideration. The degradation trilinear model, as used in this paper, is widely applied in engineering projects.

For these structures, the elastic-plastic time history analyses of the structure are carried out in order to determine the effect of accumulated damage on performance. Since

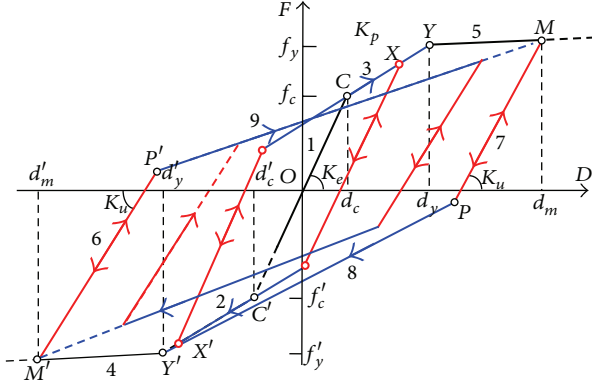


FIGURE 1: Degrading trilinear model (DT3).

the relationship between the unloading stiffness and ductility coefficient is also unknown, IDARC [2] analysis is introduced in this paper (Scheme 1).

2. Parameter Determination for Deformation-Energy Damage Model of High Strength Concrete

2.1. Model for Deformation-Energy Consumption Damage. We chose the Park and Ang's double parameters damage model for this paper [1]. This model is based on the test results of 261 groups of reinforced concrete. The seismic damage is modeled via using a double parameter combination of the maximum deformation and cumulative hysteresis energy dissipation, and expressed as

$$D = \frac{\delta_m}{\delta_u} + \frac{\beta}{\delta_u Q_y} \int dE, \quad (1)$$

$$D = \frac{\delta_m}{\delta_u} + \beta \int \left(\frac{\delta}{\delta_u} \right)^\alpha \frac{dE}{E_c(\delta)}. \quad (2)$$

δ_u is ultimate deformation under monotonic loading; δ_m is maximum deformation under earthquake; Q_y is calculated yield strength (if Q_u is smaller than Q_y , $Q_y = Q_u$); dE is incremental absorbed hysteretic energy, and α , β are nonnegative parameters. Under elastic response, the value of D should theoretically be zero; $D \geq 1.0$ signifies complete collapse or total damage.

Park and Ang represented the effect of cyclic loading on structural damage by the parameter β . The absorbed hysteretic energy (excluding potential energy) was integrated up to the failure point for 261 groups of cyclic test data from columns and beams. Only those in which a sudden failure was clearly observed or gradual failure could be identified from the envelope curve were included.

When calculating the damage index, the load-deformation curve for each test is traced up to the failure point; at the point of failure ($D = 1$), the corresponding value of β is evaluated. In fact, these β values also depend on the value of local plastic rotation supply and the concrete strengths beyond. Based on the calculated β values [1], a negative

correlation was observed between β and the confinement ratio, ρ_w , and weak positive correlations were observed between β and the shear span ratio, l/d , longitudinal steel ratio, ρ_l , and axial stress, n_0 . Consider

$$\beta = \left(-0.447 + 0.73 \frac{l}{d} + 0.24n_0 + 0.314\rho_l \right) \times 0.7^{\rho_w}, \quad (3)$$

$$\beta = \left(-0.165 + 0.0315 \frac{l}{d} + 0.131\rho_l \right) \times 0.84^{\rho_w}. \quad (4)$$

In which, l/d is shear span ratio (replaced by 1.7 if $l/d < 1.7$); n_0 is normalized axial stress (replaced by 0.2 if $n_0 < 0.2$); ρ_l is longitudinal steel ratio as a percentage (replaced by 0.75% if $\rho_l < 0.75\%$); and ρ_w : confinement ratio, (replaced by 2.0% if $\rho_w > 2.0\%$). Table 1 shows the correlation between β values from the model and the extent of damage.

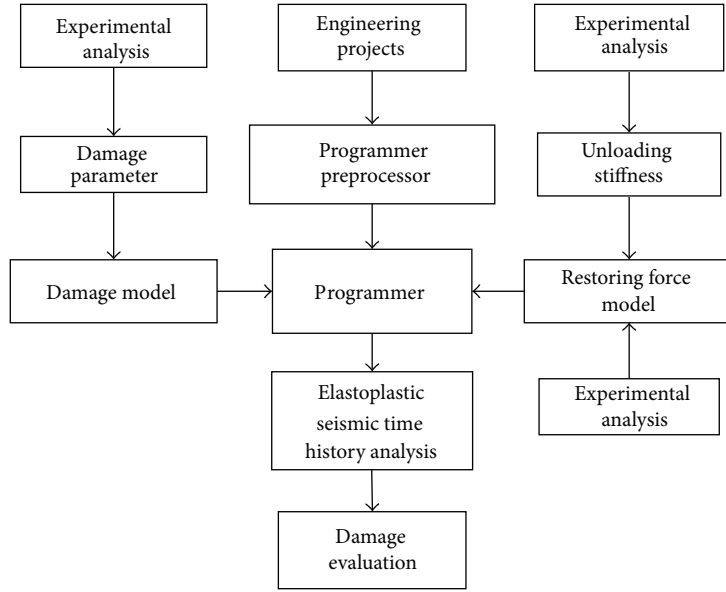
2.2. Serviceable Range of Double Parameters Damage Model. Park and Ang proposed their model based on a large number of test data, covering the following range of parameters: $1.0 < l/d < 6.6$; $0.2 < \rho_w < 2.0$; $0 < n_0 < 0.52$; $15.84 \text{ N/mm}^2 < f'_c < 41.34 \text{ N/mm}^2$; and $0.04 < \rho_l < 0.45$. They used standard compressive tests with cylindrical samples (150 mm in diameter, 300 mm high) to determine the compressive strength and the failure strength. Beolchini et al. [3], taking test data for concrete columns under repeated loading cycles, believe that the value of β depends on ρ_w , ρ_l , $\lambda = l/d$ (shear span), and $N/f_c A_C = n_0$ (axial compression ratio) as given in the following expression:

$$\beta = (-0.28 + 0.06\lambda + 0.47n_0 + 0.19\rho_l) \times 0.66^{\rho_w}. \quad (5)$$

More recently, high strength concrete ($f'_c > 41.34 \text{ N/mm}^2$) has been widely used in engineering; such concrete is beyond the strength range of Park and Ang's model. So, the parameters for the damage model expression of high strength concrete must be adapted. These parameters can then be assessed to determine the damage mechanism, and an appropriate extension created for the damage calculation program.

Relevant tests of high strength concrete columns have been performed by authors, including component design, seismic tests, design of loading devices, and evaluation of the test data to determine the loading mechanism, failure mode, $P - \Delta$ curve, ductility coefficient, and yield displacement. The tests data are presented in reference [4]. Ductility is an important indicator of high strength, constrained, concrete. The comparison between component stiffness degradation, strength degradation, and ductility is shown in Figures 2 and 3.

2.3. Calculating Coefficient of Cyclic Loading Effect β . Defining β_1 as that calculated using formula (3) and β_2 as that calculated using formula (5), failure points can be obtained from $P - \Delta$ curves of each test extrapolating to the damage point, $D = 1$. Then, values of the damage parameter β_3 can then be calculated; see Table 2. Then, the comparison of parameters β_1 , β_2 , and β_3 for a variety of values of beam



SCHEME 1: Programming flowchart.

TABLE 1: Damage evaluation rules from Park and Ang model based on value of β .

| Damage model | Intact | Slight damage | Medium damage | Serious damage | Collapsed |
|--------------------|--------|---|---------------|--|-----------|
| Park and Ang model | | 0–0.4 (damage which can be repaired) | | 0.4–1.0 (damage which cannot be repaired) | >1.0 |

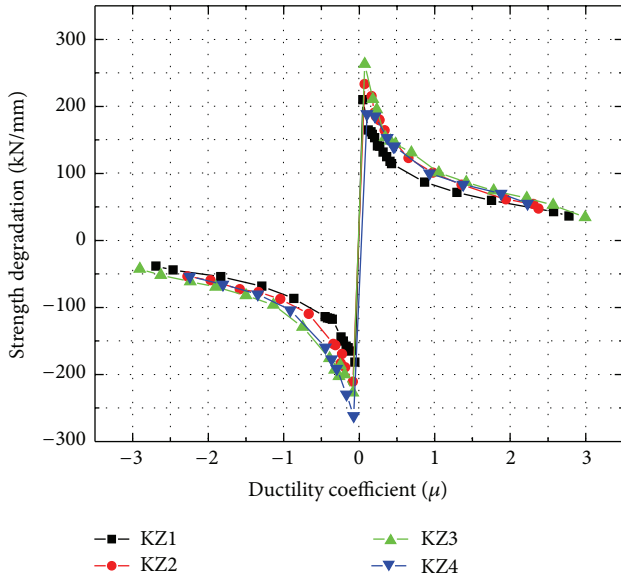


FIGURE 2: Relationship between stiffness degradation and ductility coefficient.

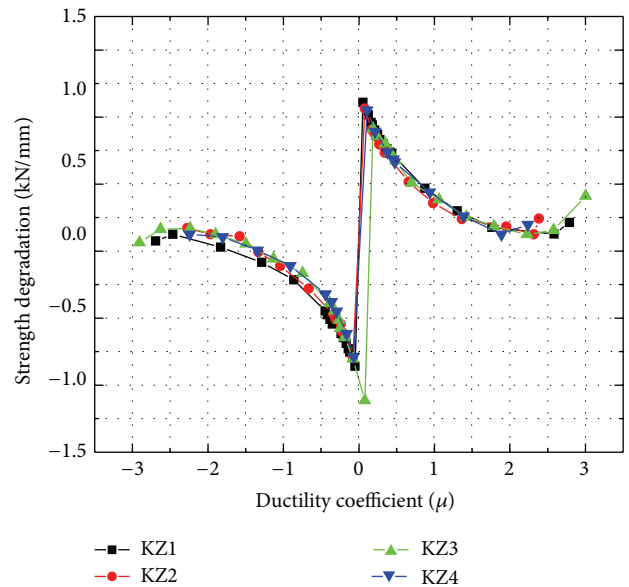


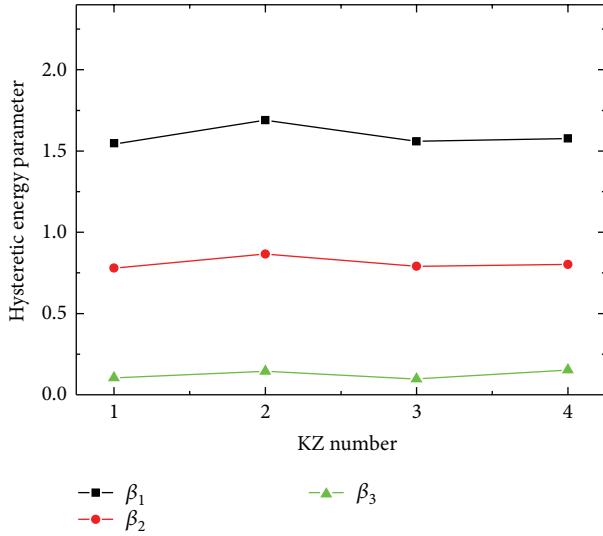
FIGURE 3: Relationship between strength degradation and ductility coefficient.

stiffness coefficient, KZ, is shown in Figure 4. The trends in the theoretical values (β_1, β_2) and the experimental regression value (β_3) are consistent. However, formulas (3) and (5) do not adequately consider the effect of the greater strength of high strength concrete; the influence of the concrete strength grade on the component ductility and energy consumption

is quite significant. Component tests are therefore necessary for determining the appropriate parameters for high strength concrete. Table 2 shows the parameters obtained by fitting the expression $\beta(\lambda, n, \rho_l, \rho_w)$ for high strength concrete columns in the following procedure: (1) calculate formula (1) using β_1 evaluated from formula (3); (2) calculate formula (2) using

TABLE 2: Calculation of β (parameter of damage model for cyclic loading).

| Specimen | δ_u mm | Q_y kN | δ_m mm | $\int dE$ kN·mm | $Q_y \delta_u$ kN·mm | β_3 | Double parameters damage model | Modified model |
|----------|------------------|-------------|------------------|--------------------|-------------------------|-----------|--------------------------------|----------------|
| TS-1 | 6.51 | 223 | 2.74 | 8292.0 | 1451.73 | 0.104 | 6.994 | 0.941 |
| TS-2 | 6.25 | 236 | 2.41 | 6053.0 | 1475 | 0.144 | 10.028 | 0.929 |
| TS-3 | 6.25 | 269 | 2.43 | 9619.0 | 1681.25 | 0.101 | 9.857 | 0.950 |
| TS-4 | 5.62 | 241 | 2.18 | 5120.0 | 1354.42 | 0.153 | 6.625 | 0.912 |

FIGURE 4: Comparison of values of β (parameter of damage model) obtained with different models.

β_2 evaluated from formula (5); (3) extrapolate each test curve to the failure point, and finally (4) determine the value at the damage point. The intermediate calculations are given in Table 2. Consider

$$\beta = \left(-0.447 + 0.73 \frac{l}{d} + 0.24n_0 + 0.314\rho_l \right)^\gamma \times 0.7^{\rho_w}. \quad (6)$$

Formula (6) was used to calculate modified parameters for the deformation-energy damage model. These parameters were then used in the evaluation of testing member, and the new damage index was obtained, as shown in Table 2. The experimentally observed parameters—structural member ruptures, yield, and the final state—correlated well with the damage index. The damage index is close to 1 when the structure fails. The observed phenomena during the tests corresponded well with the predictions from the damage index. While, Park and Ang's model damage index at failure had a value more than 1.0.

2.4. Skeleton Curve of High Strength Concrete. Through research on the restoring force model of high strength reinforced concrete columns, we have established a restoring force model which can adequately explain the nonlinear characteristics, using the principle of simplified calculation, in addition to considering the hysteresis characteristics of component, using the degrading trilinear model (Figure 1).

The route and hysteresis movement of the component can be described from the figure by tracing around the figure in the following sequence: $O \rightarrow C \rightarrow C' \rightarrow X \rightarrow X' \rightarrow \dots \rightarrow M \rightarrow P \rightarrow M' \rightarrow P'$. The OC section represents the elastic behavior, the CXY section is the strengthening, YM is degradation, $C'X'Y'$ is the reverse strengthening period, and $Y'M'$ is the reverse degradation period.

The data at key points on the skeleton curve were determined experimentally and then used to initialize an analysis program that is implemented in IDARC.

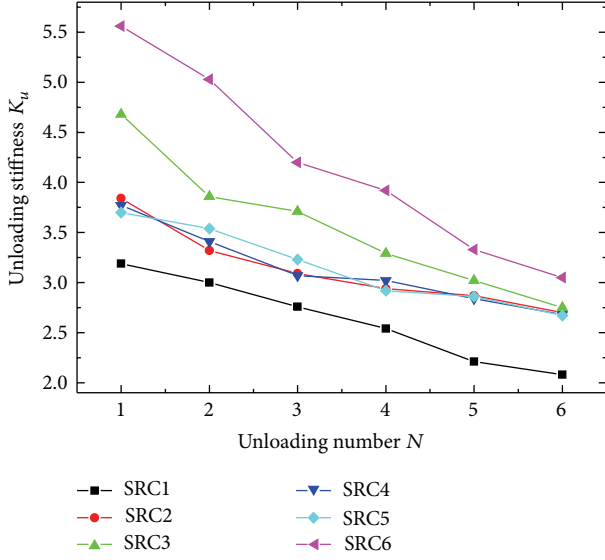
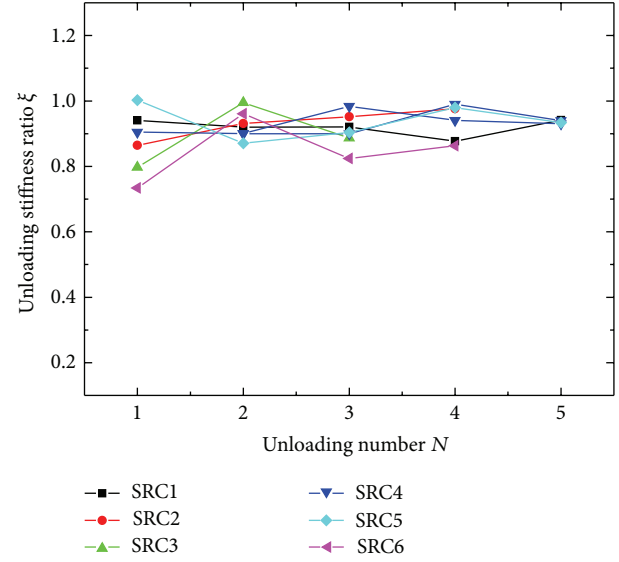
3. High Strength Reinforced Concrete Unloading Rigidity and Ductility Coefficient

3.1. Elastic Principle of Dynamic Unloading Stiffness. The IDARC program for structural damage analysis had been used to simulate the earthquake response of a frame structure collocated with a high strength concrete column. To better simulate the dynamic performance of a high strength concrete structure, the dependency of the unloading stiffness and ductility coefficient is analyzed after being introduced into the IDARC program. Loading and unloading standards can be expressed as follows: loading $(\partial\varphi/\partial\varepsilon_{ij})d\varepsilon_{ij} > 0$; neutral loading $(\partial\varphi/\partial\varepsilon_{ij})d\varepsilon_{ij} = 0$; unloading $(\partial\varphi/\partial\varepsilon_{ij})d\varepsilon_{ij} < 0$ ($\varphi = 0$).

Unloading during structural vibration is complicated, as structure unloading stiffness matrix changes with time, leading to a time varying parameter system. At present, structure elastic-plastic time history analysis generally does not consider the influences that the unloading stiffness and motion state have on each other. These influences mean that the dynamic equations represented by tangent stiffness and secant stiffness are not equivalent, as the matrix is constantly changing during this process.

From the deformation properties and the restoring force model tests of high strength concrete columns, Figure 5 shows the relationship between the structural member stiffness and number of unloading cycles; it indicates that the variation of $K_u(x)$ shows changes consistent with linear drag. The unloading stiffness K_u of for all samples changes with cycling, implying that the system is not fully elastic. The most important feature is that $dK_u(x)$ is approximately constant, although it varies from sample to sample.

3.2. Unloading Stiffness Correction Coefficient. The unloading stiffness degradation used to determine the damage index conforms to observed evolution of structure damage. As the cyclic stress presenting in structural member, the strain ε can


 FIGURE 5: Measured K_u and unloading number.

 FIGURE 6: Measured ξ and unloading number.

be divided into reversible strain ε_e and irreversible strain ε' and ε' includes the plastic strain ε_p and the residual strain due to unrecoverable damage, ε_u . From the principle of damage,

$$\sigma = E(1 - \nu D)\varepsilon_e = E(1 - \nu D)\Delta_e. \quad (7)$$

In formula (7), destruction of the member is defined as $D = 1$. For the damage model, D , we have used the deformation-energy double parameter combination; ν is only taken into account by the combination of factors of the maximum displacement damage coefficient ($0.5 \leq \nu < 1.0$). According to independent state variables principle in thermomechanics, the $P - \Delta$ state during damage evolution can be expressed as

$$F = K_0(1 - \nu D)\Delta_e = K_0(1 - \nu D)(\Delta - \Delta_p - \Delta_u),$$

$$\nu D = 1 - \frac{F}{K_0(\Delta - \Delta_p - \Delta_u)} = 1 - \frac{K_u(x)}{K_0}. \quad (8)$$

Formula (8) implies that using unloading stiffness $K_u(x)$ to describe the structure damage value D is feasible. For ductile members ($2.0 < \mu < 4.0$), assuming that the damage function $D = f_D(x_1, x_2, \dots, x_n)$ is a monotonically increasing function, we can obtain the following from formula (8):

$$K_u(x) = [1 - \nu f_D(x_1, x_2, \dots, x_n)]K_0, \quad (9)$$

where for the i th cycle, unloading stiffness is K_{u_i} and elastic stiffness ratio is η_i . At cycle $(i + 1)$, the unloading stiffness is $K_{u_{i+1}}$ and elastic stiffness ratio is η_{i+1} . ξ is defined as the ratio for the i th and $(i + 1)$ th cycles:

$$\xi = \frac{\eta_{i+1}}{\eta_i}. \quad (10)$$

Figure 6 charts the relationship between the measured value ξ and cycle number, N . The value of ξ remained steady

between $0.85 \leq \xi \leq 0.95$, implying that this parameter can be fixed during modeling; we suggest $\xi = 0.9$ for HSC. The test specimens reflect the phenomenon of degeneration of unloading stiffness with increasing displacement amplitude and can explain the fact that for an actual component the response excursion is always larger in one direction (i.e., offset), and eventually the accumulated errors as a result of this can lead to computational instability. Dynamic adjustment of unloading stiffness is simple but practically important.

4. Damage Evaluation of Highly Confined Concrete Structure Damage Evaluation Based on IDARC

4.1. Design Information of High Column Structure. In this paper, we model a structure comprising a six-floor frame of cast-in-situ high strength reinforced concrete. The strength grades of the concrete beams are C60–C80 and the main reinforcement and lateral reinforcement are HRB400 (f_y), where the effects on structure ductility while utilizing HRB400 as reinforcement in high strength concrete have been studied to be limited under certain conditions [5, 6]. The columns use symmetric steel reinforcement, the cover thickness is 30 mm, and the gravitational load of each floor is: $G_1 = 6800$ kN, $G_2 = G_3 = G_4 = G_5 = G_6 = 6600$ kN. The earthquake intensity is at level VIII (Liedu scale, CSIS). According to the structure facade height, earthquake intensity, and design ground acceleration, the seismic design parameters are design grade 2, site category II, and design group 1 (feature period $T_g = 0.35$ s). Therefore, the average material strength of the high strength concrete is necessary to consider the dynamic response characteristics (including the restoring force) of the structural members; as the natural period of structure is $T_1 = 0.49$ s, the design ground acceleration is 0.15 g.

The axial forces applied to each column in the structure are computed by elastic analysis. This paper adopts two indices to characterize the wave, the design characteristic period of site structure T_g , and structure basic natural period T_1 . To choose the earthquake duration and natural period for the model, we have selected two strong earthquake records P0151 and P0994 from the PEER Strong Motion Database [7], the EL Centro wave (Figure 7) which is widely used in engineering, and also the RH4TG040 artificial seismic wave, ThiTG040 natural seismic wave, and TH2TG040 natural seismic wave from the EPDA module [8].

4.2. Damage Programming. IDARC is from the Earthquake Engineering Research Centre of the State University of New York at Buffalo and is widely used for various types of nonlinear dynamic response time history analysis and damage analysis of structures. Details of our IDARC analysis will be given below.

(1) Hysteretic Rules Model. The program provides a three-parameter Park's model, bilinear hysteretic model, Kelvin's model, Maxwell's model, and smooth hysteretic model. For this paper, we have chosen a three-line attenuation model created by authors; all control information required by the preprocessor is obtained from the experimental skeleton curve.

(2) Nonlinear Dynamic Analysis. Nonlinear dynamic analysis is carried out using a combination of the Newmark-beta integration method, and the pseudoforce method. The equation is solved numerically, according to

$$\begin{aligned} [M] \{\Delta\ddot{u}\} + [C] \{\Delta\dot{u}\} + [K_t] \{\Delta u\} \\ = -[M] \left(\{L_h\} \Delta\ddot{x}_{gh} + \{L_v\} \Delta\ddot{x}_{gv} \right) - \{\Delta P_{TW}\} \quad (11) \\ + c_{\text{corr}} \{\Delta F_{\text{err}}\}, \end{aligned}$$

where $[M]$ is the lumped mass matrix of the structure; $[C]$ is the viscous matrix of the structure; $[K_t]$ is the tangent stiffness matrix; $\{\Delta u\}$, $\{\Delta\dot{u}\}$, and $\{\Delta\ddot{u}\}$ are the incremental vectors for displacement, velocity, and acceleration in the structure; $\{L_h\}$ and $\{L_v\}$ are the allocation vectors for the horizontal and vertical ground accelerations; $\Delta\ddot{x}_{gh}$ and $\Delta\ddot{x}_{gv}$ are the increments in the horizontal and vertical ground accelerations; c_{corr} is a correction coefficient; and $\{\Delta F_{\text{err}}\}$ is the vector containing the unbalanced forces in the structure. At the end of step $t + \Delta t$, the difference between the restoring force calculated using the hysteretic mode $\{R\}$ and the restoring force considering no change in stiffness during the step $\{R'\}$ yields the residual force $\{\Delta F_{\text{err}}\} = \{R\} - \{R'\}$.

This corrective force is then applied for the next time step of the analysis. The unbalanced forces are computed when moments, shears, and stiffness are being updated in the hysteretic model. We selected a step length of 0.02 seconds, to produce smaller changes at each step and thus avoid larger residual forces, which could lead to unstable calculations.

(3) Damage Index. IDARC incorporates three models for damage index, (a) classical Park-Ang's model; (b) a model based on low cycle fatigue damage characteristics; and (c)

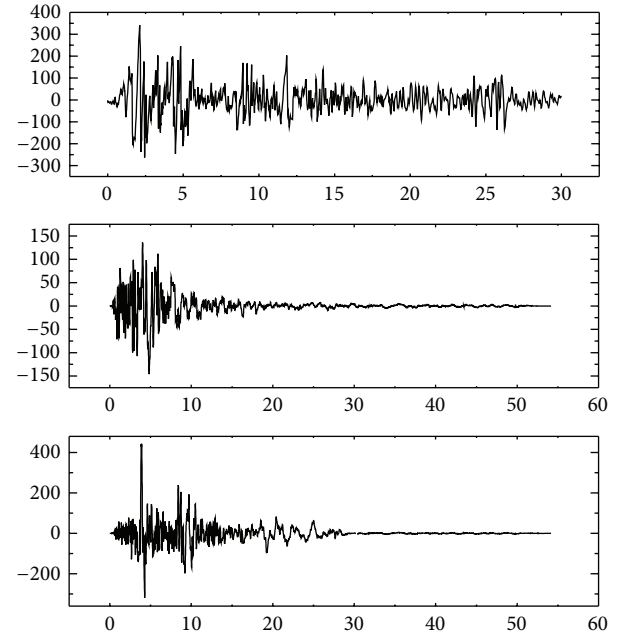


FIGURE 7: El Centro, P0151 and P0994 seismic waves.

according to the structural basic cycle for the overall structure damage index. This paper used the modified double parameters damage index and calculated the indices using the embedded computing methods (a), (b), and (c) for comparison.

4.3. Structural Nonlinear Dynamic Analysis Results

4.3.1. The Maximal Displacement and Angular Displacement between Floors. This paper selects high strength RC structures as an example to investigate dynamic analysis, study the seismic performance, and evaluate the degree of damage. Under seismic action (3 waves of structure PEER ground motion, 2 waves of EPDA ground motion, 1 wave of artificial seismic wave and the SATWE program), the maximum displacement of each floor and the maximum angular displacement between the floors are shown in Figure 8. For different input seismic waves, the trends in the maximum displacements and angular displacements of floors are consistent. It suggests that the damage assessment program is reliable. The maximum angular displacements appeared in floor 3 and floor 2, and the angular displacement exceeds the limit of 0.02 by code, but no obvious weak floors are observed.

4.3.2. Plastic Hinge Law and Damage Distribution. The implemented program provides the structural damage index and plastic hinge distribution for each seismic wave. The structural plastic hinge distribution and sequence of their appearances under earthquake ground motion PEER are shown in Figure 9, and the profile of the damage distribution is in Figure 10. The behavior of the structural damage distribution and structure plastic hinge distribution are almost identical. A greater damage index means that the members

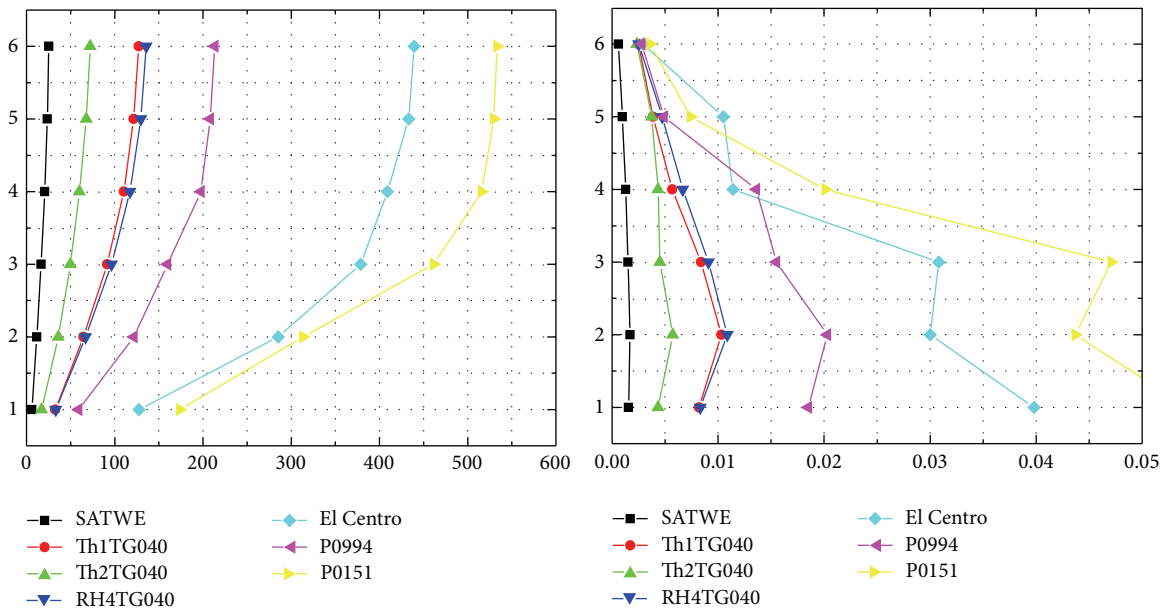
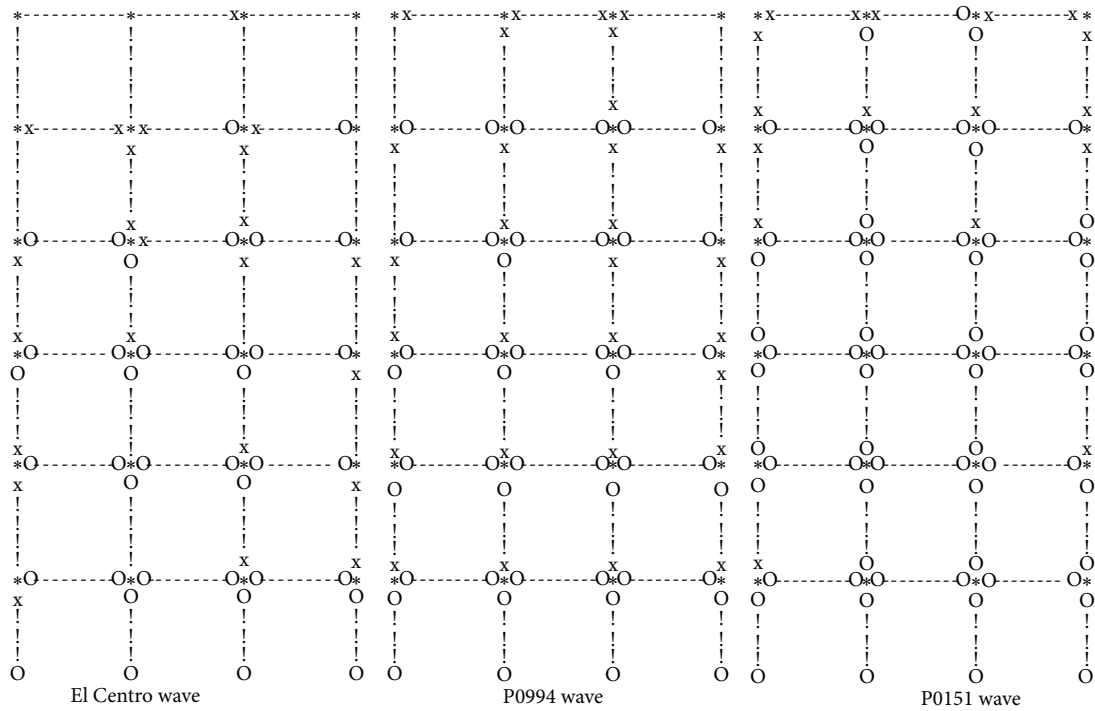


FIGURE 8: Maximum floor displacement and story drift angle of building in seismicity basic intensity 8 area.



Final state of frame
 - Beam
 ! Column
 x Cracking
 O Plastic hinge developed
 * Local failure (exceed criteria)

FIGURE 9: Plastic hinge distribution of building.

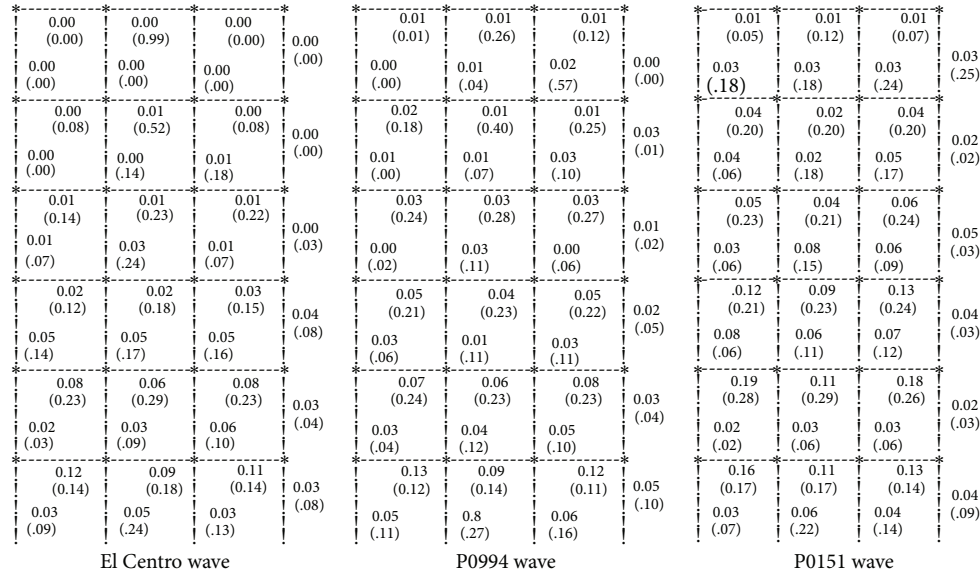


FIGURE 10: Damage index statistics of frame.

yield earlier and the plastic rotation is larger and vice versa. The damage to columns is light, the damage level of most columns is “medium destruction,” and the performance of the high-performance concrete is satisfactory. While the damage in the beams is much serious, the distribution of the damage index reflects the seismic design principle of “strong column, weak beam”. Apart from the top floor, all beam ends act as plastic hinges, whilst only the column bottoms and a few centers of columns show hinge behavior. The beams act as hinges earlier than columns, nearly forming an overall symmetrical beam hinge system. The structure performance measured by the quantitative damage index is more reliable than displacement-based design.

The shear-displacement hysteresis curves for the bottom of the structure are shown in Figure 11. Qualitative analysis of the hysteric performance of each floor can be performed based on the lateral displacement-shear hysteresis relationships under the action of the shock wave. Preliminary analysis of the graphs shows that the bottom layer has yielded, and the extent of rigidity degradation shows that the first shock transcends beyond destruction and the maximum displacement appears only for a few seconds. Most of the time, the displacement is relatively small, and the plastic energy dissipation and cumulative plastic deformation are small.

4.3.3. Seismic Damage Analysis of Whole Structure. The modified parameter damage model was used to calculate damage parameters for all columns in each floor of the frame structure under the earthquake waves. The results are shown in Table 3. Both the results and value range of the modified damage model calculation are close to those observed in real damaged structures. Getting instantaneous snapshots from the program during time history analysis, we can calculate the instantaneous damage index for the whole structure as

a function of the time period. We find that for this example wave used the damage index is

$$DI = 1 - \frac{(T_0)_{\text{initial}}}{(T_0)_{\text{equivalent}}} = 1 - \frac{0.49}{1.410} = 0.652, \quad (12)$$

where $(T_0)_{\text{initial}}$ is the initial fundamental period and $(T_0)_{\text{equivalent}}$ is the equivalent fundamental period. The overall damage can reflect more accurately the reaction of the whole structure. This is probably because that, using the vibration frequency attenuation method (i.e., the change in stiffness with time), it accurately simulates the real behavior of structures. The results show that the high strength concrete frame had been damaged, but not up to the extent of complete collapse; it reaches the seismic design goal of not collapsing under a major earthquake. The presented algorithm results in a damage index always less than 1.0. This modified double parameters damage model is correctly describing the performance of damaged structures, because it predicts the results that are quite close to those observed in real damaged structures.

5. Conclusions

In this paper, based on the deformation-energy damage model and using experimental test data, we determined the expressions for the coefficient of the cyclic load effect and values required for the double parameter damage model of members of a high strength reinforced concrete column member. Ductility is the key index of high-performance concrete, as found by the analysis of the relationships between stiffness degradation, strength degradation, and ductility. A model of the restoring force was used; this model allowed extrapolation of the data to the point of failure to obtain

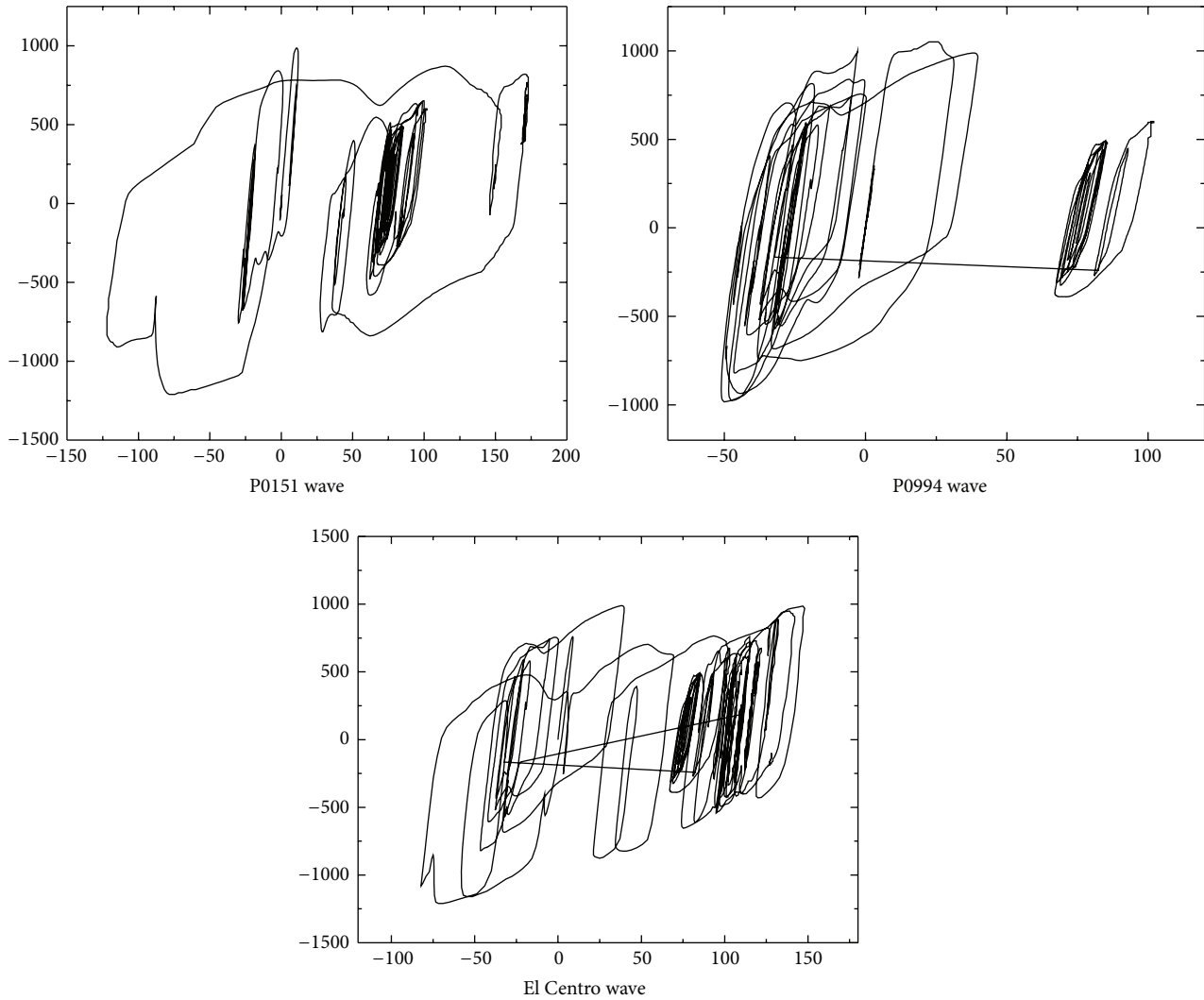


FIGURE 11: Base shear-drift hysteretic curve of building first floor.

the restoring force. A trilinear model was employed to describe damage.

Generally, the elastic-plastic time history analysis does not consider the relationship between unloading stiffness and motion state which influence each other. Thus, we evaluate the structure elastic-plastic time history analysis by introducing the unloading correction coefficient, which is a parameter that characterizes the change with time of the unloading stiffness matrix structure, and solve the equivalent problem between the structural dynamic equation indicated by tangential stiffness and secant stiffness. This gives a good description of the elastic-plastic structure vibration dynamic process, which can be used to describe the concrete structure unloading in the dynamic elastic-plastic state. We then implemented these modifications into the elastic-plastic time history analysis in IDARC program.

Presenting the case study of a high strength RC frame, the member dynamic response characteristics of the restoring force was calculated from the material average strengths,

where the longitudinal bar and stirrup bar were high strength bar and the concrete strength of the beam-column was high. The structural damages were observed under various seismic waves, including two strong artificial seismic wave records from the PEER library, the El Centro wave, two natural seismic waves, and one artificial seismic wave from EPDA. Dynamic analysis was used to analyze the seismic performance and evaluate the degree of damage. Under a strong earthquake, the maximum displacement and angular displacement between floors are consistent. The maximum angular displacement is more than limits by code, but there is no obvious weak floor; the damage to the base of the structure accumulates up until the maximum impact of reaction. The distribution of the damage index reflects the seismic design criterion of “strong column, weak beam,” nearly forming a symmetrical beam hinge system. The lateral-shear hysteresis curve is showing the yielding and the stiffness degradation degree. The displacements only appear to be exceeding initially and to be later small generally.

TABLE 3: Damage index of middle columns in each floor under seismic waves.

| Earthquake wave | | δ_u mm | F_y kN | δ_m mm | $\int dE$ kN·mm | IDARC | Modified damage model |
|-----------------|---|------------------|-------------|------------------|--------------------|-------|-----------------------|
| P | 1 | 173 | 362 | 102 | $4.07E + 04$ | 0.205 | 0.65 |
| 0 | 2 | 135 | 419 | 60.8 | $1.01E + 04$ | 0.181 | 0.77 |
| 1 | 3 | 124 | 111 | 44.7 | $1.62E + 04$ | 0.275 | 0.76 |
| 1 | 4 | 58.6 | 245 | 14.6 | $3.81E + 03$ | 0.198 | 0.79 |
| 5 | 5 | 27.8 | 191 | 19.6 | $1.12E + 03$ | 0.152 | 0.64 |
| | 6 | 140.1 | 404 | 65 | $3.33E + 02$ | 0.134 | 0.56 |
| P | 1 | 70.1 | 346 | 41.9 | $2.28E + 04$ | 0.081 | 0.5 |
| 0 | 2 | 73.1 | 373 | 43.3 | $2.12E + 03$ | 0.069 | 0.65 |
| 9 | 3 | 60 | 341 | 43.4 | $7.27E + 03$ | 0.131 | 0.65 |
| 9 | 4 | 45.1 | 245 | 29.4 | $3.19E + 03$ | 0.078 | 0.68 |
| 5 | 5 | 32.5 | 113 | 15.2 | $6.60E + 02$ | 0.06 | 0.48 |
| | 6 | 72.7 | 352 | 40.6 | $3.36E + 02$ | 0.05 | 0.47 |
| E | 1 | 148 | 276 | 69 | $2.54E + 04$ | 0.135 | 0.53 |
| L | 2 | 96.5 | 294 | 68.3 | $4.68E + 03$ | 0.11 | 0.73 |
| | 3 | 98.1 | 221 | 66.1 | $1.01E + 04$ | 0.162 | 0.7 |
| | 4 | 28.8 | 330 | 19.8 | $2.54E + 03$ | 0.1 | 0.71 |
| | 5 | 26.7 | 184 | 13.5 | $7.67E + 02$ | 0.085 | 0.53 |
| | 6 | 30.8 | 212 | 15.8 | $2.08E - 02$ | 0.081 | 0.53 |

To improve the calculation efficiency, the implementation of the modified damage model in IDARC program was developed and performed well for evaluating highly constrained high strength reinforced concrete structures. Comparison and further validation analysis and evaluation of damage with more software and programs will be done in future work, and more structural members data is necessary in evaluating the more precise correlation between damage model parameters and exact damage to structures.

Conflict of Interests

The authors of the paper declare that there is no conflict of interests regarding the publication of this paper. The authors do not have a direct financial relation with the commercial identity that might lead to a conflict of interests for any of the authors.

Acknowledgments

This work is supported by Natural Science Foundation of China (Grant no. 50578066), Natural Science Foundation of Fujian Province of China (Grant no. 2011J01320), and National Special Fund for the Territorial Resources in the Public Interest (no. 201111020-2). The authors sincerely thank them for their support and funding.

References

- [1] Y.-J. Park and A. H.-S. Ang, "Mechanistic seismic damage model for reinforced concrete," *Journal of Structural Engineering*, vol. 111, no. 4, pp. 722–739, 1985.
- [2] M. V. Sivaselvan, E. Yuksel, K. Winkelmann, and A. M. Reinhorn, "Transforming of an existing structural analysis program to the object-oriented framework," *Advances in Engineering Software*, vol. 40, no. 11, pp. 1131–1139, 2009.
- [3] G. C. Beolchini, D. Galeota, M. M. Giammatteo, and M. Zulli, *Seismic Behavior of High Strength RC Columns*, New Zealand Society for Earthquake Engineering, Auckland, New Zealand, 2000.
- [4] H. Lin and Q. Wang, "Seismic behavior on HRB400 high-strength reinforced concrete columns," *Journal of Building Structures*, vol. S1, no. 1, pp. 36–41, 2008.
- [5] K. Yang, Q. Shi, J. Zhao, W. Jiang, and H. Meng, "Study on the constitutive model of high-strength concrete confined by high-strength stirrups," *China Civil Engineering Journal*, vol. 46, no. 1, pp. 34–41, 2013.
- [6] Q. X. Shi, P. Wang, Y. Tian et al., "Experimental study on seismic behavior of high-strength concrete short columns confined with high-strength stirrup," *China Civil Engineering Journal*, no. 8, pp. 1–8, 2014.
- [7] BCUCO, *PEER Strong Motion Database*, 2014.
- [8] PKPM, *Multi-Layer and High-Rise Building Structure Elastic-Plastic Static/Dynamic Analysis Software Push& EPDA*, Chinese Architecture Industry Press, Beijing, China, 2012.

Research Article

Dynamic Characteristics of Electrostatically Actuated Microbeams with Slant Crack

Han Zhou, Wen-Ming Zhang, Zhi-Ke Peng, and Guang Meng

State Key Laboratory of Mechanical System and Vibration, School of Mechanical Engineering, Shanghai Jiao Tong University, 800 Dongchuan Road, Shanghai 200240, China

Correspondence should be addressed to Wen-Ming Zhang; wenmingz@sjtu.edu.cn

Received 14 September 2014; Accepted 18 December 2014

Academic Editor: Anaxagoras Elenas

Copyright © 2015 Han Zhou et al. This is an open access article distributed under the Creative Commons Attribution License, which permits unrestricted use, distribution, and reproduction in any medium, provided the original work is properly cited.

An improved model of the slant crack on a microbeam is presented. Based on fracture mechanics, the rotation coefficient for the slant crack is derived as a massless rotational spring accounting for the additional stress intensity factors generated by the orientation of the crack compared to the transverse crack. Comparisons between microbeams with a slant crack of different geometry parameters (slant angle, depth ratio, and crack position) are investigated with regard to the dynamic mechanical behaviors and nonlinear response. By presenting a mathematical modeling, the effects of the slant crack and the electric actuation of an electrostatically actuated fixed-fixed microbeam on the dynamic characteristics are examined in detail. It is shown that the crack position has more significant influence on the pull-in voltage value than the slant angle or the depth ratio. Approaching the slant crack to the fixed end or enlarging the external incentives amplifies the nonlinearity of the microbeam system, while the effects of depth ratio and slant angle are dependent on the crack position. The resonance frequency and the resonance amplitude are affected as well.

1. Introduction

With the advantages in miniaturizing reducing cost and energy consumption, the microelectromechanical systems (MEMS) are a growing industry finding their application in different fields such as resonators for sensing [1, 2] and electric filtering applications [3, 4]. Microbeams such as cantilever and doubly clamped beam are the major components of MEMS devices, and the preferred actuation method is always the electric actuation. In an electrostatically actuated microbeam, an air gap capacitor, composed of a movable microbeam (upper electrode) and a fixed (lower) electrode, is connected to a voltage source. This generates electric field and electrostatic force. The elastic force grows linearly with displacement, whereas the electrostatic force grows inversely proportional to the square of the distance when a potential difference is applied between the two electrodes. Consequently, the moveable beam deforms, and the displacement grows when the voltage is increased until at one point the growth rate of the electrostatic force exceeds than the elastic force. The system cannot reach a force balance without

a physical contact, and the pull-in instability occurs. This phenomenon is known as “pull-in,” and the critical voltage is the pull-in voltage. The reason for this phenomenon is the electrostatic force nonlinearity [5, 6].

In order to avoid or use the characteristic of the phenomenon, it is essential to study the pull-in. The pull-in instability is firstly found out in 1967 [7], and later Bernstein et al. [8] proved the existence of a bifurcation point at pull-in, where the microbeam deflection becomes unstable, and then Pelesko [9] proved the uniqueness property of the point. A review including the overview of the pull-in phenomenon in electrostatically actuated MEMS and NEMS devices and the physical principals of the pull-in instability provide a comprehensive understanding of the phenomenon [10]. In recent decades, different models have been developed to solve the pull-in problems, such as the nonlinear model of a beam including the electrostatic force, midplane stretching, and applied axial load [11, 12]. In the same time, different analytical numerical methods are improved, such as the shooting method [11], the differential quadrature method (DQM) [13],

and the combination of step-by-step linearization method (SSLM) and Galerkin-based reduced order model [6].

Another important problem generated during the machining process is the fatigue crack [14]. The existence of the crack was found to induce considerable local flexibility due to the strain energy concentration in the vicinity of the crack tip under load. Moreover, the crack will open or close in time depending on the loading conditions and vibration amplitude, which will change the dynamic characteristics. Eventually, the detection of the structural flaw can be available through measuring such changes. Moreover, a lot of analytical, numerical, and experimental investigations are reported now. Whether the crack is an open or a closed one depends on the combination of the static deflection of the cracked beam caused by some loading components such as the residual loads and the structure weights with the vibration effect. In detail, the crack remains open all the time, or it opens and closes regularly when the static deflection is larger than the vibration amplitudes. But if the static deflection is small, then the crack will open and close in time depending on the vibration amplitude. In these two cases, the former system is linear, while the latter one is nonlinear. So most of the researchers made the assumption that the crack in a structural element is open and remains open during vibration in their work, in order to avoid the complexities that resulted from the nonlinear characteristics presented by introducing a breathing crack (a crack which opens and closes during vibration) [15–17].

Many researchers are focused on developing suitable models to describe the effect of damage on the beam-like structures, and different approaches for crack modeling have been reported. The approaches can be generally divided into three categories [18]: spring models or elastic hinges [19], local stiffness reduction [20], and finite element models [21]. According to Friswell and Penny in [22], simple models of crack flexibility based on beam elements are adequate compared with other approaches, and those models belong to the category relying on the spring models. In particular, the model of crack as an internal hinge endowed with a rotational spring connecting the two adjacent beam segments is of high accuracy.

Based on that, the crack is modeled as an equivalent massless rotational spring with a local compliance, and this method was often used to quantify the relation between the applied load and the strain concentration around the tip of the crack in a macroscopic way [23, 24]. With improvement of the method in recent years, the crack is substituted by the additional local compliance of a cracked beam with relation to the strain energy concentration as well as to the stress intensity factor, and a lot of results both analytical and experimental are gained under different loading and geometry for a number of cases. Most researchers assumed the crack to be open but not close, which guaranteed a constant stiffness and frequency shift during vibration. Lin et al. [25] investigated the cracked beams model as a function of the crack depth as well as the consequently dynamic behaviors and the stability characteristics. Furthermore, Rubio and Fernández-Sáez studied the applicability of different approximate closed-form solutions to evaluate

the natural frequencies for bending vibrations of simply supported Euler–Bernoulli cracked beams [26]. Motallebi et al. [6] presented investigation of the effects of the geometry parameters, such as the crack depth, crack position, and the crack number, of open crack on the static and dynamic pull-in voltages of the microbeams under different support methods. Afshari and Inman presented results that the proposed crack modeling approach as a massless rotational spring was beneficial as it provided twice-differentiable mode shapes for the cracked beam and can be used as trial functions in the assumed mode approximations [27].

Since resonant sensors are important components in micromechanical devices, the investigations into the frequency response of a resonant microbeam to an electric actuation are of big significance [28]. As reported, frequency of a resonant microbeam is very sensitive to the axial strain induced by external loads, such as pressure, temperature, force, and acceleration, and consequently causes a shift in its natural frequencies. Such shift is generally converted to a digital signal related to the physical quantity being measured [29]. Additionally, some reports show that some other factors such as squeeze-film damping [30] and the elasticity of the microbeam supports can also originate the frequency shift [31]. Alsalem et al. [32] presented results of modeling, analysis and experimental investigation for nonlinear resonances, and the dynamic pull-in instability in electrostatically actuated resonators. Caddemi et al. [18] studied the nonlinear dynamic response of the Euler–Bernoulli beam in presence of multiple concentrated switching cracks (i.e., cracks that are either fully open or fully closed). Besides the transverse crack analyses, the dynamic characteristics of slant crack attract attention of researchers. But most such study is based on the vibrations analysis of rotors with slant crack, for example, [33, 34]. Little investigation of effect of slant crack on the dynamic response of microbeams is carried out.

In this paper, an improved model of beam with slant open crack is presented as a massless rotational spring. It is based on a continuous beam model and the stress and strain energy analysis of the vicinity of the crack. The combinatorial method of SSLM and Galerkin-based reduced order model is used to investigate the static response of MEMS devices, and the fixed-fixed beam model is applied. The natural frequencies and corresponding cracked mode shapes of the microbeam are calculated with the usage of the transfer matrix method under the boundary and patching conditions. And then the comparisons of the dynamic vibration behaviors and the pull-in voltages of beams with different geometry parameters of slant crack are shown. The effects of the crack depth, crack slant angle, and crack position on the dynamic vibration behaviors and the pull-in voltages are discussed. Finally, an investigation into the dynamic response of the microbeam is presented by using the multiple scales method, and the effects of the crack parameters and the electric actuation are discussed on the vibration nonlinearity.

2. Mathematical Modeling

Figure 1 shows the schematic of an electrostatically actuated fixed-fixed microbeam with a slant crack on the surface.

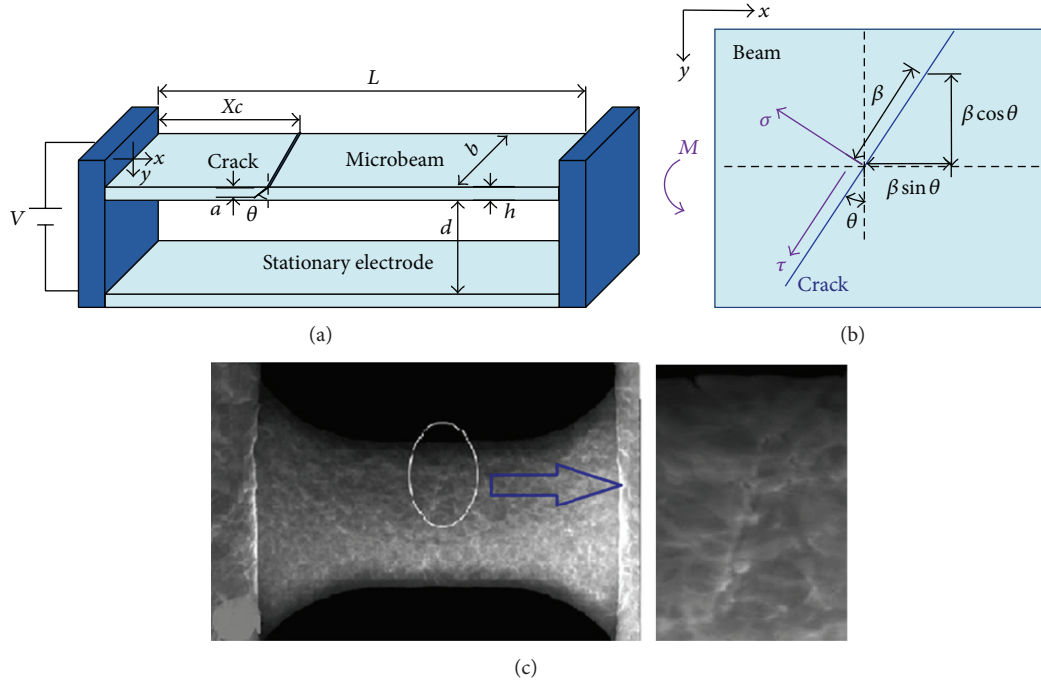


FIGURE 1: Schematic of a microbeam with a slant crack on the surface. (a) The mathematical modeling of an electrostatically actuated fixed-fixed microbeam with a slant crack. (b) Top view of stress components analysis of the microbeam loaded with a bending moment M . (c) Optical image of an actual beam specimen with a slant crack located at the center of a MEMS fatigue device and anchored to two lateral plates acting as electrostatic actuators [35].

The specimen is the small suspended fixed-fixed microbeam with a rectangular cross section located at the center of a MEMS device, which is fabricated using the gold electrodeposition technique [35]. The beam specimen is anchored to two lateral plates acting as electrostatic actuators (Figure 1(c)). When the plates are actuated, the beam structure deforms and undergoes a tensile load. The magnified section reveals the formation of intruded and extruded sections and the propagated crack. Figure 1(a) depicts the simplified mathematical modeling of the electrostatically actuated fixed-fixed microbeam, including a suspended elastic beam with an applied electrostatic force and another beam fixed at both ends to the ground conductor. The upper beam is suspended over a dielectric film deposited on top of the center conductor, which will be pulled down for the electrostatic force when a voltage is applied between the upper and lower electrodes. The microbeams are considered as Euler-Bernoulli beams of length L , width b , thickness h , density ρ , Young's modulus \bar{E} , Poisson's ratio ν , and $\bar{E} = \bar{E}/(1 - \nu^2)$. On the surface of the beam, an slant crack was located at point X_c , having a depth a oriented at an angle of θ relative to the normal direction of the beam, the depth ratio of $\gamma = a/h$. d and ε are initial gap and dielectric constant, respectively. \tilde{x} and $\tilde{w}(\tilde{x}, \tilde{t})$ denote the coordinate along the length of the microbeam with its origin at the left end and the transverse displacement of the beam, respectively. Now, the entire beam is divided into two parts with length of X_c and $L - X_c$, respectively [6], and the global nonlinear system can be separated into two linear subsystems joined by an additional local stiffness discontinuity. According to

the theory of fracture mechanics, the additional rotation coefficient can be derived from the strain energy release rate J and the strain energy U . For plane strain, the expression of J , U and the relation of them are [36, 37]

$$J = \frac{1}{\bar{E}} (K_I^2 + K_{II}^2 + (1 + \nu) K_{III}^2)$$

$$U = \iint_A J dA \quad (1)$$

$$\Theta = \frac{\partial U^2}{\partial P^2},$$

where A is the area of the crack. K_I , K_{II} , K_{III} represent the stress intensity factors (SIFs) corresponding to opening, sliding, and tearing mode of crack displacement, respectively. Θ is the additional rotation in the slope due to the existence of the crack, and P is the force loaded on the beam.

The SIFs are derived as follows. To simplify the problem, the slant-cracked beam is loaded with pure bending moment M . As shown in Figure 1(b), compared to a transverse crack, the bending M leads to more numbers of stress components responsible for the opening and tearing mode of crack displacement. The stress components include the shear stress τ and the normal stress σ , which cause tearing mode and opening mode of the crack, respectively. According to stress analysis [38], it can be gotten that

$$\sigma_0 = \frac{M}{I} \beta; \quad \tau_0 = 0; \quad \sigma_c = \sigma_0 \cos^2 \theta; \quad (2)$$

$$\tau_c = \sigma_0 \cos \theta \sin \theta,$$

where β is the distance from the centre point of the crack along the crack edge. σ_0 , τ_0 and σ_c , τ_c are the stress components in the transverse crack surface and the slant crack surface, respectively. And $I = 1/12bh^3$ is the inertia moment of microbeam cross section. To simplify the calculation, we take the largest stress, which means $\sigma_0 = 6M/bh^2$.

Then, SIFs for opening, sliding, and tearing mode can be expressed as

$$\begin{aligned} K_I^0 &= \sigma_0 \sqrt{\pi\alpha} F_2, & K_{II}^0 &= K_{III}^0 = 0; \\ K_I^c &= \sigma_c \sqrt{\pi\alpha} F_2, & K_{II}^c &= 0, & K_{III}^c &= \tau_c \sqrt{\pi\alpha} F_{III}, \end{aligned} \quad (3)$$

where K_I^0 , K_{II}^0 , and K_{III}^0 represent SIFs related to the transverse crack, while K_I^c , K_{II}^c , and K_{III}^c are related to the slant crack, and one has

$$\begin{aligned} F_2\left(\frac{a}{h}\right) &= \sqrt{\frac{2h}{\pi a} \tan\left(\frac{\pi a}{2h}\right)} \left(\frac{0.923 + 0.199 [1 - \sin(\pi a/2h)]^4}{\cos(\pi a/2h)} \right) \\ F_{III}\left(\frac{a}{h}\right) &= \sqrt{\frac{2h}{\pi a} \tan\left(\frac{\pi a}{2h}\right)}. \end{aligned} \quad (4)$$

With the expressions of SIFs derived above, synthesizing (1) to (3), adopting the correction function given by Anifantis and Dimarogonas and Taylor's series expansion [23], the nondimensional rotation expression is obtained as

$$\begin{aligned} \Theta &= 6\pi(1-v^2)\left(\frac{h}{L}\right) \left[\cos^3(\theta) f_1(\gamma) \right. \\ &\quad \left. + (1+v) \cos(\theta) \sin^2(\theta) f_2(\gamma) \right] \\ f_1(\gamma) &= 0.6348\gamma^2 - 1.035\gamma^3 + 3.7201\gamma^4 - 5.1773\gamma^5 \\ &\quad + 7.553\gamma^6 - 7.332\gamma^7 + 2.4909\gamma^8 \\ f_2(\gamma) &= 0.2026\gamma^2 + 0.03378\gamma^4 + 0.009006\gamma^6 + 0.002734\gamma^8. \end{aligned} \quad (5)$$

The microbeam is subject to a viscous damping due to squeeze-film damping. And this effect is approximated by an equivalent damping coefficient \tilde{c} per unit length [39, 40]. \tilde{N}_a and \tilde{N}_r are the stretching and residual forces, respectively. Thus, the nondimensional governing equation of the transverse vibration of the beam can be given by [6]

$$\frac{\partial^4 w}{\partial x^4} + \frac{\partial^2 w}{\partial t^2} + c \frac{\partial w}{\partial t} - (N_a + N_r) \frac{\partial^2 w}{\partial x^2} = \alpha \left[\frac{V(t)}{(1-w)} \right]^2. \quad (6)$$

The boundary conditions of the fixed-fixed microbeam are as follows:

$$w(0, t) = w(1, t) = \frac{\partial w}{\partial x}(0, t) = \frac{\partial w}{\partial x}(1, t) = 0, \quad (7)$$

where the nondimensional variables and parameters are

$$\begin{aligned} w &= \frac{\tilde{w}}{d}, & x &= \frac{\tilde{x}}{L}, & t &= \frac{\tilde{t}}{t^*}, \\ \alpha &= \frac{6\varepsilon L^4}{\bar{E}h^3 d^3}, & t^* &= \sqrt{\frac{\rho b h L^4}{\bar{E}I}}, \\ N_r &= \frac{12\tilde{N}_r L^2}{\bar{E}h^3 b}, & c &= \frac{12\tilde{c} L^4}{\bar{E}h^3 b t^*}, \\ N_a &= 6 \left(\frac{d}{h} \right)^2 \int_0^1 \left(\frac{\partial w}{\partial x} \right)^2 dx. \end{aligned} \quad (8)$$

By dropping the time dependence of (6), the governing equation can be rewritten as

$$\frac{\partial^4 w}{\partial x^4} - (N_a + N_r) \frac{\partial^2 w}{\partial x^2} = \alpha \left[\frac{V}{(1-w)} \right]^2. \quad (9)$$

3. Numerical Analysis

In order to study the effect of the slant crack on the local stiffness discontinuity, each segment divided by the crack can be considered as a separate beam under undamped free vibration, with nondimensional equation form as follows:

$$\frac{\partial^4 w_i}{\partial x^4} + \frac{\partial^2 w_i}{\partial t^2} = 0, \quad i = 1, 2. \quad (10)$$

Using the separable solutions, $w_i(x, t) = Y_i(x)e^{j\omega t}$, in (10) leads to the associated eigenvalue problem:

$$\frac{\partial^4 Y_i}{\partial x^4} - \Lambda^4 Y_i = 0, \quad i = 1, 2 \quad (11)$$

with patching conditions as [25]

$$\begin{aligned} Y_1(lc^-) &= Y_2(lc^+), & Y_1''(lc^-) &= Y_2''(lc^+) \\ Y_1'''(lc^-) &= Y_2'''(lc^+), & Y_2'(lc^+) - Y_1'(lc^-) &= \Theta Y_2''(lc^+), \end{aligned} \quad (12)$$

where $\Lambda^4 = \omega^2$ and $lc = Xc/L$, with ω being the nondimensional nature frequency and Λ being the frequency parameter.

The general solution of the eigenvalue problem in (11) with boundary conditions in (7) and patching conditions in (12) is written as

$$\begin{aligned} Y_1(x) &= A_1 \sin[\Lambda x] + B_1 \cos[\Lambda x] + C_1 \sinh[\Lambda x] \\ &\quad + D_1 \cosh[\Lambda x], \quad (0 \leq x \leq lc) \\ Y_2(x) &= A_2 \sin[\Lambda(x-lc)] + B_2 \cos[\Lambda(x-lc)] \\ &\quad + C_2 \sinh[\Lambda(x-lc)] + D_2 \cosh[\Lambda(x-lc)], \\ &\quad (lc \leq x \leq 1), \end{aligned} \quad (13)$$

where A_i , B_i , C_i , D_i ($i = 1, 2$) are constants associated with the i th segment. And along with the process, the square of

the series value of Λ obtained corresponds to the nondimensional natural frequencies of associated modes.

Because of the nonlinearity of the static equation, the numerical solution is complicated and time consuming, and the direct application of the Galerkin method or finite difference method creates a set of nonlinear algebraic equations. In this paper, a method of two steps is used. In the first step, the SSLM is used [8, 41], and in the second step, the Galerkin method for solving the linear equation obtained is applied. Using the SSLM, it is assumed that w^k is the displacement of beam due to the applied voltage V^k . Therefore, by increasing the applied voltage to a new value, the displacement can be written as [6]

$$w_s^{k+1} = w_s^k + \delta w = w_s^k + \psi(x) \quad (14)$$

when

$$V^{k+1} = V^k + \delta V. \quad (15)$$

So, the equation of the static deflection of the fixed-fixed microbeam (equation (9)) can be rewritten in the step of $k+1$ as follows:

$$\frac{\partial^4 w_s^{k+1}}{\partial x^4} - (N_a^{k+1} + N_r) \frac{\partial^2 w_s^{k+1}}{\partial x^2} = \alpha \left[\frac{V}{(1 - w_s^{k+1})} \right]^2. \quad (16)$$

By considering the small value of δV , it is expected that ψ would be small enough. Thus by using the calculus of variation theory and Taylor's series expansion about w^k in (16) and applying the truncation to its first order for suitable value of δV , it is possible to obtain the desired accuracy. The linearized equation for calculating ψ can be expressed as

$$\begin{aligned} \frac{d^4 \psi}{dx^4} - (N_a^k + \delta N_a + N_r) \frac{d^2 \psi}{dx^2} - \delta N_a \frac{d^2 w}{dx^2} \Big|_{(w^k, V^k)} \\ - 2 \frac{\alpha (V^k)^2}{(1 - w_s^k)^3} \psi - 2 \frac{\alpha V^k \delta V}{(1 - w_s^k)^2} = 0, \end{aligned} \quad (17)$$

where the variation of the hardening term based on the calculus of variation theory can be expressed as $\delta N_a = \int_0^1 \psi(x) d^2 w / d^2 x |_{(w^k, V^k)} dx$. Similarly, because of the small value of δV and ψ , the value of multiplying δN_a by $d^2 \psi / dx^2$ would be small enough that can be neglected.

The linear differential equation obtained is solved by the Galerkin method, and $\psi(x)$ based on function spaces can be expressed as

$$\psi(x) = \sum_{j=1}^n a_j Y_j(x), \quad (18)$$

where $Y_j(x)$ is selected as the j th undamped linear mode shape of the cracked microbeam. $\psi(x)$ is approximated by truncating the summation series to a finite number n in this work.

Substituting (18) into (17) and multiplying by $Y_i(x)$ as a weight function in the Galerkin method and then integrating

the outcome from $x = 0$ to 1, a set of linear algebraic equations can be obtained as follows:

$$\sum_{j=1}^n K_{ij} a_j = F_i \quad (i = 1, 2, \dots, n), \quad (19)$$

where

$$\begin{aligned} K_{ij} &= K_{ij}^m + K_{ij}^a - K_{ij}^e, & K_{ij}^m &= \int_0^1 Y_i Y_j^{(4)} dx \\ K_{ij}^a &= \int_0^1 Y_i \left[(N_a^k + N_r) Y_j'' \right. \\ &\quad \left. + \left(\int_0^1 Y_i \frac{d^2 \omega}{dx^2} \Big|_{\omega^k, V^k} dx \right) \frac{d^2 \omega}{dx^2} \Big|_{\omega^k, V^k} \right] dx \\ K_{ij}^e &= 2\alpha (V^k)^2 \int_0^1 \frac{Y_i Y_j}{(1 - \omega^k)^3} dx \\ F_i &= 2\alpha (V^{k+1} - V^k) \int_0^1 \frac{Y_i(x)}{(1 - \omega^k)^2} dx. \end{aligned} \quad (20)$$

Considering the resonant microbeam (see Figure 1) actuated by an electric load that is composed of a DC component (polarization voltage) V_p and an AC component v_{ac} , the voltage signal can be given by

$$V(t) = V_p + v_{ac} \cos(\omega_e t), \quad (21)$$

where ω_e is the excitation frequency and $V_p \gg v_{ac}$.

In order to investigate the dynamic behavior of the microbeams more simply, the linearization of the right part of the governing equation (6) can be written as

$$\begin{aligned} \left[\frac{V(t)}{(1 - w)} \right]^2 &= [V_p^2 + 2V_p v_{ac} \cos(\omega_e t) + v_{ac}^2 \cos^2(\omega_e t)] \\ &\quad \cdot (1 + 2w + 3w^2 \dots) \\ &= V_p^2 (1 + 2w + 3w^2) + 2V_p v_{ac} \cos(\omega_e t), \end{aligned} \quad (22)$$

where the term involving v_{ac}^2 is dropped because typically $v_{ac} \ll V_p$ in resonant sensors. Using the Rayleigh-Ritz method, assuming the bending deflection of the beam to be of the form $w(x, t) = Y(x) * u(t)$ as analyzed previously, and substituting (22) into (6), we can get the governing equation as a single degree-of-freedom Duffing equation as follows:

$$\ddot{u} + \omega_0^2 u - \hbar u^3 = \lambda \dot{u} + \ell u^2 + \chi \cos(\omega_e t) + \kappa, \quad (23)$$

where $u(t)$, $\dot{u}(t)$, $\ddot{u}(t)$ are the displacement, speed, and acceleration of the center layer of the beam. And one has

$$\begin{aligned} \omega_0^2 &= a_1 - N_r a_2 - 2\alpha V_p^2, & \hbar &= \frac{6d^2 a_3}{h^2} \\ \lambda &= -c, & \ell &= 3\alpha b_3 V_p^2, & \chi &= 2\alpha b_1 v_{ac} V_p^2, \\ & & \kappa &= \alpha b_1 V_p^2, \end{aligned} \quad (24)$$

where

$$\begin{aligned} a_1 &= \int_0^1 Y^{(4)}(x) Y(x) dx, & a_2 &= \int_0^1 Y^{(2)}(x) Y(x) dx \\ a_3 &= a_2 \int_0^1 [Y'(x)]^2 dx, & b_i &= \int_0^1 Y^i(x) dx, \\ & & (i &= 1, 2, 3), \quad b_2 = 1. \end{aligned} \quad (25)$$

To calculate the nonlinear response of the electrostatically actuated microbeam given by (23), the multiple scale perturbation theory is employed. The response to the primary resonance excitation of its first mode is analyzed because it is the case that is used in resonator applications. Still, the analysis is general and can be used to study nonlinear responses of the beam to a primary resonance of any of its modes. The excitation frequency ω_e is usually tuned close to the fundamental nature frequency of mechanical vibrations, namely, $\omega_e = \omega_0 + \eta\sigma$, where η is a dimensionless small parameter and σ is a small detuning parameter. By redefining the parameters as $\hbar = \eta\hbar$, $\lambda = \eta\lambda$, $\ell = \eta\ell$, $\chi = \eta\chi$, and $\kappa = \eta\kappa$, (23) can be written as

$$\ddot{u} + \omega_0^2 u = \eta [\hbar u^3 + \lambda \dot{u} + \ell u^2 + \chi \cos(\omega_0 + \varepsilon\sigma)t + \kappa]. \quad (26)$$

To solve (26), two time scales, $T_0 = t$ and $T_1 = \eta t$, are introduced, and the first-order uniform solution is given in the form

$$u(t, \eta) = u_0(T_0, T_1) + \eta u_1(T_0, T_1). \quad (27)$$

Substituting (27) into (26) and equating coefficients of like powers of ε , the linear partial differential equations of order η^0 and order η^1 are obtained as

$$\begin{aligned} D_0^2 u_0 + \omega_0^2 u_0 &= 0 \\ D_0^2 u_1 + \omega_0^2 u_1 &= -2D_0 D_1 u_0 + \hbar u_0^3 + \lambda D_0 u_0 + \ell u_0^2 \\ &+ \chi \cos(\omega_0 + \eta\sigma)T_0 + \kappa, \end{aligned} \quad (28)$$

where $D_0 = \partial/\partial T_0$ and $D_1 = \partial/\partial T_1$. The general solution of the first equation of (28) can be written as

$$u_0(T_0, T_1) = a(T_0) \cos[\omega_0 T_0 + \delta(T_1)] = A(T_1) e^{j\omega_0 T_0} + cc, \quad (29)$$

where $A(T_1) = a(T_0) e^{j\delta(T_1)}/2$ and cc denotes a complex conjugate. Equation (29) is then substituted into the second equation of (28), and the trigonometric functions are expanded. The elimination of the secular terms yields two first-order nonlinear ordinary differential equations that allow for a stability analysis. Furthermore, the modulation of the response with the amplitude a and phase δ is given by

$$\begin{aligned} D_1 a &= \frac{\lambda a}{2} + \frac{\chi}{2\omega_0} \sin \varphi \\ a D_1 \delta &= -\left(\frac{3\hbar a^3}{8\omega_0} + \frac{\chi}{2\omega_0} \cos \varphi \right), \end{aligned} \quad (30)$$

where $\varphi = \sigma T_1 - \delta$. The steady-state motion occurs when $D_1 a = D_1 \varphi = 0$, which corresponds to singular points of (30). Then the steady-state frequency response is obtained as

$$\left[\left(\omega_e - \omega_0 + \frac{3\hbar A_0^2}{8\omega_0} \right)^2 + \left(\frac{\lambda}{2} \right)^2 \right] A_0^2 = \left(\frac{\chi}{2\omega_0} \right)^2, \quad (31)$$

where A_0 is the resonance amplitude when it is steady-state. While one has $A_0 \leq \chi/(\lambda\omega_0)$, a function of the independent incentive frequency is found to be

$$\omega_e = \omega_0 - \frac{3\hbar}{8\omega_0} A_0^2 \pm \sqrt{\frac{\chi^2}{4\omega_0^2 A_0^2} - \frac{1}{4} \lambda^2}. \quad (32)$$

Defining nondimensional resonance frequency, $\Omega = \omega_e/\omega_0$, (32) can be expressed as

$$\Omega = 1 - \frac{3\hbar}{8\omega_0^2} A_0^2 \pm \sqrt{\frac{\chi^2}{4\omega_0^4 A_0^2} - \frac{\lambda^2}{4\omega_0^2}}. \quad (33)$$

As indicated in (33), the nondimensional design parameters affect the resonance frequency through changing the effective nonlinearity of the undamped linear mode shape.

The maximum resonance amplitude is reached when the magnitude under the square root is zero [42]. Hence,

$$A_{\max} = \frac{\chi}{\lambda\omega_0} \quad (34)$$

and the corresponding frequency is

$$\Omega = 1 - \frac{3\hbar}{8\omega_0^2} A_{\max}^2. \quad (35)$$

The curve determined by (35) is defined as the skeleton line, which manifests the relation between the peak amplitude and the resonance frequency, dominating the shape of the amplitude-frequency response (AFR). The AFR curves indicate the nonlinear characteristics of the microbeam. According to (33) and (35), the AFR curves and the skeleton lines not only are affected by parameters of the beam structure and the slant crack, but also are related to the external incentives, namely, the DC and AC voltages.

4. Results and Discussion

4.1. Frequency and Mode Shapes. The geometric and material properties of the microbeam are as follows: $L = 250 \mu\text{m}$, $b = 50 \mu\text{m}$, $\varepsilon = 8.85 \text{ PF/m}$, $h = 3 \mu\text{m}$, $d = 1 \mu\text{m}$, $E = 1.69 \text{ GPa}$, $\rho = 2331 \text{ kg/m}^3$, and $\nu = 0.06$ [6]. Figure 2 shows the effects of the crack depth ratio for selected crack positions ($lc = 0.05, 0.25, 0.5$) and slant angles ($\theta = 0^\circ, 20^\circ$) on the value of the first four ($n = 1-4$) nature frequencies along the depth ratio. It can be found that increasing the depth ratio will gradually decrease the natural frequencies, with the tendency serving as the confirmation of the EBB theory according to Hasheminejad et al. [43]. Some important observations are found. Increasing the crack depth ratio does not have any impact on the cases of $n = 2$ ($lc = 0.5$) and $n = 4$ ($lc = 0.5$),

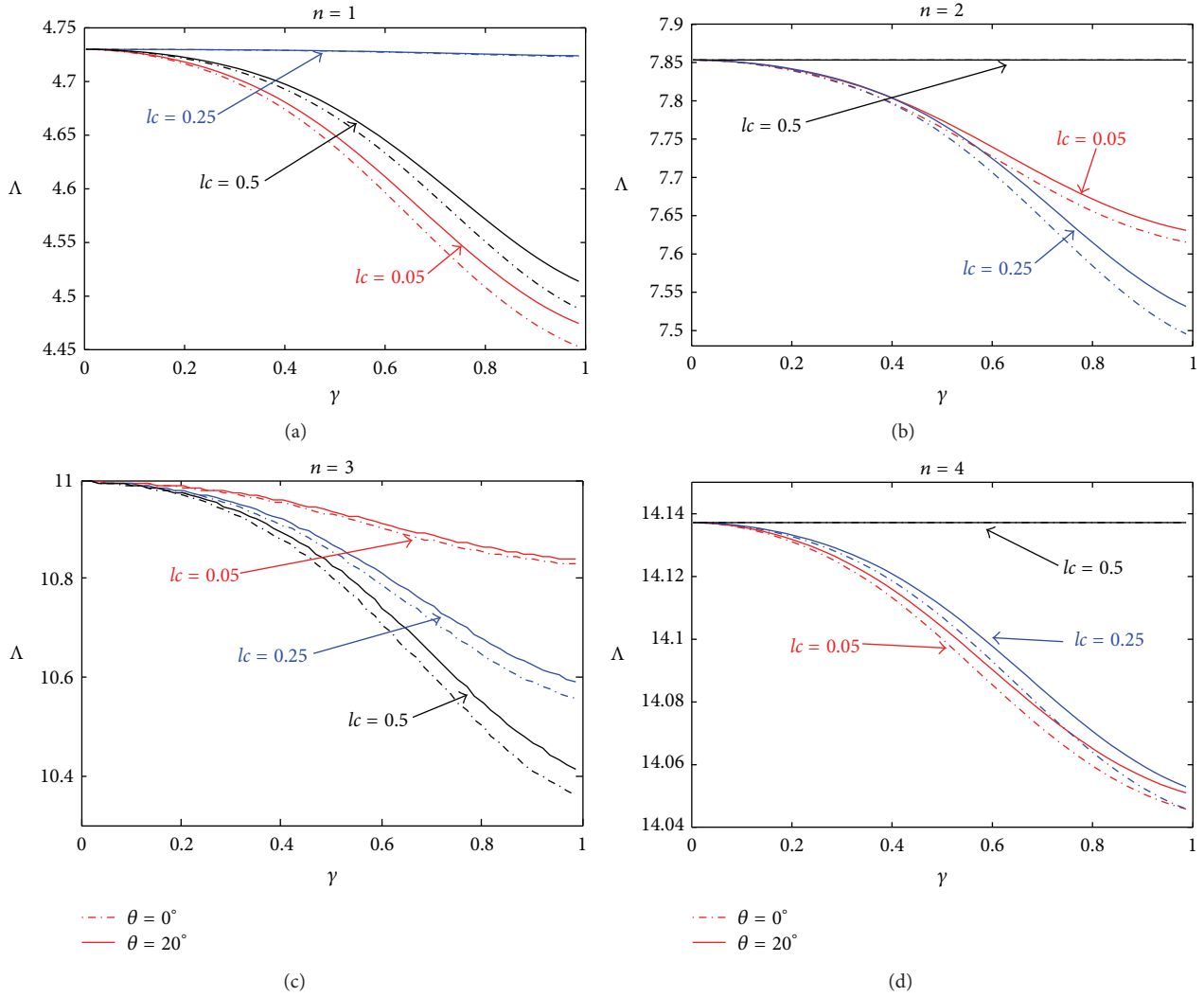


FIGURE 2: The first four nondimensional natural frequencies of the microbeam along with the depth ratio of the crack for three crack positions and two slant angles.

TABLE 1: Values of the first four frequency parameters for a fixed-fixed beam with different crack positions and crack slant angles. Crack depth ratio $\gamma = 0.5$.

| Λ | $lc = 0.05$ | | | | $lc = 0.5$ | | | |
|-----------|--------------------|---------------------|---------------------|---------------------|--------------------|---------------------|---------------------|---------------------|
| | $\theta = 0^\circ$ | $\theta = 15^\circ$ | $\theta = 30^\circ$ | $\theta = 45^\circ$ | $\theta = 0^\circ$ | $\theta = 45^\circ$ | $\theta = 30^\circ$ | $\theta = 45^\circ$ |
| $n = 1$ | 4.6392 | 4.6452 | 4.6616 | 4.6836 | 4.6673 | 4.6719 | 4.6840 | 4.6995 |
| $n = 2$ | 7.7647 | 7.7702 | 7.7855 | 7.8065 | 7.8532 | 7.8532 | 7.8532 | 7.8532 |
| $n = 3$ | 10.929 | 10.933 | 10.944 | 10.960 | 10.806 | 10.819 | 10.854 | 10.901 |
| $n = 4$ | 14.100 | 14.102 | 14.108 | 14.117 | 14.137 | 14.137 | 14.137 | 14.137 |

which exhibits the same trend with results presented by Hasheminejad et al. [43]. This can be explained by the fact that none of the crack positions ($lc = 0.5$) lie on the vibration nodes for the beam vibrating in first and third modes ($n = 1, 3$), while in the case of the second and fourth modes ($n = 2, 4$), the crack position ($lc = 0.5$) is exactly set on the vibration nodes.

Take the slant angle of the crack into account, the increment in angle leads to a gradual increase of the four

nature frequencies, except the special cases mentioned above. Besides, the effect of the crack position on frequency differs in different modes.

More detailed changes of the first four frequency parameters for the fixed-fixed microbeam with different crack slant angles θ for a crack located at positions $lc = 0.05$ and 0.5 are given in Table 1, and the crack depth ratio $\gamma = 0.5$.

The first-mode shapes of the cracked microbeam of different geometry characteristics are displayed in Figure 3.

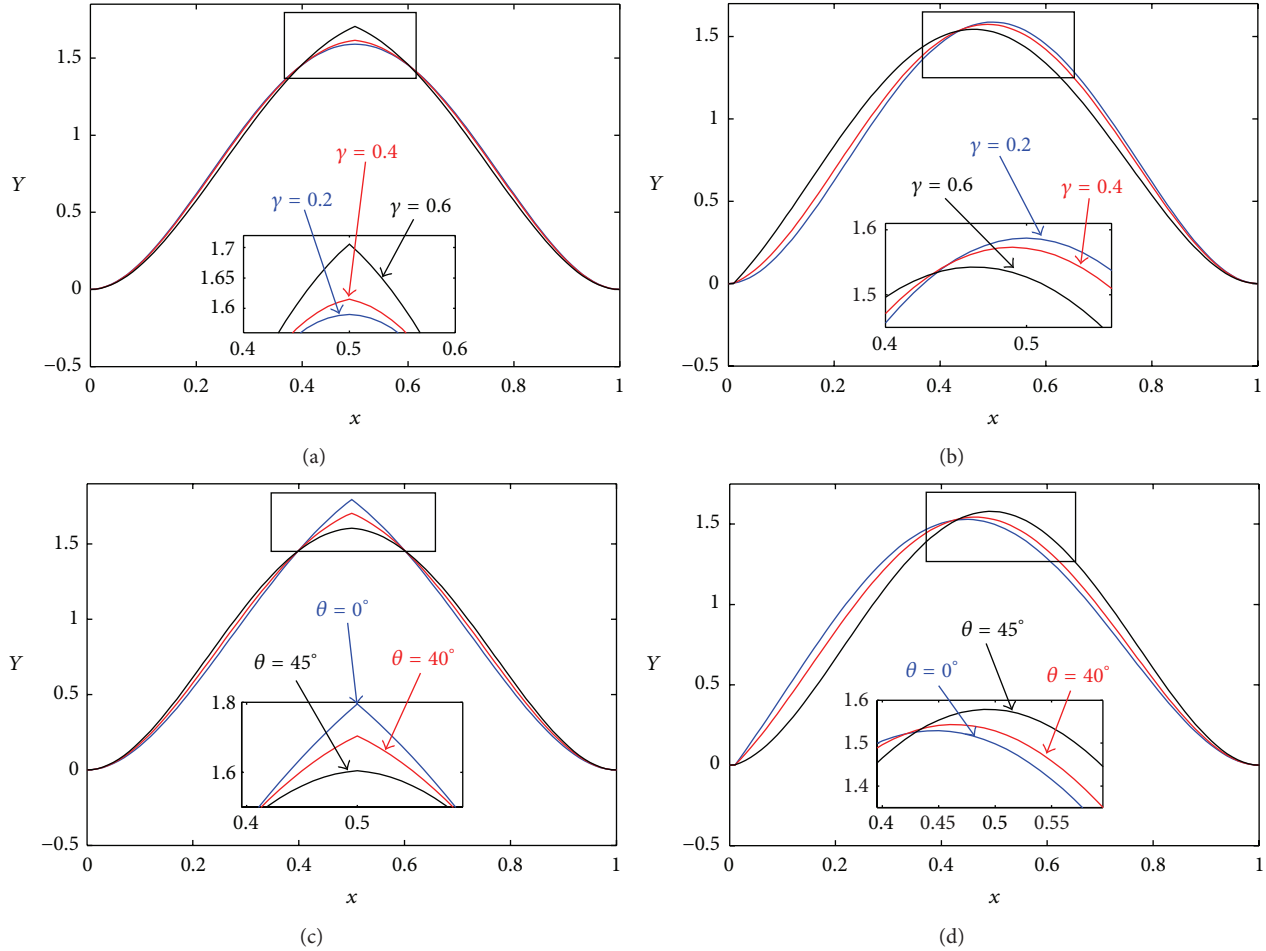


FIGURE 3: The effects of the depth ratio (a, b) and the slant angle (c, d) of the slant crack on the first-mode shapes of the beam at different positions. (a) and (c) $lc = 0.5$; (b) and (d) $lc = 0.05$.

The abscissa is the nondimensional distance of the crack from the left end of the microbeam, and the ordinate is the vibration amplitude of first-mode shape. It manifests that the effects of the slant angle and depth ratio on the first-mode shapes depend on the crack position. For example, the growth in the depth ratio will increase the maximum vibration amplitude along the beam length when the crack is near the center point of the beam ($lc = 0.5$, see Figure 3(a)), but it will lead the inverse trend when the crack is located at the end part ($lc = 0.05$, see Figure 3(b)). Similarly, when it comes to the slant angle (see Figures 3(c) and 3(d)), the angle increment causes decrease in the maximum vibration amplitude when the crack is located near the center part of the beam, but it increases when it is near the end. The effect differences in vibration amplitude are in good agreement with the ones in the nature frequency. Additionally, the maximum vibration amplitude is larger when the crack position gets near the center part.

4.2. Pull-In Voltage Analysis. In the pull-in voltage analysis, voltages will differ when different voltage increment is applied, but the difference is small enough to be neglected.

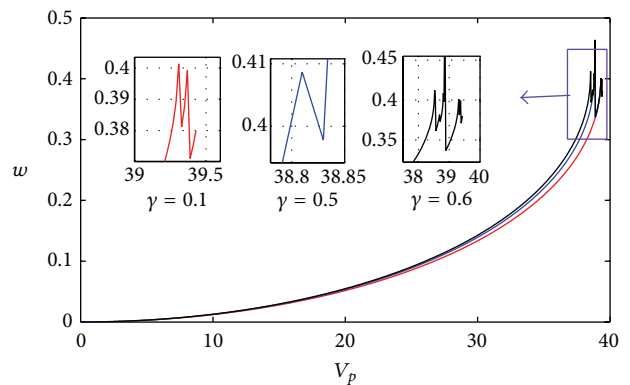


FIGURE 4: The displacement of center point of the beam with the DC voltage for case of position 0.5, slant angle 45° , and a static voltage increment of 0.02 V, for three depth ratios (0.1, 0.5, and 0.6).

Just as seen in Figure 4, the abscissa is the value of the applied DC voltage, and the ordinate is the transverse deflection of the middle point of the beams. Figure 4 illustrates how the microbeam resonator loses stability. Before the DC voltage

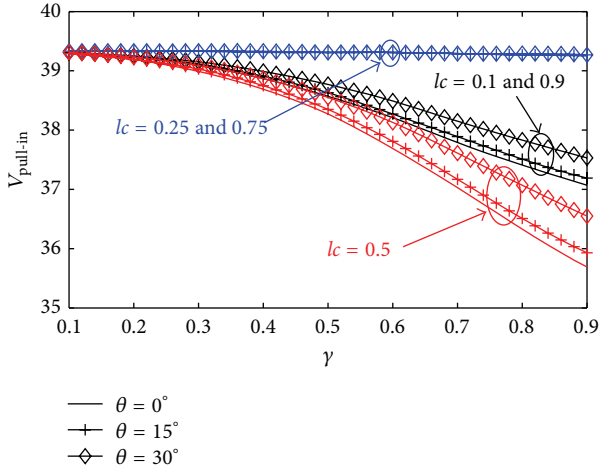


FIGURE 5: Variation of the pull-in voltage of the fixed-fixed microbeam with the crack depth ratio (for three crack positions and three slant angles).

increases to a certain value, it exhibits a steady increase trend in the deflection of center point of the beam. Once the DC voltage reaches a critical point, it enters the pull-in instability zone, where the deflection begins oscillating violently with the increasing of the DC voltage. This critical point indicates the pull-in voltage, and the corresponding displacement is the pull-in displacement.

By using the modified model proposed, the effects of the slant crack parameters on static pull-in voltage of the fixed-fixed microbeam are investigated. The variation of the pull-in voltages of the cracked beam of different crack depth ratio (for three crack positions and three slant angles) is shown in Figure 5. It is shown that the crack position has a strong effect on the pull-in voltage. When the crack is near to the middle of the microbeam, especially for the higher crack depth ratios, the pull-in voltage is greatly reduced. And the position of $lc = 0.25$ and 0.75 is more ineffective on the pull-in voltage than other positions. In addition, the effect of the slant angle on the pull-in voltage is appreciable. The pull-in voltage is increased slightly along with the increase of the angle. In addition, the detailed effect of the crack position on pull-in voltage of the beam is investigated and shown in Figure 6. As shown, interestingly, there are several extreme points located in $lc = 0.25, 0.5, 0.75$ and two endpoints. As shown in the figure when the crack is located at $lc = 0.25$ and 0.75 , it has the lowest effect on the pull-in voltage and when $lc = 0.5$, the effect is greater, but endpoints are still lower. As shown, the rate of the variation is smaller in larger crack slant angle. The results gained above show that the crack position has more significant effect on the pull-in voltage of the beam than the crack depth ratio or the slant angel. And the slant angel exhibits a contrary effect on the pull-in voltage compared with the crack depth ratio.

4.3. *Dynamic Response Analysis.* The dynamic response of the microbeam described by (31) has been taken into account. The set of parameters applied in all the numerical simulations

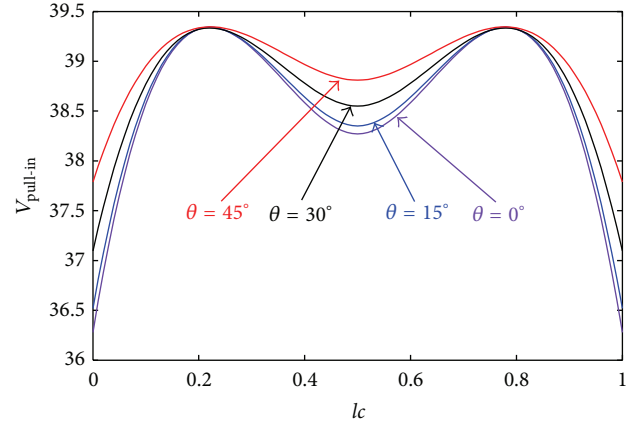


FIGURE 6: Comparison of the pull-in voltage of the slant-cracked microbeam with the crack position (for four slant angles).

TABLE 2: Parameters values for the solution and results values.

| Figure | Varying parameters | Resonant frequency | Max-amplitude |
|--------------|---------------------------------|--------------------|---------------|
| Figure 7 | $lc = 0.05$ | 21.63 | 0.4317 |
| | $lc = 0.25$ | 22.34 | 0.4150 |
| | $lc = 0.5$ | 22.06 | 0.4193 |
| Figure 8(a) | $\gamma = 0.1$ $lc = 0.5$ | 22.34 | 0.4141 |
| | $\gamma = 0.5$ $lc = 0.5$ | 22.04 | 0.4188 |
| Figure 8(b) | $\gamma = 0.7$ $lc = 0.5$ | 21.43 | 0.4289 |
| | $\gamma = 0.1$ $lc = 0.05$ | 22.33 | 0.4143 |
| | $\gamma = 0.5$ $lc = 0.05$ | 21.88 | 0.4235 |
| Figure 9(a) | $\gamma = 0.7$ $lc = 0.05$ | 21.09 | 0.4407 |
| | $\theta = 0^\circ$ $lc = 0.5$ | 18.29 | 0.4399 |
| | $\theta = 23^\circ$ $lc = 0.5$ | 18.53 | 0.4377 |
| Figure 9(a) | $\theta = 45^\circ$ $lc = 0.5$ | 20.88 | 0.4453 |
| | $\theta = 70^\circ$ $lc = 0.5$ | 21.56 | 0.4305 |
| Figure 9(b) | $\theta = 0^\circ$ $lc = 0.05$ | 20.41 | 0.4561 |
| | $\theta = 23^\circ$ $lc = 0.05$ | 20.53 | 0.4532 |
| | $\theta = 45^\circ$ $lc = 0.05$ | 20.88 | 0.4453 |
| | $\theta = 70^\circ$ $lc = 0.05$ | 21.56 | 0.4305 |
| Figure 10(a) | $V_p = 1.0$ V | 22.06 | 0.07172 |
| | $V_p = 6.0$ V | 22.04 | 0.2513 |
| | $V_p = 6.0$ V | 21.99 | 0.4317 |
| Figure 10(a) | $v_{ac} = 0.01$ V | 22.04 | 0.04188 |
| | $v_{ac} = 0.5$ V | 22.04 | 0.2094 |
| | $v_{ac} = 0.1$ V | 22.04 | 0.4188 |

are $\theta = 45^\circ, lc = 0.5, \gamma = 0.5, V_p = 3.5$ V, and $v_{ac} = 0.1$ V. The resonance frequency and resonance amplitude are acquired by varying one of the parameters, as listed in Table 2.

As plotted in Figures 7–10, the dynamic response curves of the first mode are acquired. The abscissa is the nondimensional resonance frequency, and the ordinate is the resonance amplitude. But the abscissa of the subgraphs in the graphs is the excitation frequency. As plotted, when the resonance

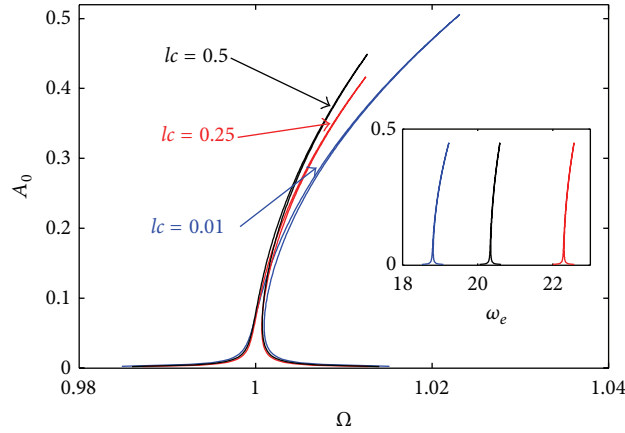


FIGURE 7: The effects of the crack position on the dynamic response of microbeams of different positions lc .

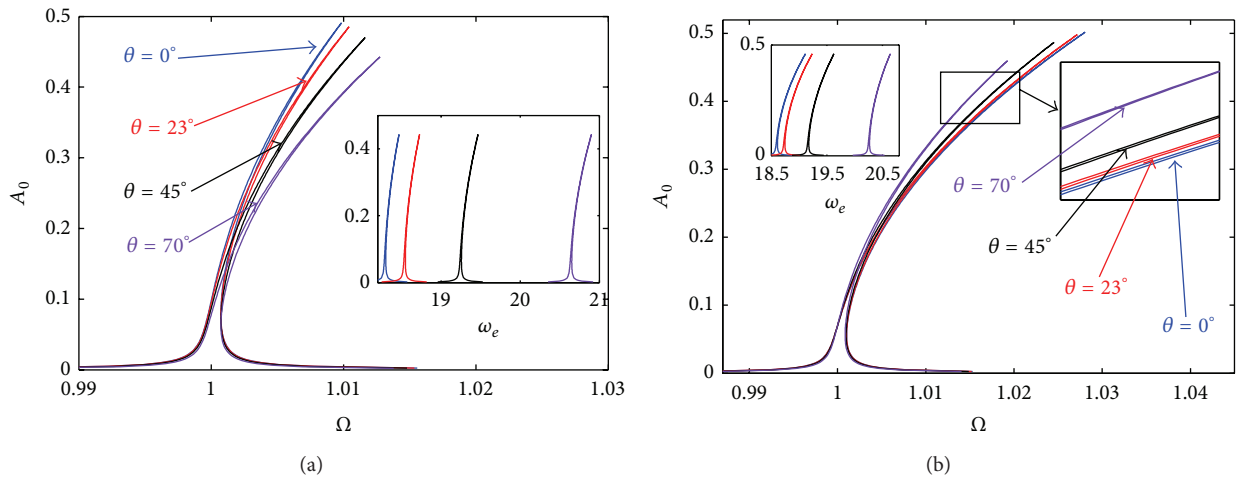


FIGURE 8: The effects of the slant angle of the crack on the dynamic response of microbeams. (a) $lc = 0.5$; (b) $lc = 0.05$.

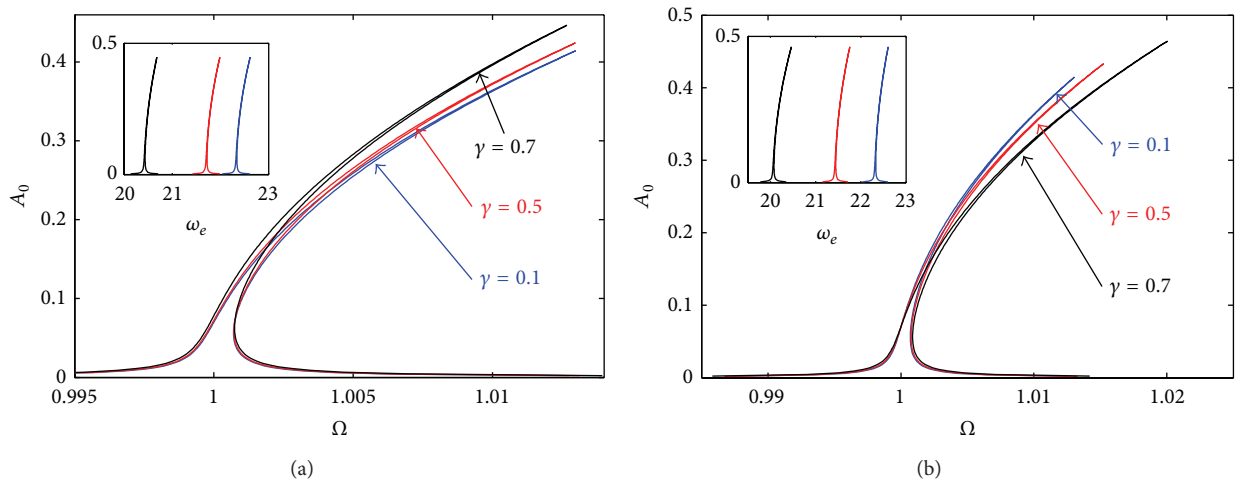


FIGURE 9: The effects of the crack depth ratio of the crack on the dynamic response of microbeams. (a) $lc = 0.5$; (b) $lc = 0.05$.

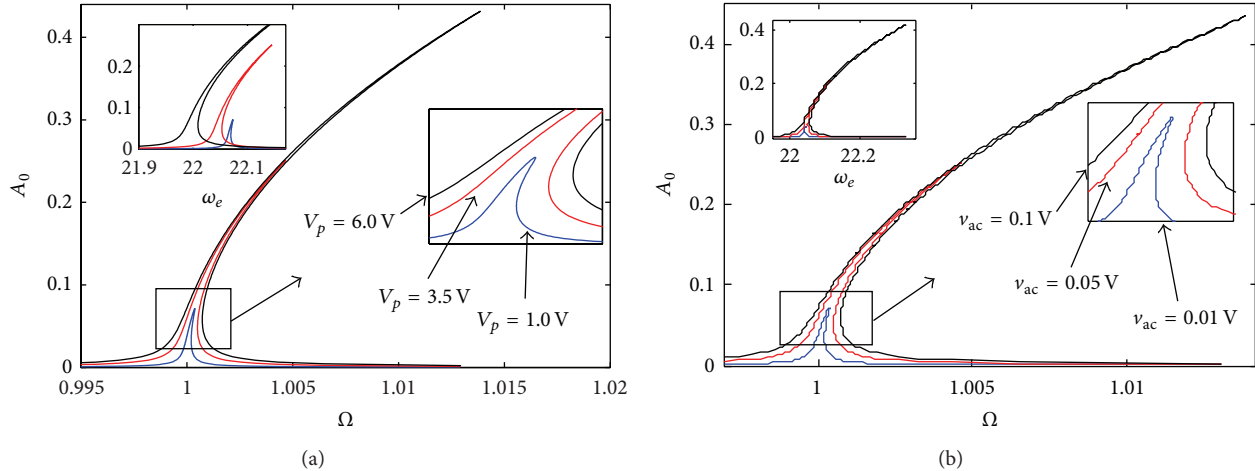


FIGURE 10: The effects of the external incentives on the dynamic response of microbeams. (a) DC voltage; (b) AC voltage.

frequency grows sufficiently large, the two branches of all the curves merge and produce a standard resonance peak with a hardening characteristic. A larger degree of curvature means the stronger hardening behavior, which points out that the nonlinearity strengthens.

Figure 7 illustrates the influence of the crack position on the frequency response of the microbeam. When the crack is located at the middle point of the beam, the nonlinear behavior of the system is not evident. As the crack approaches the fixed end, the influence of the nonlinearities becomes more obvious showing a typical hardening characteristic. At most frequencies, it is noted that the fact that the crack approaches the fixed end results in a decrease in the steady-state amplitude. For case of $lc = 0.01$, the value of the nondimensional resonance frequency where the maximum amplitude occurs is bigger than the other two cases.

The influence of the slant angles of crack θ on the dynamic response differs at different crack locations as shown in Figure 8. When the crack is located at the center part of the microbeam ($lc = 0.5$, Figure 8(a)), the microbeam with a slant crack of a bigger angle displays a stronger nonlinearity but a less resonance amplitude at most frequencies. Increasing the slant angle decreases the maximum resonance amplitude and slightly increases the corresponding frequency. But if the crack is located at the fixed end of the microbeam ($lc = 0.05$, Figure 8(b)), the result becomes that the microbeam with a slant crack of a smaller angle depicts the stronger nonlinearity and the less resonance amplitude. Meanwhile, increasing the slant angle of the crack has no significant influence on the maximum resonance amplitude but decreases the corresponding frequency.

When it comes to the influence of the crack depth ratio γ on the dynamic response, the characteristics displayed in Figure 9 are similar to what is seen in Figure 8. It is noted that a deeper crack affects the dynamic response of the microbeam in the same way with how a slant crack with a smaller slant angle does. Increasing the depth ratio of the crack located at the center part of the microbeam ($lc = 0.5$, Figure 9(a)) weakens the nonlinear behavior of

the microbeam and enlarges the resonance amplitude at most frequencies, as well as the maximum resonance amplitude, but it has no significant influence on the corresponding resonance frequency, contrary to the effects of the crack depth ratio on the response characteristics located at the fixed end ($lc = 0.05$, Figure 9(b)).

Figure 10 illustrates the influence of the external incentives on the dynamic response of microbeams including the DC voltage (Figure 10(a)) and the AC voltage (Figure 10(b)). As plotted in the two figures, it can be directly seen that increased external incentives result in an obvious increase in the steady-state amplitude at most frequencies as expected. As the value of the external incentives is decreased, the hardening behavior weakens. A resonance response will not be seen if the incentive values are significantly reduced. This result is in agreement with that found by Younis and Nayfeh [44].

5. Conclusion

In this work, the model of slant open crack is established, and it is applied into the continuous vibration equation of electrostatically actuated fixed-fixed microbeams. Analytic results of the natural frequency, the corresponding mode shapes, and the numerical results of the pull-in voltages are presented. By comparing the calculated results in different cases, the effects of the crack depth ratio, crack position, and the slant angle on the dynamic behaviors and the pull-in voltages are investigated. It is shown that except for some special cases the first four nature frequencies decrease with the increase of the crack depth ratio, but the opposite change is displayed when the slant angle of the crack increases. In addition, the effect of the crack position on frequency differs in different modes. Furthermore, the influences of the crack position, slant angle, and the depth ratio on the pull-in voltages are similar to those on frequencies, respectively. The pull-in voltage decreases the most when the crack is located at the middle point of the beams and the least when the crack is located at the quarter point. Finally,

the dynamic response of the beam is investigated by employing the multiple scale perturbation theory. It is found that the response demonstrates a hardening characteristic, which is affected by the geometry parameters of the slant crack and the electric incentives. The nonlinearity of the resonance response gets enlarged when the crack position approaches the fixed end of the microbeam or the DC voltage and AC voltage value amplifies. The effects of the crack depth ratio and the slant angle on the dynamic response vary in different positions.

Conflict of Interests

The authors declare that there is no conflict of interests regarding the publication of this paper.

Acknowledgments

The authors gratefully acknowledge projects supported by the National Natural Science Foundation of China (no. 11322215), National Program for Support of Top-notch Young Professionals, the Fok Ying Tung Education Foundation (no. 141050), and the Innovation Program of Shanghai Municipal Education Commission (no. 15ZZ010).

References

- [1] J. Tamayo, P. M. Kosaka, J. J. Ruz, Á. San Paulo, and M. Calleja, "Biosensors based on nanomechanical systems," *Chemical Society Reviews*, vol. 42, no. 3, pp. 1287–1311, 2013.
- [2] L. M. Bellan, D. Wu, and R. S. Langer, "Current trends in nanobiosensor technology," *Wiley Interdisciplinary Reviews: Nanomedicine and Nanobiotechnology*, vol. 3, no. 3, pp. 229–246, 2011.
- [3] S. Pourkamali and F. Ayazi, "Electrically coupled MEMS band-pass filters: part I: with coupling element," *Sensors and Actuators A: Physical*, vol. 122, no. 2, pp. 307–316, 2005.
- [4] S. Pourkamali and F. Ayazi, "Electrically coupled MEMS band-pass filters: part II. Without coupling element," *Sensors and Actuators A: Physical*, vol. 122, no. 2, pp. 317–325, 2005.
- [5] M. Fathalilou, A. Motallebi, H. Yagubizade, G. Rezaadeh, K. Shirazi, and Y. Alizadeh, "Mechanical behavior of an electrostatically-actuated microbeam under mechanical shock," *Journal of Solid Mechanics*, vol. 1, no. 1, pp. 45–57, 2009.
- [6] A. Motallebi, M. Fathalilou, and G. Rezaadeh, "Effect of the open crack on the pull-in instability of an electrostatically actuated micro-beam," *Acta Mechanica Solida Sinica*, vol. 25, no. 6, pp. 627–637, 2012.
- [7] H. C. Nathanson, W. E. Newell, R. A. Wickstrom, and J. R. Davis, "The resonant gate transistor," *IEEE Transactions on Electron Devices*, vol. 14, no. 3, pp. 117–133, 1967.
- [8] D. Bernstein, P. Guidotti, and J. Pelesko, "Mathematical analysis of an electrostatically actuated MEMS device," in *Proceedings of the Modelling & Simulation of Microsystems*, pp. 489–492, 2000.
- [9] J. A. Pelesko, "Multiple solutions in electrostatic MEMS," in *Proceedings of the International Conference on Modeling and Simulation of Microsystems (MSM '01)*, pp. 290–293, March 2001.
- [10] W.-M. Zhang, H. Yan, Z.-K. Peng, and G. Meng, "Electrostatic pull-in instability in MEMS/NEMS: a review," *Sensors and Actuators A: Physical*, vol. 214, pp. 187–218, 2014.
- [11] E. M. Abdel-Rahman, M. I. Younis, and A. H. Nayfeh, "Characterization of the mechanical behavior of an electrically actuated microbeam," *Journal of Micromechanics and Microengineering*, vol. 12, no. 6, pp. 759–766, 2002.
- [12] V. Y. Taffoti Yolong and P. Woaf, "Dynamics of electrostatically actuated micro-electro-mechanical systems: single device and arrays of devices," *International Journal of Bifurcation and Chaos*, vol. 19, no. 3, pp. 1007–1022, 2009.
- [13] F. Najar, S. Choura, S. El-Borgi, E. M. Abdel-Rahman, and A. H. Nayfeh, "Modeling and design of variable-geometry electrostatic microactuators," *Journal of Micromechanics and Microengineering*, vol. 15, no. 3, pp. 419–429, 2005.
- [14] B.-G. Nam, S. Tsuchida, and K. Watanabe, "Fatigue crack growth driven by electric fields in piezoelectric ceramics and its governing fracture parameters," *International Journal of Engineering Science*, vol. 46, no. 5, pp. 397–410, 2008.
- [15] T. G. Chondros, A. D. Dimarogonas, and J. Yao, "Vibration of a beam with a breathing crack," *Journal of Sound and Vibration*, vol. 239, no. 1, pp. 57–67, 2001.
- [16] A. D. Dimarogonas, "Vibration of cracked structures: a state of the art review," *Engineering Fracture Mechanics*, vol. 55, no. 5, pp. 831–857, 1996.
- [17] M. Rezaee and R. Hassannejad, "Free vibration analysis of simply supported beam with breathing crack using perturbation method," *Acta Mechanica Solida Sinica*, vol. 23, no. 5, pp. 459–470, 2010.
- [18] S. Caddemi, I. Calì, and M. Marletta, "The non-linear dynamic response of the Euler-Bernoulli beam with an arbitrary number of switching cracks," *International Journal of Non-Linear Mechanics*, vol. 45, no. 7, pp. 714–726, 2010.
- [19] A. Khorram, F. Bakhtiari-Nejad, and M. Rezaeeian, "Comparison studies between two wavelet based crack detection methods of a beam subjected to a moving load," *International Journal of Engineering Science*, vol. 51, pp. 204–215, 2012.
- [20] M. Donà, A. Palmeri, and M. Lombardo, "Exact closed-form solutions for the static analysis of multi-cracked gradient-elastic beams in bending," *International Journal of Solids and Structures*, vol. 51, no. 15-16, pp. 2744–2753, 2014.
- [21] M. Kisa and M. Arif Gurel, "Free vibration analysis of uniform and stepped cracked beams with circular cross sections," *International Journal of Engineering Science*, vol. 45, no. 2–8, pp. 364–380, 2007.
- [22] M. I. Friswell and J. E. T. Penny, "Crack modeling for structural health monitoring," *Structural Health Monitoring*, vol. 1, no. 2, pp. 139–148, 2002.
- [23] T. G. Chondros, A. D. Dimarogonas, and J. Yao, "A continuous cracked beam vibration theory," *Journal of Sound and Vibration*, vol. 215, no. 1, pp. 17–34, 1998.
- [24] S. Caddemi, I. Calì, and F. Cannizzaro, "The influence of multiple cracks on tensile and compressive buckling of shear deformable beams," *International Journal of Solids and Structures*, vol. 50, no. 20-21, pp. 3166–3183, 2013.
- [25] H. P. Lin, S. C. Chang, and J. D. Wu, "Beam vibrations with an arbitrary number of cracks," *Journal of Sound and Vibration*, vol. 258, no. 5, pp. 987–999, 2002.
- [26] L. Rubio and J. Fernández-Sáez, "A note on the use of approximate solutions for the bending vibrations of simply supported cracked beams," *Journal of Vibration and Acoustics, Transactions of the ASME*, vol. 132, no. 2, 2010.
- [27] M. Afshari and D. J. Inman, "Continuous crack modeling in piezoelectrically driven vibrations of an Euler-Bernoulli beam," *Journal of Vibration and Control*, vol. 19, no. 3, pp. 341–355, 2013.

- [28] M. H. Ghayesh, M. Amabili, and H. Farokhi, "Nonlinear forced vibrations of a microbeam based on the strain gradient elasticity theory," *International Journal of Engineering Science*, vol. 63, pp. 52–60, 2013.
- [29] M. H. Ghayesh, H. Farokhi, and M. Amabili, "Nonlinear behaviour of electrically actuated MEMS resonators," *International Journal of Engineering Science*, vol. 71, pp. 137–155, 2013.
- [30] S.-C. Sun, C.-W. Chung, C.-M. Hsu, and J.-H. Kuang, "The squeeze film damping effect on dynamic responses of microelectromechanical resonators," *Applied Mechanics and Materials*, vol. 284–287, pp. 1961–1965, 2013.
- [31] H. O. Ekici and H. Boyaci, "Effects of non-ideal boundary conditions on vibrations of microbeams," *Journal of Vibration and Control*, vol. 13, no. 9–10, pp. 1369–1378, 2007.
- [32] F. M. Alsaleem, M. I. Younis, and H. M. Ouakad, "On the nonlinear resonances and dynamic pull-in of electrostatically actuated resonators," *Journal of Micromechanics and Microengineering*, vol. 19, no. 4, Article ID 045013, 2009.
- [33] Y. Lin and F. Chu, "The dynamic behavior of a rotor system with a slant crack on the shaft," *Mechanical Systems and Signal Processing*, vol. 24, no. 2, pp. 522–545, 2010.
- [34] Q. Han, J. Zhao, and F. Chu, "Dynamic analysis of a geared rotor system considering a slant crack on the shaft," *Journal of Sound and Vibration*, vol. 331, no. 26, pp. 5803–5823, 2012.
- [35] G. De Pasquale and A. Soma, "MEMS mechanical fatigue: effect of mean stress on gold microbeams," *Journal of Microelectromechanical Systems*, vol. 20, no. 4, pp. 1054–1063, 2011.
- [36] A. K. Darpe, "Coupled vibrations of a rotor with slant crack," *Journal of Sound and Vibration*, vol. 305, no. 1–2, pp. 172–193, 2007.
- [37] M. Kisa and J. Brandon, "Effects of closure of cracks on the dynamics of a cracked cantilever beam," *Journal of Sound and Vibration*, vol. 238, no. 1, pp. 1–18, 2000.
- [38] A. K. Darpe, "Dynamics of a Jeffcott rotor with slant crack," *Journal of Sound and Vibration*, vol. 303, no. 1–2, pp. 1–28, 2007.
- [39] J. P. Lynch, A. Partridge, K. H. Law, T. W. Kenny, A. S. Kiremidjian, and E. Carryer, "Design of piezoresistive MEMS-based accelerometer for integration with wireless sensing unit for structural monitoring," *Journal of Aerospace Engineering*, vol. 16, no. 3, pp. 108–114, 2003.
- [40] M. I. Younis, E. M. Abdel-Rahman, and A. Nayfeh, "A reduced-order model for electrically actuated microbeam-based MEMS," *Journal of Microelectromechanical Systems*, vol. 12, no. 5, pp. 672–680, 2003.
- [41] G. Rezazadeh, M. Fathalilou, R. Shabani, S. Tarverdilou, and S. Talebian, "Dynamic characteristics and forced response of an electrostatically-actuated microbeam subjected to fluid loading," *Microsystem Technologies*, vol. 15, no. 9, pp. 1355–1363, 2009.
- [42] Z.-Y. Zhong, W.-M. Zhang, G. Meng, and J. Wu, "Inclination effects on the frequency tuning of comb-driven resonators," *Journal of Microelectromechanical Systems*, vol. 22, no. 4, pp. 865–875, 2013.
- [43] B. S. M. Hasheminejad, B. Gheshlaghi, Y. Mirzaei, and S. Abbasion, "Free transverse vibrations of cracked nanobeams with surface effects," *Thin Solid Films*, vol. 519, no. 8, pp. 2477–2482, 2011.
- [44] M. I. Younis and A. H. Nayfeh, "A study of the nonlinear response of a resonant microbeam to an electric actuation," *Nonlinear Dynamics*, vol. 31, no. 1, pp. 91–117, 2003.